MECHANISMS FOR COLLOIDAL STABILIZATION OF MAGNETIC NANOPLATELETS

Patricija Hribar Boštjančič

Doctoral Dissertation
Jožef Stefan International Postgraduate School
Ljubljana, Slovenia

Supervisor: Asst. Prof. Alenka Mertelj, Jožef Stefan International Postgraduate School and Jožef Stefan Institute, Ljubljana, Slovenia
Co-Supervisor: Prof. Dr. Darja Lisjak, Jožef Stefan International Postgraduate School and Jožef Stefan Institute, Ljubljana, Slovenia

Evaluation Board:
Prof. Dr. Darko Makovec, Chair, Jožef Stefan International Postgraduate School and Jožef Stefan Institute, Ljubljana, Slovenia
Prof. Dr. Matija Tomšič, Member, Faculty of Chemistry and Chemical Technology, Ljubljana, Slovenia
RNDr. Vladimira Novotná, Member, Institute of Physics of Czech Academy of Sciences, Prague, Czech Republic

MEDNARODNA PODIPLOMSKA ŠOLA JOŽEFA STEFANA
JOŽEF STEFAN INTERNATIONAL POSTGRADUATE SCHOOL

Patricija Hribar Boštjančič

MECHANISMS FOR COLLOIDAL STABILIZATION OF MAGNETIC NANOPLATELETS

Doctoral Dissertation

MEHANIZMI KOLOIDNE STABILIZACIJE MAGNETNIH NANOPLOŠČIC

Doktorska disertacija

Supervisor: Asst. Prof. Alenka Mertelj

Co-Supervisor: Prof. Dr. Darja Lisjak

Ljubljana, Slovenia, April 2022

To my loved ones.

Acknowledgments

First of all, I would like to thank the Slovenian Research Agency for its financial support.

Throughout the time of my PhD study, research, and writing, countless people have offered help and support, and I would like to thank everyone who has contributed in any way to this dissertation.

A special thanks goes to my supervisor Asst. Prof. Alenka Mertelj for her expert guidance at all stages of my PhD study, for her help, suggestions, kind support and patience. I also thank her for the analyses and the calculations for the evaluation of the SAXS results and interplatelet interactions in the doctoral dissertation. Many thanks to my co-supervisor Prof. Dr. Darja Lisjak for her advice, suggestions, constructive feedback, endless support and understanding. I also thank her for the transmission electron microscopy images from the time when I have not yet learned to use the microscope. Their expert supervision has enriched this study.

I would like to thank the chair and members of the evaluation committee Prof. Dr. Darko Makovec, Prof. Dr. Matija Tomšič, and RNDr. Vladimira Novotnà for their careful review of this work and valuable suggestions for improvement.

I thank Prof. Dr. Matija Tomšič from the Faculty of Chemistry and Chemical Technology, University of Ljubljana, for SAXS measurements, Dr. Martin Cigl from the Institute of Physics, Czech Academy of Sciences, and Dr. Zois Syrgiannis from the University of Trieste for the synthesis of 10POCB and dendrimer, respectively. I thank Dr. Jelena Papan, Asst. Prof. Sašo Gyergyek, Dr. Blaž Belec, and Tanja Goršak for their help with the synthesis procedures, Mojca Vrčon Mihelj and Prof. Dr. Matjaž Valant from the University of Nova Gorica for the TG-MS measurements, Peter Medle Rupnik for his help with POM, and Žiga Gregorin for the birefringence measurements in the zero field and birefringence calculations.

I would also like to thank all my colleagues at the Department of Complex Matter, especially those in the Light and Matter group, who kindly welcomed me into their research world. A great part of my experimental work was carried out at the Department for Materials Synthesis. Therefore, I would like to thank the head of the department Prof. Dr. Darko Makovec and all the colleagues (some of whom are no longer working at the Jožef Stefan Institute) for their hospitality, help and a pleasant working atmosphere.

I would also like to thank my parents, who were always there for me and enabled me the (post)graduate study, which eventually led me to a PhD study. And last but not least, I would like to thank my partner Aleš for all the moral support, listening and encouragement.

Abstract

The dissertation presents a study of the colloidal stabilization of ferrimagnetic barium hexaferrite nanoplatelets in various isotropic and nematic media for the preparation of ferromagnetic fluids. Colloidal stability is the most important requirement to obtain a ferromagnetic liquid of barium hexaferrite nanoplatelets that exhibits spontaneous magnetization in the absence of an external magnetic field. The work is divided into three parts.

In the first part, the focus was on the study of the mechanisms for the colloidal stabilization of barium hexaferrite nanoplatelets, the surface of which was modified with a double layer of the surfactant dodecylbenzenesulfonic acid. For the nanoplatelets dispersed in alcohols, we measured the zeta potential, determined the concentration of the free surfactant in the suspensions, and calculated the Debye length. The results of the measurements formed the basis for calculating the electrostatic interaction between the nanoplatelets in four different alcohols: *tert*-butanol, 1-hexanol, 1-butanol, and 2-propanol. The comparison of the electrostatic interactions between the nanoplatelets dispersed in alcohols with different polarity allowed to determine the optimal alcohol to obtain a ferromagnetic nematic ferrofluid. 1-Butanol proved to be the best choice. The results obtained in the first part formed the basis for the continuation, i.e., the second part of the dissertation.

In the second part, we focused on the preparation of 1-butanol ferromagnetic nematic suspensions of barium hexaferrite nanoplatelets with a dodecylbenzenesulfonic acid double layer and the determination of the nanoplatelets threshold volume fraction at which the phase transition from the isotropic to the nematic phase occurs. The phase transition was determined by diluting the nematic suspension to the isotropic phase. The exact threshold volume fraction of the nanoplatelets was determined by polarization optical microscopy. Based on the birefringence of the sample, it is possible to distinguish between the isotropic (dark color) and nematic (lighter color, presence of magnetic domains) phases. We determined the threshold volume fraction for suspensions with different equivalent diameter (i.e., a disk diameter with an area equal to the basal surface of the platelet) distribution and magnetization of nanoplatelets, or concentration of dissolved dodecylbenzenesulfonic acid. In this way, we were able to determine the effect of each parameter (without changing the other two) on the threshold volume fraction. We found that the threshold volume fraction shifts to lower values when the average equivalent diameter is larger, when the magnetization of the nanoplatelets is larger, and when the concentration of dissolved dodecylbenzenesulfonic acid in the suspension is increased.

In the last part of the dissertation, we studied the colloidal stabilization of the nanoplatelets with different surface modifications in some other solvents and in the isotropic and nematic phases of a liquid crystal. The first requirement for the colloidal stabilization of nanoplatelets is a solvent that wets their surface. At the same time, sufficient repulsion between nanoplatelets is required to prevent magnetic dipole-dipole interactions from prevailing. Only smaller nanoplatelets ($<$ 35 nm) with lower magnetization remained colloidally stable in nonpolar solvents such as toluene and

chloroform, with negligible electrostatic repulsion that enabled the stability of larger nanoplatelets with higher magnetization in alcohols. Favorable interaction between the modified nanoplatelet surface and the liquid crystal is essential for colloidal stabilization in liquid crystals. In our study, oleic acid, ricinoleic acid, and a polyether chain ligand were found to be the only surface ligands for stabilization in the nematic phase of the liquid crystal. Ricinoleic acid and oleic acid enabled the preparation of a suspension in a liquid crystal with a sufficiently high concentration of the nanoplatelets to form magnetic domains.

Colloidal stabilization of the barium hexaferrite nanoplatelets was ensured in various media with sufficient electrostatic or (electro)steric repulsion. Ferromagnetic ferrofluids can be prepared in isotropic media with electrostatic repulsion (in the case of dodecylbenzenesulfonic acid and ligand with polyether chain) and in nematic medium with steric effect and suitable nematic-mediated elastic interactions (in the case of oleic and ricinoleic acids and ligand with polyether chain).

Povzetek

Osnovna tema te doktorske disertacije je študija koloidne stabilizacije ferimagnetnih nanoploščic barijevega heksaferita v različnih izotropnih in nematskem mediju z namenom priprave feromagnetnih tekočin. Ključen pogoj za pripravo feromagnetne tekočine, ki ima spontano magnetizacijo v odsotnosti magnetnega polja, je koloidna stabilizacija nanoploščic barijevega heksaferita. Delo je razdeljeno na tri dele.

V prvem delu smo se posvetili proučevanju mehanizmov stabilizacije barijevih heksaferitnih nanoploščic z dvoslojem dodecilbenzensulfonske kisline na površini. Nanoploščicam, dispergiranim v alkoholu smo izmerili zeta potencial, določili koncentracijo prostega surfaktanta v suspenzijah in izračunali Debyevo dolžino. Rezultati meritev so bili podlaga za izračun elektrostatske interakcije med magnetnimi nanoploščicami v štirih različnih alkoholih; *tert*-butanolu, 1-heksanolu, 1-butanolu ter 2-propanolu. Primerjava elektrostatskih interakcij med nanoploščicami v alkoholih z različno polarnostjo je omogočila določitev najprimernejšega alkohola za pripravo koloidno zelo stabilnih suspenzij, ki so osnova za pripravo feromagnetne nematske suspenzije. Za najboljšo izbiro se je izkazal 1-butanol.

V drugem delu disertacije smo se osredotočili na pripravo feromagnetnih nematskih suspenzij barijevih heksaferitnih nanoploščic z dvoslojem dodecilbenzensulfonske kisline v 1-butanolu in določitev koncentracije nanoploščic pri faznem prehodu iz izotropne v nematsko fazo. Volumski delež nanoploščic pri faznem prehodu smo določili z redčenjem nematske suspenzije do izotropne faze. S polarizacijsko optično mikroskopijo se na podlagi dvolomnosti vzorca lahko loči med izotropno (temna) in nematsko (svetlejša z magnetnimi domenami) fazo. Fazni prehod smo določili različnim vzorcem, ki so se razlikovali med seboj ali po distribuciji ekvivalentnega premera, magnetizaciji nanoploščic ali koncentraciji raztopljene dodecilbenzensulfonske kisline v suspenziji. S tem smo lahko določili vpliv posameznih parametrov (brez spreminjanja ostalih dveh) na volumski delež nanoploščic pri faznem prehodu. Ugotovili smo, da se fazni prehod zamakne k nižjim volumskim deležem suspenzije, če je ekvivalentni premer delcev večji, če je magnetizacija nanoploščic večja, in če povišamo koncentracijo raztopljene dodecilbenzensulfonske kisline v suspenziji.

V zadnjem delu disertacije sem z različnimi modifikacijami površine nanoploščic dosegla njihovo koloidno stabilizacijo tudi v nekaterih drugih topilih ter v izotropni in nematski fazi tekočega kristala. Za koloidno stabilizacijo nanoploščic je ključno omočenje površine delca s topilom, obenem pa je potreben tudi zadosten odboj med delci, da ne prevladajo privlačne magnetne dipol-dipol interakcije. V nepolarnih topilih kot sta toluen in kloroform so bili koloidno stabilni le manjši delci (< 35 nm) z manjšo magnetizacijo, kar je posledica zanemarljive verjetnosti elektrostatskih odbojnih interakcij, ki bi omogočile stabilizacijo tudi večjih delcev z večjo magnetizacijo. Za stabilizacijo v tekočem kristalu je pomembno, da imamo ustrezno interakcijo med modificirano površino delca in tekočim kristalom. Stabilizacijo nanoploščic v nematski fazi tekočega kristala so omogočili trije površinski ligandi: ligand s polietrsko verigo ter oleinska in ricinolejska kislina. Slednji kislini sta omogočili dovolj visoko koncentracijo nanoploščic v tekočem kristalu, da so se lahko tvorile magnetne domene.

Nanoploščice barijevega heksaferita so bile stabilne v različnih topilih z zadostnim elektrostatskim ali (elektro)steričnim odbojem. Feromagnetne tekočine je možno pripraviti v izotropnem topilu (v primeru dodecilbenzensulfonske kisline in liganda s polietrsko verigo) in v nematskem tekočem kristalu s steričnim efektom in ustreznimi elastičnimi interakcijami, ki so posledica nematičnega urejanja (primer oleinska in ricinolejska kislina ter ligand s polietrsko verigo).

Contents

List of Figures

List of Tables

Abbreviations

5CB	... 4-cyano-4'-pentylbiphenyl
10POCB	... {[4'-cyano[1,1'-biphenyl]-4-yl)oxy]decyl}phosphonic acid
AL	... alendronate sodium trihydrate
BHF	... barium hexaferrite
CCD	... charge-coupled device
DBSA	... dodecylbenzenesulfonic acid
DLS	... dynamic light scattering
DLVO	... Derjaguin, Landau, Verwey and Overbeek
DMSO	... dimethyl sulfoxide
DSC	... differential scanning calorimetry
HPA	... hexylphosphonic acid
IR	... infrared
LC(s)	... liquid crystal(s)
MO	... magneto-optic
MS	... mass spectrometry
NLC	... nematic liquid crystal
NPLs	... nanoplatelets
OA	... oleic acid
ODPA	... octadecylphoshonic acid
Pether	... (2-{2-[2-Methoxy-ethoxy]-ethoxy}-ethyl)phosphonic acid
PALS	... phase analysis light scattering
PHDA	... 16-phosphonohexadecanoic acid
PMU(s)	... promesogenic unit(s)
POM	... polarized optical microscopy
PSA	... (12-phosphono)dodecyl sulphonic acid
RA	... ricinoleic acid
RCF	... relative centrifugal force or g-force
SANS	... small-angle neutron scattering
SAXS	... small-angle X-ray scattering
TA	... thermal analysis
TEM	... transmission electron microscopy
TGA	... thermogravimetric analysis
THF	... tetrahydrofuran
VdW	... Van der Waals
VSM	... vibrating-sample magnetometer

Symbols

a	...	intercept in the linear fit equation
A	...	normalization constant
A_{Amp}	...	amplitude
b	...	slope in the linear fit equation
$\mathbf{B}$	...	magnetic field
c_{ads}	...	concentration of adsorbed surfactant to the nanoplatelets
c_{dis}	...	concentration of dissolved surfactant in the suspension
c_{i}	...	molar concentration of ions
$c_{\mathrm{i,alcohol}}$	...	concentration of ions in a given alcohol
$c_{\mathrm{i,H_2O}}$	...	concentration of ions in water
c_{max}	...	reactant concentration for infinite condensation
c_{min}	...	minimal concentration to overcome the barrier for nucleation
c_{s}	...	critical super-saturation level concentration
c_{tot}	...	total concentration of surfactant in suspension
D	...	equivalent diameter of nanoplatelets
D_{c}	...	diffusion coefficient
d_c	...	thickness of a capillary
D_{eff}	...	effective equivalent diameter
e_0	...	elementary electron charge
f	...	anisotropy function
f_1	...	decay rate
$f_{\text{1-butanol}}$	...	decay rate in 1-butanol
$f_{\textit{tert}\text{-butanol}}$	...	decay rate in *tert*-butanol
$f(q)$	...	scattering amplitude of a disk
$f(\kappa a)$	...	Debye factor
g_2	...	correlation function
g_2^{n}	...	normalized correlation function
h	...	thickness of nanoplatelets/disks
H_{c}	...	coercivity field
h_{eff}	...	effective thickness of nanoplatelets
I	...	scattering intensity
$I_1(\mathrm{x})$	...	modified Bessel function with the order 1
$J_1(\mathrm{x})$	...	Bessel function of the first kind
j/j_0	...	normalized intensity
k	...	wavenumber

K, K_1, K_2, K_3	...	elastic constants
k_B	...	Boltzmann constant
L	...	distance
M	...	magnetization
m_{DBSA}	...	mass of dodecylbenzenesulfonic acid in the sample
m_{NPLs}	...	mass of bare nanoplatelets
M_r	...	remanent magnetization
M_s	...	saturation magnetization
M_{si}	...	saturation magnetization of a particle
n	...	refractive index of a solvent
$\mathbf{n}$	...	director
$\mathbf{n}_0$	...	undeformed director field
$\mathbf{n}_1$, $\mathbf{n}_2$	...	unit vectors denoting orientation of disk 1 and 2
N	...	number of particles
$\mathbf{n}(\mathbf{r})$	...	director, where $\mathbf{r}$ denotes the position in space
$\mathbf{n}_e$	...	director easy-axis denotation
$\mathbf{n}_i$	...	unit vector
n_i	...	number density of ions
p	...	magnetic moment
$p(\mathbf{n}_1,\mathbf{n}_2,\mathbf{r})$	...	Boltzmann probability distribution
p_i	...	magnetic moment of a nanoplatelet ($i = 1$ or $i = 2$)
q	...	length of scattering vector
q_P	...	component of the length of q parallel to the disk axis
q_s	...	q multiplied with refractive index of the solvent
$q_\perp$	...	component of the length of q perpendicular to the disk axis
$\mathbf{r}$	...	distance vector, vector connecting two plates
r	...	distance between the centres of two plates (absolute value of $\mathbf{r}$)
R, R_1, R_2	...	the radius of a disk/ thin plate
r_c	...	critical size
R_{eq}	...	radius of a sphere with equivalent volume as a disk
R_s	...	radius of a spherical particle
s_1	...	stretched exponent
T	...	temperature
$<U(r)>$	...	average interaction energy
U	...	total interaction energy
$U_{anchoring}$	...	surface anchoring energy
U_{dip}	...	magnetic dipole-dipole interaction energy
U_{el}	...	electrostatic interaction energy
$U_{el,par}$	...	electrostatic interaction energy between two parallel nanoplatelets
$U_{tot,par}$	...	total interaction energy between two parallel nanoplatelets
V	...	volume of a material
V_i	...	particle/disk volume
V_s	...	volume of suspension
W	...	anchoring strength

W_{DBSA}	...	mass fraction of DBSA in the dry part of the sample
y_0	...	background
Z_{i}	...	charge of i-th species
Ze_0	...	effective surface charge
$Z_1 e_0$	...	surface charge of disk 1
$Z_2 e_0$	...	surface charge of disk 2
γ	...	mass concentration
$\Delta\, c_{\mathrm{dis}}$	...	variation in concentration of dissolved DBSA after additions
$\Delta\, c_{\mathrm{tot}}$	...	variation in the total concentration of DBSA
$\Delta\, n$	...	birefringence
$\boldsymbol{\Delta\rho}$	...	contrast between the solvent and a disk
ε	...	dielectric constant
ε_0	...	vacuum permittivity
ζ	...	zeta potential
η	...	viscosity
$\eta_{1-\mathrm{butanol}}$	...	viscosity of 1-butanol
η_{alcohol}	...	viscosity of alcohol
$\eta_{\mathrm{H_2O}}$	...	viscosity of water
$\eta_{\mathit{tert}-\mathrm{butanol}}$	...	viscosity of *tert*-butanol
θ	...	scattering angle
ϑ_{i}	...	angle between $\mathbf{r}$ and $\mathbf{n}_{\mathrm{i}}$
$\boldsymbol{\kappa}^{-1}$	...	Debye screening length
$\boldsymbol{\kappa D}$	...	Debye parameter
λ	...	wavelength of illumination
Λ	...	molar conductivity
Λ^{∞}	...	molar conductivity at infinite dilution
μ	...	electrophoretic mobility
μ_0	...	vacuum permeability
μ_{B}	...	Bohr magneton
ξ	...	surface extrapolation length
σ	...	sphere diameter
σ_{e}	...	conductivity of an electrolyte
σ_{s}	...	conductivity of a suspension or solution
$\sigma_{\mathrm{alcohol}}$	...	conductivity in an alcohol solution
$\sigma_{\mathrm{H_2O}}$	...	conductivity in water
τ	...	delay time
ϕ	...	volume fraction of nanoplatelets in a suspension
ϕ_{IN}	...	threshold volume fraction
$\phi_{\mathrm{IN,eff}}$	...	effective volume fraction
$\phi_{\mathrm{IN,eff,resc}}$	...	rescaled effective volume fraction
$\phi_{\mathrm{IN,resc}}$	...	rescaled volume fraction
ψ_{s}	...	surface potential
Ω_{i}	...	solid angle

Chapter 1

Introduction

Structural anisotropy of materials offers new perspectives on their chemical and physical properties, such as magnetic anisotropy, nonlinear optical behavior, ferroelectricity, pyroelectricity, piezoelectricity, etc. Anisotropic magnetic nanoparticles are promising for the use in various applications [1]. For example, magnetic nanoparticles dispersed in a liquid medium can be used in biomedical applications [2], in magnetooptics for magnetic control of optical properties (transmission, scattering, absorption etc.), for the development of new devices such as diffraction gratings, optical filters, and polarizers (e.g., [3]–[6]). Other applications can be found in microfluidics [7], [8] and electronics [3], medical therapy [2] and diagnostics [9].

Anisotropic magnetic nanoparticles can be either elongated, such as nanotubes and nanorods, or plate-shaped, such as nanoplates. The shape anisotropy of nanoparticles determines their magnetic easy axis, which is reflected in their response to an external magnetic field [1]. Due to shape anisotropy, it is common to have easy-plane magnetization. The hexaferrites are a particular example of materials with uniaxial magnetocrystalline anisotropy [10], [11]. Barium hexaferrite (BHF) nanoplatelets (NPLs) belong to the group of hexaferrites with a magnetic easy axis perpendicular to the plane of the plate, leading to atypical properties for plate-like magnetic nanoparticles [1], [11]. This enables unique coupling possibilities and the development of novel materials, such as ferromagnetic suspensions [1], [3]. The BHF NPLs are a type of hexagonal ferrites that can be prepared by a straightforward and environmentally friendly synthesis. Their magnetic properties are intrinsically linked to their crystalline structure, which allows their direct use in any medium [11]. There are several interactions between colloidal nanoparticles, but the most challenging attractive interaction between magnetic nanoparticles is the magnetic dipole-dipole interaction, which is the main reason for their aggregation.

In the first part of the introduction, we will discuss the crystal structure, magnetic properties and synthesis of BHF. Furthermore, we focus on explaining the interparticle interactions in liquid media and the surface modification, the understanding of which is crucial for the preparation of (nematic) ferrofluids, which will be discussed in the last part of the introduction.

1.1 Barium Hexaferrite

1.1.1 BHF crystal structure

BHF is an M-type hexagonal ferrite with space group $P6_3/mmc$ and chemical formula $BaFe_{12}O_{19}$. Its structure is composed of hexagonal and cubic layers. The O^{2-} and Ba^{2+} ions are close packed, while the Fe^{3+} ions occupy different sites. The BHF unit cell has an a

and b parameter of 0.59 nm and c parameter of 2.32 nm. The unit cell comprises of two different blocks: S and R [11]–[13] and is shown in Figure 1.1.

The S block ($Fe_6O_8^{2+}$) is a slice of spinel structure along the 111 diagonal. It is composed of two layers of O^{2-} ions. Between the O^{2-} layers, Fe^{3+} ions occupy tetrahedral and octahedral sites [12].

The R block ($BaFe_6O_{11}^{2-}$) is composed of three layers. The outer ones are O^{2-} layers, while the middle layer contains a Ba^{2+} ion. The Fe^{3+} ions cannot be allocated in the cubic sequence but are allocated differently to minimize the Coulomb energy. Consequently, the structure of the R-block becomes hexagonal. Fe^{3+} ions occupy three different types of sites. Octahedral sites are located in octahedra connected by common faces. The distances between these sites are shorter than those between the occupied octahedral sites in the S-block (shared by an edge), making the cation Coulomb energy contribution higher than for the octahedral sites of the S-block. The second site has a shape of a trigonal bipyramid. It is a fivefold coordinated site consisting of two tetrahedra with a common face. The Fe^{3+} ions in these sites can oscillate or are allocated in two sites, staggered from the central position for 0.016 nm, contributing most to the uniaxial magnetocrystalline anisotropy.

Between the R and S blocks is another octahedral site in octahedra with common edges. The energy of Fe^{3+} ions occupying these sites is different from the energy of Fe^{3+} ions in the S block. The reason for this is the difference in the surroundings. The BHF unit cell consists of four blocks, i.e. R, S, R*, S*, where * denotes the 180° rotation around the c-axis [12].

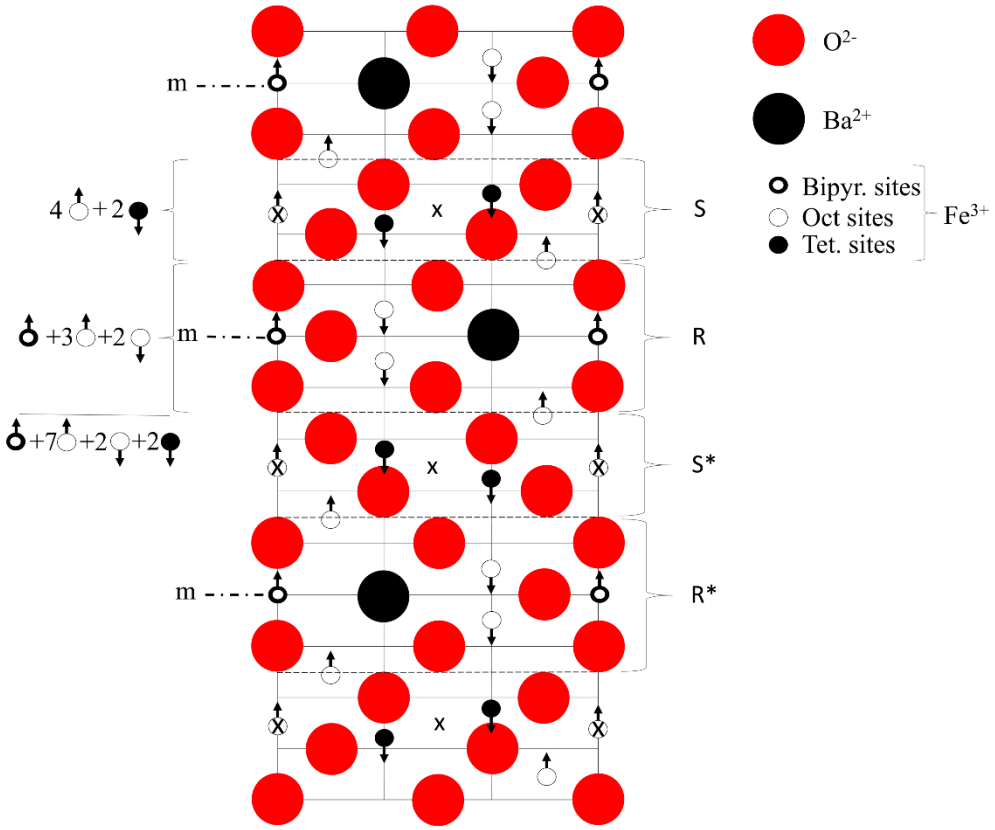

Figure 1.1: Schematic representation of the BHF unit cell, with the c-axis vertical. The letter m stands for mirror plane [14].

1.1.2 Magnetic properties of BHF

In ferromagnetic materials, a positive exchange interaction between the magnetic moments of neighboring atoms having orbitals with unpaired d-electrons induces coupling and spontaneous parallel arrangement of the magnetic moments, as shown in Figure 1.2a. The result is a net magnetic moment and spontaneous magnetization without the application of an external magnetic field [15]. When sublattices have the same opposite magnetic moments, as presented in Figure 1.2b, the material does not exhibit spontaneous magnetization and is called antiferromagnetic [15], [16].

The BHF crystal structure is not only composed of ions with unpaired d-electrons (i.e., Fe^{3+}), but also contains O^{2-} ions, which prevents direct coupling between Fe^{3+}. The ions with magnetic moments are not coupled directly but via O^{2-}, i.e., via superexchange interaction. Therefore, BHF (along with some other oxide materials) is not a ferro- but a ferrimagnetic material. The Fe^{3+} ions are in different locations in R and S blocks (see Figure 1.1) and have different directions of magnetic moment. Adjacent sublattices have an antiparallel direction of magnetic moments, as depicted in Figure 1.1 and Figure 1.2c. The different orientation of the magnetic moments in the BHF crystal (Figure 1.1) is a consequence of the exchange energy and the orientation of the magnetic moments is preferentially along the c-axis. The net magnetic moment of 40 μ_B at 0 K ($1\ \mu_B = 9.27 \cdot 10^{-21}$ erg/Oe) is a consequence of different occupation of five crystallographic sites where the magnetic moments have parallel or antiparallel orientation (see Figure 1.1) [14]. Ferrimagnetic materials exhibit spontaneous saturation magnetization M_s as well as remanent magnetization M_r and coercivity H_c, similar to ferromagnetic materials. Since the magnetic coupling in BHF is not direct, the material exhibits a lower magnetization than ferromagnetic materials. Materials do not exhibit spontaneous magnetization above the Curie temperature of the material, which in the case of BHF is 450 °C [14]. Above this temperature, the material becomes paramagnetic due to the predomination of thermal energy over magnetic coupling energy.

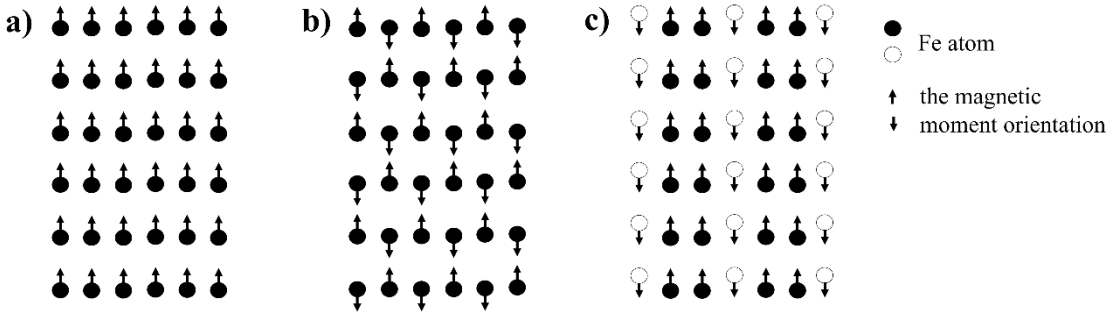

Figure 1.2: Schematic representation of the magnetic moment orientation in a) ferromagnetic, b) antiferromagnetic, and c) ferrimagnetic material [16].

Magnetism originates from the electron orbital movement and spin. Thus, each electron owns a magnetic moment. The magnetic moment of an atom is a sum of electron magnetic moments. The ratio between magnetic moment p and volume V of a material describes magnetization M [17]:

$$M = \frac{p}{V} \tag{1.1}$$

The type of atoms, their electronic structure, and their position (spacing and angle between atoms) in a crystal structure affect the magnetic properties of a material, its M_s, and magnetocrystalline anisotropy. In the case of BHF, the large Ba^{2+} ions disturb the order of the crystal lattice and are the reason for magnetocrystalline anisotropy. In anisotropic materials, the magnetic moments align in one or more preferred directions called magnetic easy axes. BHF has only one preferred direction, along the c-axis, and therefore exhibits uniaxial magnetocrystalline anisotropy. The magnetic field required to align the magnetic moments to a different crystallographic direction is called the magnetocrystalline anisotropy field [11], [14].

In a macroscopic piece of magnetic material, the spontaneous magnetization is uniform only in limited regions called magnetic domains. They are separated by magnetic walls. In the absence of the field, the direction of spontaneous magnetization in a domain depends on the crystal structure (easy axis) and the history of exposure to an external magnetic field. Magnetic domains form to minimize the magnetostatic energy, which is smallest when there is no magnetic field outside the magnetic body. This occurs when domains form such that the magnetization inside the magnetic body forms closed loops, as shown in Figure 1.3. However, the formation of domains leads to an increase in two other types of energy that contribute to the total energy of a system. The first is the so-called elastic energy, which arises when the magnetization depends on the position in space, such as in magnetic domain walls. The second is the energy contribution due to magnetocrystalline anisotropy, which increases when the orientation of the magnetization deviates from the easy axis. The details of the domain structure depend on these contributions and the history of exposure to an external field [17], [18].

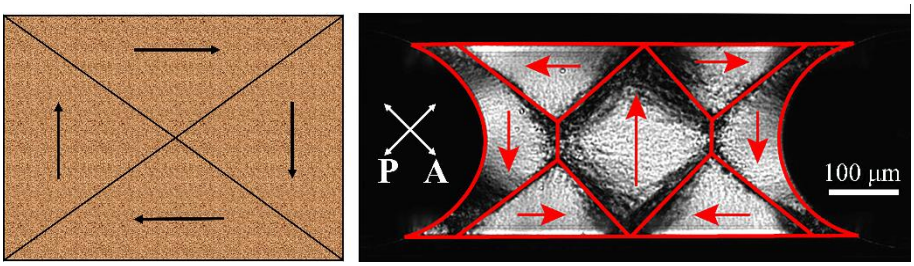

Figure 1.3: A scheme of a simple closure-domain structure in a soft magnetic material on the left and an experimental example on the right where the arrows indicate the direction of magnetization in magnetic domains [17], [19].

The magnetic properties of the sample can be determined by measuring the magnetization curve. In such a measurement, the magnetic moment of the magnetic sample is measured as a function of the external magnetic field, and the average magnetization is calculated by dividing the measured moment by the sample volume (or mass). Before exposure, the domains in a multi-domain sample are oriented in different directions and the average magnetization is zero or very close to it. When we apply an external magnetic field, the magnetization in the domains aligns in the direction of the external field and the average magnetization of the sample increases. With a sufficiently large magnetic field, all domains are aligned in the direction of the external magnetic field, and the measured magnetization value reaches its saturation M_s, as shown in Figure 1.4. By reducing the field back to zero, partial relaxation of the magnetic domains occurs and the magnetic body retains a finite average magnetic moment M_r. The field applied in the opposite direction, where the measured magnetization is reduced to zero, is called coercivity field H_c. Increasing the field in the opposite direction again leads to saturation. The shape of the magnetic

hysteresis also depends on the shape and size of the magnetic particles, since H_c and M_r are extrinsic properties. The H_c values decrease as the size of the monodomain particles decreases because the energy required to realign the magnetic moments in the direction of the external magnetic field is smaller. H_c is the highest for the largest monodomain particles, while multidomain structure decreases H_c [16], [20]. Due to the high magnetocrystalline anisotropy, BHF is a hard magnetic material, which is reflected in the magnetization curve with wide magnetic hysteresis. Ferri- and ferromagnetic materials are classified as hard- and soft magnetic, depending on the shape of the hysteresis loop, as shown in Figure 1.4.

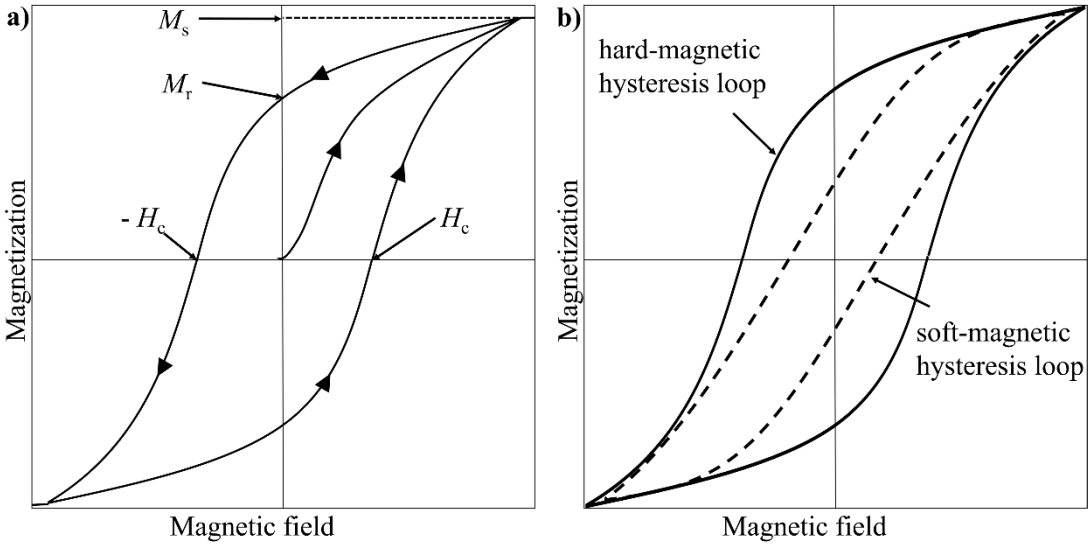

Figure 1.4: a) Magnetic hysteresis, where M_s is the saturation magnetization, M_r is the remanent magnetization, and H_c is the coercivity field. b) An example of hysteresis for soft and hard magnetic material [15], [21].

The magnetic properties of BHF originate from Fe^{3+} ions in the crystal lattice. The higher the number of Fe^{3+} ions, the higher the net magnetic moment of a crystal. When we reduce the size of BHF nanoparticles to below 10 nm, we observe a quantum size effect, where the particle size affects the electronic structure and consequently the properties of the nanoparticles, such as optical and magnetic properties. Superparamagnetism is a property of sufficiently small nanoparticles that at larger sizes exhibit ferro- or ferrimagnetic behavior. The nanoparticles become superparamagnetic at a critical volume that is inversely proportional to the magnetic anisotropy of the material [10], which in the case of BHF is as small as 300 nm^3 [22]. The magnetic anisotropy energy of superparamagnetic nanoparticles is comparable to the thermal energy. The time of realignment of magnetic moments is much shorter than the measurement time, and the average value of magnetization appears to be zero. This type of behavior is called Néel relaxation, and the time between two random flips of magnetization is called Néel relaxation time [23]. Superparamagnetic nanoparticles can be magnetized in an external magnetic field, but they do not show any M_r and H_c is zero. Decreasing the temperature of superparamagnetic nanoparticles below the so-called blocking temperature, the thermal energy decreases and consequently the Néel relaxation time increases, so they become ferromagnetic, i.e., show M_r and H_c [20]. Magnetic nanoparticles dispersed in an isotropic solvent undergo Brownian rotation and motion [24]. Although nanoparticles are sufficiently large to be ferromagnetic, they are randomly oriented in a solvent and the suspension

behaves like a superparamagnetic material, i.e., it has no spontaneous magnetization in the absence of a magnetic field. Nanoparticles that undergo Néel or Brown relaxation do not exhibit H_c. The H_c of a nanoparticle increases with increasing size as long as the nanoparticles are monodomain. When they exceed the maximum size of a monodomain, multiple domains begin to form and the H_c value decreases. To obtain monodomain nanoparticles with the highest possible magnetic moment, the domain wall energy must slightly exceed the magnetostatic energy. The domain wall energy depends on magnetic anisotropy and exchange energy, while the magnetostatic energy depends mainly on M_s and nanoparticle shape. The critical size for the formation of multidomain ferromagnetic particles is larger for materials with higher magnetocrystalline anisotropy [17], [20]. Monodomain BHF NPLs with a diameter of > 10 nm are ferrimagnetic and exhibit a typical hard magnetic hysteresis loop [22], [25].

Sufficiently large nanoparticles not to exhibit the quantum size effect (> 1000 atoms for isotropic shape) are nevertheless different from submicron particles. The reason is the surface area to volume ratio. For example, the surface to volume ratio of a cube with a side length of 1 µm is 100 times smaller than the surface to volume ratio of cubes with a side length of 10 nm and the same volume. The number of surface atoms highly exceeds the number of atoms inside the nanoparticle. The contribution of the surface atoms, which do not have the same coordination as the inner atoms, to the properties of nanoparticles is different due to the difference in coordination and other surface effects, which leads to a change in the magnetic properties of the nanoparticles and decreases M_s.

1.1.3 Synthesis of BHF NPLs

The hydrothermal method allows the synthesis of monodomain BHF NPLs at temperatures below 280 °C. It is a commonly used wet chemical method for the synthesis of nanomaterials, where the reaction takes place in water at temperatures above 100 °C and correspondingly elevated pressure [26]. The role of water is not limited to being a medium and a solvent, but it can also catalyze the reaction or be a reactant in a hydrolysis reaction [27], [28]. At the same time, the properties of water such as viscosity, density, and dielectric constant under hydrothermal conditions differ from those under ambient conditions [26], which changes the solubility and mass transfer in the reaction mixture. The dielectric constant, viscosity, density, and surface tension of water decrease with increasing temperature, while the ionic product increases. The change in the strength of acids and bases affects the reaction conditions, which are different from those at ambient conditions [29].

The hydrothermal synthesis of BHF NPLs begins with the coprecipitation of metal ions from an aqueous solution. During precipitation, a chemical reaction converts soluble compounds into insoluble ones. When two or more different cations are precipitated simultaneously, we refer to coprecipitation. Coprecipitation is a process that can be used for the synthesis of nanoparticles without subsequent hydrothermal treatment [29], e.g., for the synthesis of superparamagnetic iron oxide nanoparticles [30]. For the synthesis of BHF NPLs, the corresponding hydroxides are coprecipitated and the reaction mixture is subsequently hydrothermally treated [25]. The coprecipitation of metal ions from the aqueous solution is triggered by the addition of hydroxyl ions, leading to the formation of a zero-charge precursor. During the nucleation process, the zero-charged precursor condenses. When the concentration reaches a critical level of supersaturation (c_s), homogeneous nucleation is possible, as depicted in Figure 1.5. When c_{min} is reached, the rate of condensation increases rapidly and is infinite when the concentration is at least c_{max}. Nuclei are formed immediately. The rate of nucleation depends on the rate of the precursor formation. When the latter process is slower, both the concentration of precursors and the

rate of condensation decrease. When the concentration of reactants falls below c_{min}, nucleation comes to an end [31], [32] (see Figure 1.5). Nucleation is followed by the growth process. In this phase, nuclei grow until they reach a critical size of the primary particle. Nucleation and growth can occur simultaneously if the concentration of the precursor is higher than c_{min}. To produce particles with a narrow size distribution, the nucleation and growth phases must be separated, which is also known as the LaMer-Dinger principle [33]. Such separation is achieved when the precursor concentration drops below c_{min} instantly after the nucleation phase and does not increase above c_{min} during the growth phase. In the opposite case, the particles grow while nucleation is still taking place.

The last phase is the ageing phase, which lasts from a few hours to a few months and in which we obtain a thermodynamically stable phase. In this phase, the particles recrystallize into the most thermodynamically stable crystal structure or change their morphology. Particles smaller than a critical size dissolve and larger particles grow at the expense of the dissolved particles. This process is called Ostwald ripening.

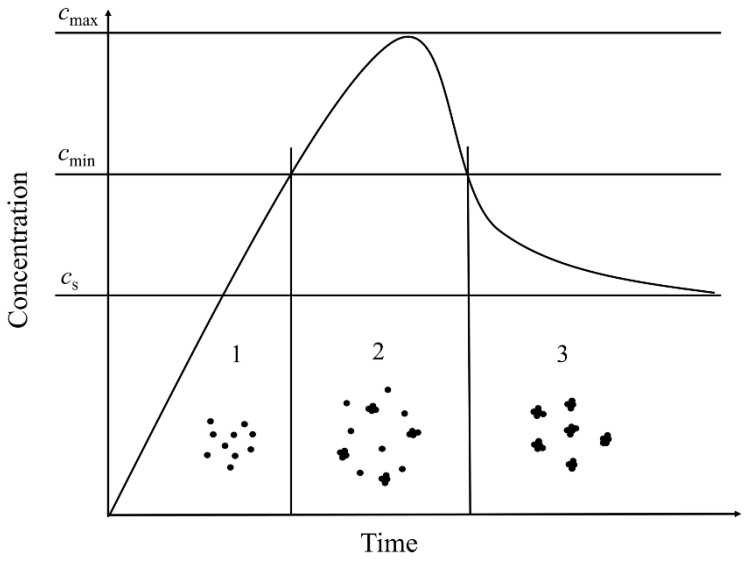

Figure 1.5: Schematic representation of the precursor concentration with time during the processes: formation of precursor (1), nucleation (2), and growth (3) [31].

Hydrothermal synthesis enables the synthesis of BHF particles at temperatures below 280 °C, which is much lower than the temperatures required for the preparation of BHF particles with, for example, combustion (700–850 °C) [34], [35], sol-gel synthesis (900 °C) [36], crystallization in glass (> 600 °C) [37], [38] or solid-state synthesis (≥ 1000 °C) [11]. The main problem besides the synthesis temperature is that in (partial) solid-state synthesis, the BHF NPLs are most likely to aggregate and prevent colloidal stability. Recently, however, Borin et al. used crystallization in glass to prepare ferrofluids from BHF NPLs with size and M_s comparable to hydrothermally synthesized NPLs [39].

In 2007, Drofenik et al. [25] presented the use of controlled hydrothermal synthesis at temperatures below 280 °C and correspondingly elevated pressure. Nucleation and crystallization at these temperatures were enabled by an excess of Ba^{2+} and OH^- ions. Pure BHF NPLs were obtained at an optimal precursor composition $Ba(OH)_2 \cdot 8H_2O/\gamma\text{-}Fe_2O_3 = 0.3$ and the by-product $BaCO_3$ was easily dissolved with hydrochloric acid. OH^- ions play an essential role in the synthesis [25], [40], as they affect the concentration of precursors. $Fe(OH)_3$ reacts with the OH^- ions to form a tetrahydroxoferate (III) $Fe(OH)_4^-$. In a very

alkaline environment, the $Fe(OH)_4^-$ forms aggregates $[Fe(OH)_4]_x^{x-}$ [22], where x varies with the concentration of the OH^- ions [40]:

$$y\left[Fe(OH)_4\right]_x^{x-}(aq) + Ba^{2+}(aq) \Leftrightarrow BaFe_{12}O_{19}(s) + 19H_2O(l) + 10OH^-(aq) \tag{1.2}$$

where y is the number of $[Fe(OH)_4]_x^{x-}$ and x is the number of $Fe(OH)_4$-units per complex, the product of x and y should be 12. Increased concentration of OH^- ions triggers precipitation and subsequent nucleation of BHF. A high concentration of OH^- ions increases the concentration of $[Fe(OH)_4]_x^{x-}$ complexes (see Eq. (1.2)), which is required for the supersaturation of the reaction mixture. Consequently, the supersaturation in the reaction mixture occurs at a relatively low temperature (even below 100 °C) and high synthesis temperatures are no longer required [40]. However, the continuous release of OH^- ions resulted in simultaneous nucleation and growth, which led to a wide distribution of the equivalent diameter (i.e., a disk diameter with an area equal to the basal surface of the platelet) of NPLs [40]. The size of BHF NPLs strongly depends on the synthesis temperature. Very small NPLs with a diameter of 10 nm are prepared at temperatures of 150 °C and below [41]. Such NPLs are superparamagnetic and exhibit a low M_s of ~ 10 A m^2/kg at an applied magnetic field of 5 T. The crystal structure of the NPLs comprises an SRS* segment with a theoretical composition of $BaFe_{18}O_{28}$, which is only a part of the unit cell with composition SRS*R* [42]. Increasing the synthesis temperature above 150 °C leads to larger NPLs due to the Ostwald ripening process. During the process of exaggerated growth, which occurs at temperatures above 160 °C and at longer synthesis times, some individual NPLs grow very rapidly. The diameter of the BHF NPLs increases much faster than the thickness that increases discretely with the additions of the R and S segments [42], leading to an increase in M_s and H_c. Exaggerated growth can be controlled by the addition of surfactants such as oleic acid, which allows the preparation of uniform and ultrafine superparamagnetic NPLs at 240 °C [22].

Another way to suppress secondary growth is the substitution of Fe^{3+} ions. Partial substitution of Fe^{3+} ions by more voluminous Sc^{3+} and In^{3+} ions reduces the mass transport during particle growth and reduces the deposition rate, resulting in a very efficient solution. The result is enhanced primary particle growth and suppression of exaggerated growth of NPLs [43]. In this way, the NPLs exhibit a narrower distribution of equivalent diameter than unsubstituted BHF NPLs. Moreover, the magnetic properties of the partially substituted $BaFe_{12-x}M_xO_{19}$ (M stands for a more voluminous metal ion) NPLs are slightly improved compared to the unsubstituted BHF NPLs [43]. The Sc-substituted NPLs (nominal composition $BaFe_{11.5}Sc_{0.5}O_{19}$) hydrothermally synthesized at 240 °C had an average diameter of (43 ± 17) nm and exhibited comparable M_s to the unsubstituted NPLs with an average diameter of (110 ± 90) nm [43]. The maximum diameter decreased from 623 nm to 105 nm by increasing the Sc^{3+} content from x = 0 to 0.5 (nominal). A detailed analysis of the crystal structure of the Sc^{3+}-substituted BHF NPLs [44] showed that the distribution of Sc^{3+} is very inhomogeneous and preferentially concentrated in the R blocks. Unlike in bulk [45], Sc^{3+} in NPLs also partially substitutes Ba^{2+} and not only Fe^{3+}. The charge difference is compensated by the formation of some ionized cation vacancies [44].

1.2 Interparticle Interactions and Colloidal Stability

The colloidal stabilization of nanoparticles in a solvent depends on the interactions between the nanoparticles, which can be either attractive or repulsive. The nature of the interaction depends on the type of the nanoparticles dispersed and the type of solvent. In the next

sections we present the forces between particles and the relations necessary to obtain stable colloidal suspensions.

1.2.1 Van der Waals interactions

Van der Waals (VdW) interactions occur between atoms, molecules, or particles. The origin of VdW forces is the dipole or induced dipole interactions at the atomic level. The VdW potential energy between colloidal particles is distance dependent and also depends on the dielectric properties of the suspension, i.e., the particles and a solvent. The VdW interaction can be either attractive or repulsive between particles in a solvent. The VdW force is repulsive when the value of the dielectric constant of the solvent is between those of the two different particles [46]. To achieve colloidal stability of the suspension, the attractive VdW forces must be overcome by additional repulsive interactions, such as electrostatic, steric or electrosteric.

1.2.2 Electrostatic interaction

Systems in which only VdW forces are present are limited to a few, for example, interactions between nonpolar molecules in vacuum. In colloidal suspensions in polar solvents such as water and alcohols, electrostatic interactions between particles occur in addition to the VdW interactions. The interplay between the two types of interactions is very important. If only attractive VdW interactions between similar particles were to act, the particles would eventually aggregate and separate from the solvent. Between the surface-charged particles dispersed in polar solvents long-range electrostatic interactions occur. The surface of the particles is covered with ionized functional groups. In the case of oxide particles, the surface groups are hydronium and hydroxide ions, which provide positive or negative surface charge, depending on the pH of the suspension. The particle surface modified with surfactants may also have a surface charge that may differ from the surface charge of the bare particles, depending on the type of surfactant. The ionized groups on the particle surface are in a polar solvent surrounded by a layer of strongly bound ions called the slipping plane, which is surrounded by a diffuse layer of ions forming an electric double layer, as depicted in Figure 1.6. The surface potential decreases with distance from the particle and eventually approaches zero when the concentration of counter ions and coions is equal. The charges in the slipping plane are strongly bound and move with the particle, while the charges outside the slipping plane remain with the bulk fluid [47]. The slipping plane has a determinable potential called the zeta potential (see Figure 1.6). Changing the pH of the suspension has a strong effect on the net surface charge and the zeta potential. The pH at which the net charge is zero is called the isoelectric point. At this pH, the electrostatically stabilized suspensions lose their colloidal stability [46]. The zeta potential ζ is calculated from the electrophoretic mobility, which is measured under an applied electric field [48]:

$$\zeta = \frac{3\mu\eta}{2\varepsilon\varepsilon_0 f(\kappa a)} \tag{1.3}$$

where μ is the electrophoretic mobility of the particles, η the viscosity of the solvent, ε the dielectric constant of the solvent, ε_0 the vacuum permittivity with a value of $8.854 \cdot 10^{-12}$ (A s)/(V m), and $f(\kappa a)$ is the Debye factor. The Debye factor is 1.5 when the particle radius is much larger than the electric double layer. In the opposite case, it is 1. Eq. (1.3) is known as Henry's equation [48]. The surface charge of the particles arises either from the dissociation of the surface groups or from the adsorption of ions on a neutral surface.

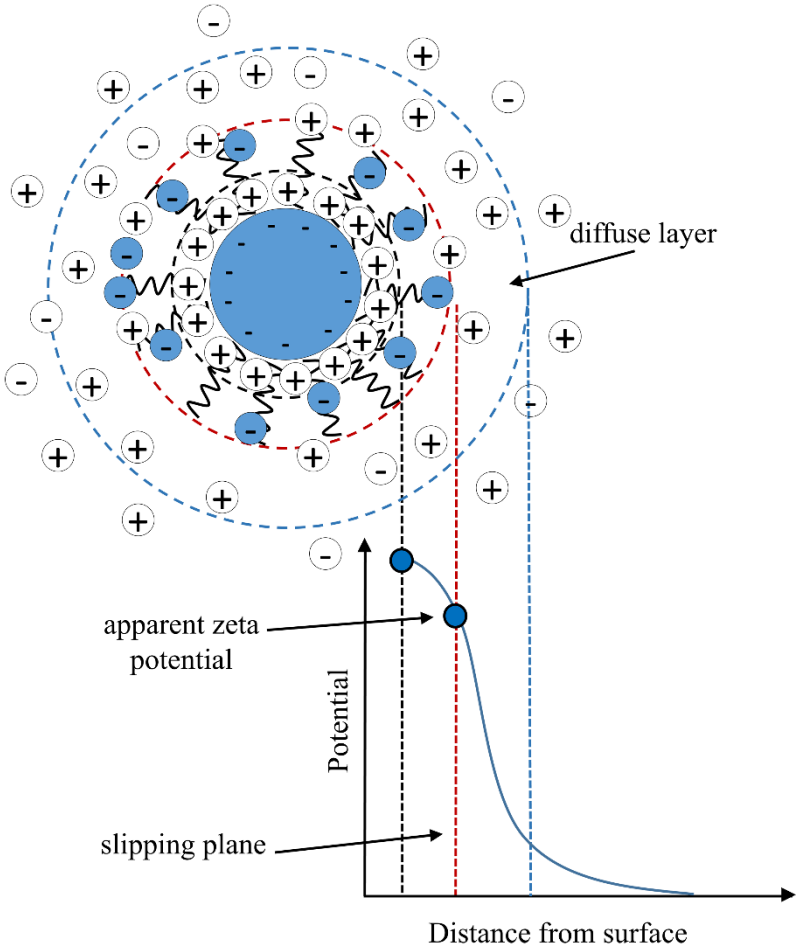

Figure 1.6: Schematic representation of a charged particle (with a thin negatively charged polyelectrolyte layer). The apparent zeta potential is at the slipping plane, i.e., at the imaginary boundary between the ions moving with the particle and the ions remaining in the bulk fluid [47].

The thickness of a charged layer near a charged surface, called a diffuse electric double layer, is also known as the Debye screening length κ^{-1}. This is the distance at which the electrostatic repulsion between colloidal particles is significant. The Debye length in a suspension depends on the dielectric properties of the solvent and the ionic strength of the suspension. In a suspension with lower ionic strength, the surface charge is weakly shielded, resulting in a thicker ionic double layer and a higher zeta potential. Therefore, there is a stronger interparticle repulsion. The Debye screening length can be calculated using the following expression [46]:

$$\kappa^{-1} = \sqrt{\frac{\varepsilon\varepsilon_0 k_B T}{e_0^2 \sum_i n_i Z_i^2}} \tag{1.4}$$

where k_B is the Boltzmann constant with a value of $1.38 \cdot 10^{-23}$ J/K, T is the absolute temperature, e_0 is the elementary electron charge with a value of $1.6022 \cdot 10^{-19}$ A s, n_i is the number density of the i-th ionic species in the suspension, and Z_i is the charge of the i-th ionic species in the suspension.

In aqueous medium, the surface charge depends on the type of the dissociating functional groups and the pH of the suspension, since the dissociation of the functional groups is pH dependent. For example, the surface charge of particles, which is provided by an acidic group (e.g., carboxyl group) is expected to be negative over most of the pH range, while the charge provided by basic groups (e.g., amino group) is expected to be positive. In nonpolar solvents with a very low dielectric constant, dissociation is very unlikely to occur, but surfactant molecules can maintain the surface charge within micelles dispersed in a nonpolar solvent above a critical micelle concentration. Micellization can be accelerated by adding water and ions to the nonpolar solvent, which adds a charge. In addition, some studies have shown that particles dispersed in nonpolar solvents can also carry a surface charge [49]–[53]. Dispersants and surfactants must be able to interact with the solvent and particles to be adsorbed on the particle surface and have high solubility in the solvent. Such dispersants are usually surfactants with long nonpolar moieties and a functional group (acidic or basic) capable of interacting with the particles via hydrogen bonds or acid-base interactions. Studies of charge mechanisms in nonpolar solvents [51]–[53] revealed that the most probable charge-generating process is proton transfer between the particle surface and dispersant. The electrosteric contributions to the stability of carbon black in dodecane at different concentrations of a basic dispersant polyisobutene succinimide were discussed by Pugh et al. [51]. Carbon black has surface groups such as phenols and carboxyl groups and the dispersant adsorbs in a thick layer to the surface of the carbon black from nonpolar solvent. The measured zeta potential had a negative value in the low dielectric constant medium. The proposed explanation for the charge formation and its sign was proton transfer. Protons are transferred from the acidic sites on the particle surface to the basic sites of the dispersant that becomes protonated. The next step is the (partial) desorption of the protonated dispersant into the medium and consequently the particle surface remains negatively charged, as depicted in Figure 1.7 [51]. The process is expected to reverse when the particles act as a base and the dispersant is acidic.

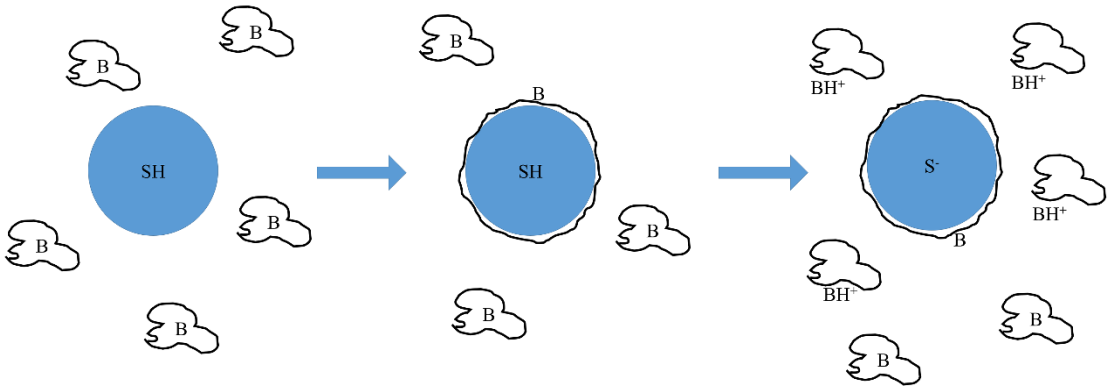

Figure 1.7: The proposed mechanism for the negative charge of carbon black dispersed in dodecane in the presence of a basic dispersant (left), with the dispersant (B) adsorbed to the acidic particle surface (SH) in the middle. Proton transfer between the acidic surface and the basic dispersant results in a negatively charged surface and a positively charged desorbed dispersant in the surrounding medium (right) [51].

1.2.3 DLVO theory

The DLVO theory, named after the initials of the four scientists who proposed it, namely Derjaguin, Landau, Verwey and Overbeek, describes the behavior of suspensions (of spherical particles) based on the relationship between the VdW and electrostatic interactions. The electrostatic and, accordingly, the total interaction energy between particles depends on the surface charge density and the Debye length. Figure 1.8 depicts the total interaction energy at different distances between two particles and at different surface charge densities. Curve a in Figure 1.8 represents particles with a high surface charge density in a dilute electrolyte where the Debye length is large and there is a strong long-range repulsion. In this case, a high energy barrier occurs due to the predominant repulsive electrostatic interaction. Reduced surface charge density (curve b), i.e., with the addition of electrolyte that increases the ionic strength and thins the double layer, causes a decrease in the height of the energy barrier (curve b) and the presence of a secondary minimum in which the particles reversibly flocculate. The particles in such a system can either remain in the secondary minimum or be thoroughly dispersed in the solvent. Reducing the surface charge density lowers the energy barrier (curve c) to the point where attractive VdW interactions prevail and the particles aggregate. When a critical aggregation concentration is reached, the energy barrier drops below zero (curve d). The particles aggregate and the suspension is unstable. Curve e represents a system in which only VdW interactions are present and the particles aggregate. Such particles have no surface potential (pH of the isoelectric point) [46].

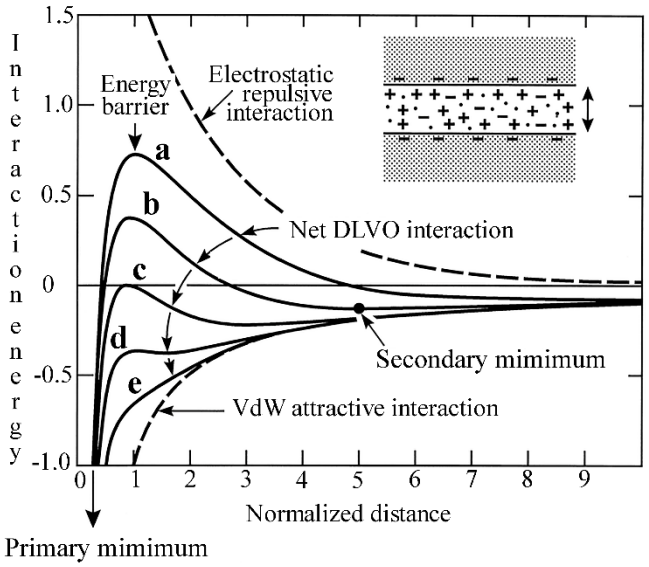

Figure 1.8: The interaction energy as a function of the distance between two particles [46], where a–e represent systems with different surface charge densities (a with the highest and e with the lowest surface charge density).

The VdW interactions depend on the size and shape of the particles. Stronger VdW forces act between larger particles than between two smaller particles. The range of attractive VdW forces is a few nm. The interaction energy changes differently with interparticle distance for spherical and plate-shaped particles. A comparison of the interaction energy between two spherical and two plate-shaped particles with the same surface charge for different situations is given in Figure 1.9 as a function of distance. While

repulsive forces can act between two curved surfaces at all distances, the forces between two flat surfaces can be attractive at the same distance with a stable equilibrium (see Figure 1.9b). At the same time, attractive forces can act between two curved surfaces at all distances, while between two flat surfaces the forces can be repulsive at a certain distance (see Figure 1.9c) [46].

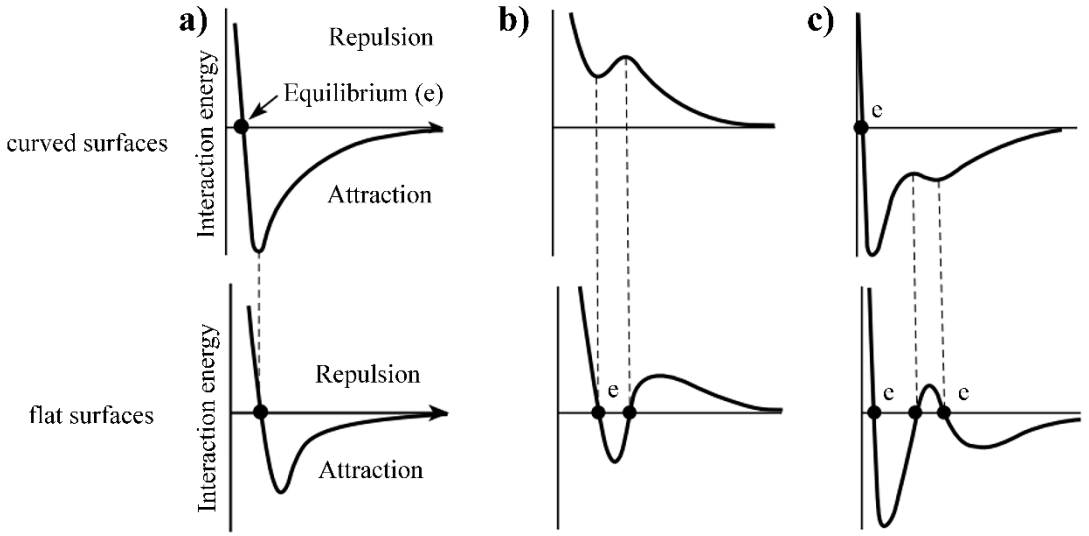

Figure 1.9: The diagrams show a comparison of the interaction energy as a function of the distance between two curved surfaces (top three) and between two flat surfaces (bottom three) with the same surface charge – the points marked with e represent the equilibrium, where the force is zero. a), b) and c) represent systems with a different surface charge. b) The force can be repulsive between two curved surfaces and attractive between two flat surfaces with the same surface charge, with a stable equilibrium at a finite distance. c) Also, attractive forces between two curved surfaces can become repulsive between two flat surfaces with the same surface charge [46].

1.2.4 Steric interaction

For colloidal suspensions in nonpolar solvents, electrostatic repulsion is very unlikely to occur. Nevertheless, steric stabilization can be exploited in both nonpolar and polar solvents. Dense steric barriers can efficiently overcome the attractive forces between nanoparticles and prevent their aggregation. Steric stabilization is provided by specific surface modifications with large organic molecules (e.g., polymers) that interact with the solvent. For example, to colloidally stabilize polymer-coated nanoparticles, the solvent must wet (solvate) the surface and allow the polymer chains to uncoil, forming a steric barrier, as shown in Figure 1.10a. The polymer chains act like a spring that in the case of efficient solvation uncoils and repels other particles enabling colloidal stability. In the opposite case, the chains coil, and the particles aggregate, i.e., depletion flocculation occurs, as shown in Figure 1.10b. Unlike electrostatic, steric stabilization is not affected by the ionic strength of the suspension [46], [54].

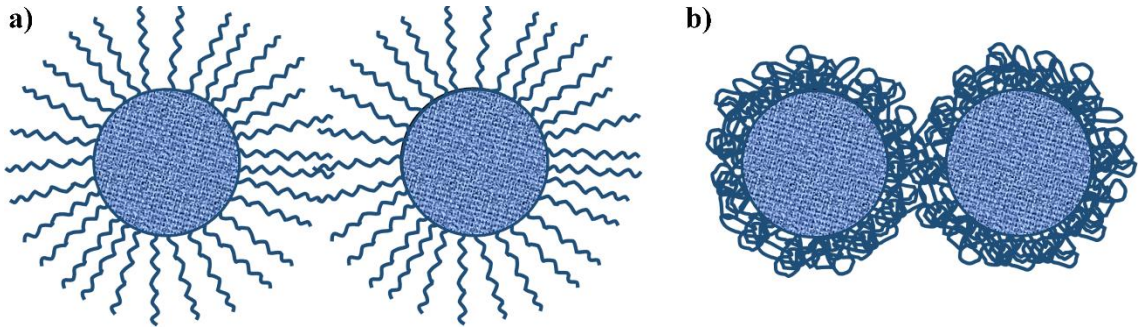

Figure 1.10: Schematic representation of a) steric stabilization, b) depletion flocculation.

1.2.5 Electrosteric interaction

The electrosteric interaction between colloidal nanoparticles is a combination of electrostatic and steric interaction. It is usually achieved by surface modification with polyelectrolytes or amphiphilic polymer brushes. The latter contain both, cationic and anionic groups. Polyelectrolytes with an affinity for the surface of nanoparticles (oppositely charged) adsorb on the surface. The behavior of the adsorbed polyelectrolyte in a solvent depends on the nature of the system. Any change in pH, ionic strength, and dielectric properties in the suspension can affect the electrostatic and steric stabilization. Higher ionic strength in the suspension screens the charges of polyelectrolyte, reducing the electrostatic repulsion, which leads to chain collapse and consequently reduces the steric barrier [54].

1.2.6 Solvation interaction

The solvation interaction occurs in the colloidal suspensions at short distances below 2 nm and depends on the local order of the solvent molecules between the surfaces of the nanoparticles. Figure 1.11 shows the distribution of solvent molecules between two surfaces at different distances. The solvation interaction depends on the distance between the two surfaces and oscillates with the oscillation period determined by the size of the solvent molecules. Repulsive interactions occur at distances corresponding to multiples of an approximate sphere (i.e., of a molecule) diameter σ (see Figure 1.11a (b, d, f)) and attractive interactions are observed in-between (see Figure 1.11a (a, c, e, g)) [46]. Solvation in water is called hydration and solvation forces in water are called hydration forces. The latter arise when water molecules bind to the hydrophilic groups on the surface of particles.

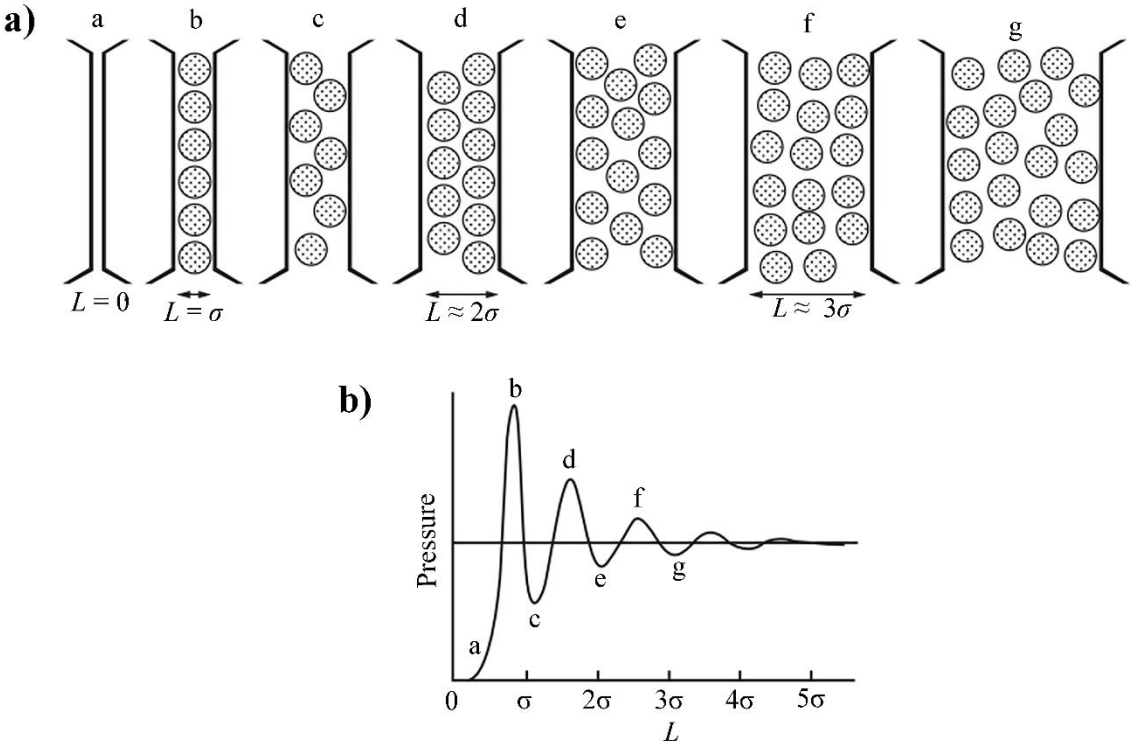

Figure 1.11: a) Distribution of solvent molecules between two surfaces at different distances (a–g), b) distance-dependent oscillation solvation force, where σ is the sphere (i.e. molecule) diameter and L is the distance between two surfaces [46].

1.2.7 Magnetic interaction

In suspensions of magnetic NPLs, there are long-range interactions between magnetic dipoles in addition to VdW interactions. Magnetic dipole-dipole interactions U_{dip} represent the most challenging attraction between magnetic nanoparticles and are the main reason for their aggregation in a liquid. The magnitude of the interaction between two magnetic dipoles depends on the relative orientations of the NPLs, which is described by the expression in parentheses in [15]:

$$U_{\text{dip}} = -\frac{\mu_0 p_1 p_2}{4\pi r^3}\left(\frac{3(\mathbf{n}_1 \times \mathbf{r})(\mathbf{n}_2 \times \mathbf{r})}{\mathbf{r} \times \mathbf{r}} - \mathbf{n}_1 \times \mathbf{n}_2\right) \tag{1.5}$$

where μ_0 is the vacuum permeability with a value of $1.257 \cdot 10^{-6}$ H/m, p_1 and p_2 are the magnetic moments of two NPLs, and r is the distance between the centers of the two NPLs. $\mathbf{r}$ is a vector with an absolute value r, and $\mathbf{n}_1$ and $\mathbf{n}_2$ are unit vectors denoting the orientation of the NPL's magnetic moment. An individual magnetic nanoparticle has a magnetic moment p_i that is a function of the saturated magnetization M_{Si} and the particle volume V_i [17]:

$$p_i = M_{Si} V_i \tag{1.6}$$

Larger particles have larger magnetic moment and consequently larger magnetic dipole-dipole interaction energy [24]. The possibility for aggregation is greater in this case. Figure 1.12 depicts two thin magnetic disks with magnetic moment p_i perpendicular to the disk plane. The energy of the magnetic dipolar interaction depends on the orientation of the disks, on average it is attractive. In the case where $\mathbf{n}_2$ is parallel to $\mathbf{n}_1$ and on the symmetry axis of $\mathbf{n}_1$, the magnetic attraction between the disks is the strongest and Eq. (1.5) is simplified to [15]:

$$U_{\text{dip}} = -\frac{\mu_0 p_1 p_2}{4\pi r^3} \tag{1.7}$$

Colloidal stabilization of hard magnetic NPLs is challenging, especially due to the strong magnetic dipole-dipole interactions, and requires strong repulsive interactions between the NPLs. Such repulsion can be achieved by electrostatic interactions.

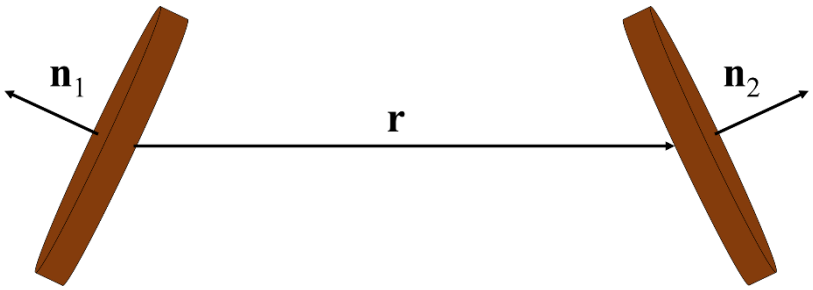

Figure 1.12: Two thin disks as magnetic NPLs connected by a vector $\mathbf{r}$ with absolute value r, where $\mathbf{n}_1$ and $\mathbf{n}_2$ denote the orientation of the NPL magnetic moment [55].

1.3 Ferrofluids

Ferrofluids are colloidal suspensions of magnetic nanoparticles dispersed in a carrier fluid [24], [56]. The thermal energy that causes Brownian motion, in combination with the coating around the nanoparticles, keeps the ferrofluids colloidally stable [24]. Magnetic nanoparticles can be sterically stabilized if their magnetic moments are relatively small. When such nanoparticles are in contact in the absence of a magnetic field, the thermal energy is larger than the average magnetic interaction energy. However, when a magnetic field is applied, the magnetic interaction energy dominates the thermal energy and causes the formation of chain-like structures characteristic for ferrofluids. Chain formation is possible even without an external magnetic field if the nanoparticles have sufficiently large magnetic moments [24], [57]. To prevent such behavior and ensure colloidal stability, the electrostatic repulsion between the particles must outweigh magnetic attraction. BHF NPLs are magnetically hard nanoparticles that tend to form chains and aggregate more than smaller superparamagnetic nanoparticles due to strong magnetic dipole interactions. Therefore, special attention must be paid to the surface modification of BHF NPLs to ensure the colloidal stability of their suspensions.

1.3.1 Surface modification of nanoparticles

Two approaches can be used for the surface modification of nanoparticles, namely in-situ and post-synthetic modification [58]. Surface ligands used in in-situ surface modification not only provide colloidal stabilization but can also change the size and shape of

nanoparticles [22], [27]. Post-synthetic surface modification can be applied directly to the synthesized bare nanoparticles or by a ligand exchange, where one weaker-bound ligand is replaced by another [58]. A variety of molecules that can serve as surface-modifying ligands offer different options to choose from. The choice depends on the interaction between the nanoparticle's surface and the anchoring group, and on desirable interactions between a nanoparticle and a solvent. The interactions can be modified with the length, composition, and functional groups in the ligand chain.

Surface modification of nanoparticles is critical for colloidal stability. The anchoring groups that bind to the nanoparticle surface must be selected with respect to the composition of the nanoparticle surface. In terms of composition and reactivity, the surface of BHF NPL is very similar to the surface of iron oxide nanoparticles. Several functional groups show affinity to the iron oxide surface via electrostatic, coordination or covalent interactions [58]. Electrostatic interactions are weaker than covalent or coordination bonds and are less preferred for surface modification. However, they can still contribute to colloidal stabilization. Electrostatically bound anchoring groups can be relatively easily replaced with anchoring groups with stronger affinity to the iron oxide surface and can be used for intermediate modification prior to colloidal stabilization with other, more strongly bound ligands [58]–[60]. In the following sections, we describe the interactions between the surface of iron-oxide nanoparticle and sulfonic acid, carboxylic acid and phosphonic acid anchoring groups.

The interaction between a sulfonic acid and the iron oxide surface is an acid-base reaction between the S-OH and OH groups on the surface [61]. The electrostatically driven interaction between a deprotonated sulfonic anchoring group and a positively charged iron-oxide surface leads to surface modification [62], [63]. Due to the size of the sulfonic group, not all binding sites on the surface are occupied and some free Fe-OH surface groups can lead to a ligand desorption process in which the proton of the OH surface group is transferred to the sulfonate group of the ligand [61]. Such behavior reduces the number of ligand molecules on the surface, which may lead to lower colloidal stability. On the other hand, in the case of attractive interactions between the ligand tails, a double layer can form around the particle, increasing the colloidal stability [62].

Carboxylic acids, such as oleic acid [64], [65], ricinoleic acid [65], and citric acid [66], are well known surface-modifying ligands that provide colloidal stability for iron oxide nanoparticles. The carboxylic acid can bind to a metal oxide surface in two different ways, as depicted in Figure 1.13, namely monodentate and bidentate (bridging or chelating) [58]. In most cases, the formation of a strong bond between the carboxylic acid group and a metal oxide surface requires a high pH (to ensure deprotonation of the OH groups) and a high temperature [30], [63], [66]–[68].

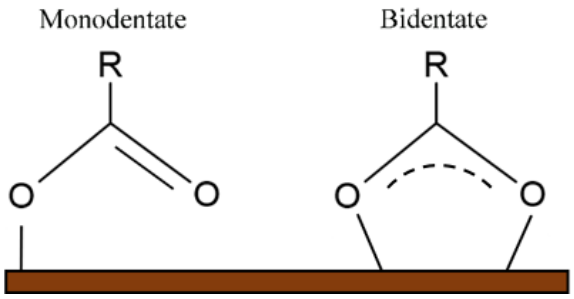

Figure 1.13: Two possible modes of the carboxyl group binding to iron oxide surface [58].

Phosphonic acids are phosphorus compounds with the highest affinity for iron oxide surfaces and a very good choice for surface modification of nanoparticles [61], [69]–[72]. The binding mechanism of phosphonic acids is explained as an acid-base condensation reaction of P-OH groups with the OH groups on the metal oxide surface and the byproduct H_2O [73]. Phosphonic acids have three active binding groups leading to up to three different binding modes [74], [75], which are shown in Figure 1.14, namely monodentate, bidentate (bridging or chelating) and tridentate (bridging or chelating). The dominant configurations are monodentate or bidentate bridging configurations with the possibility of H-bond formation between residual M-OH groups at the metal oxide surface and unbound P=O and P-OH. The type of binding mode depends on the nature of the phosphonic acid and metal oxide, as well as the conditions of the surface modification process, such as pH and temperature [75].

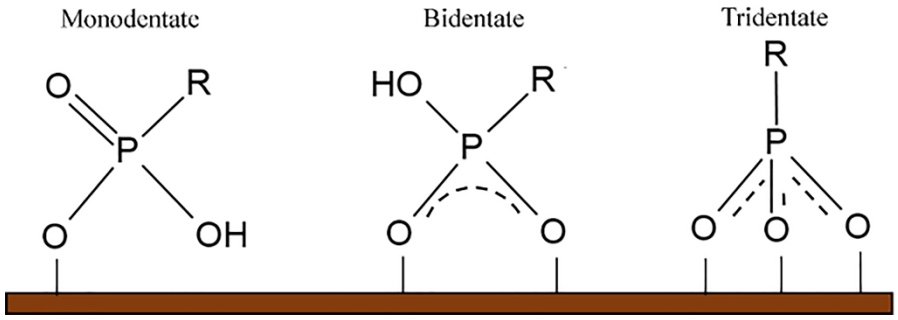

Figure 1.14: Three possible binding modes of a phosphonic group [75].

A major contribution to colloidal stability is the ligand chain. Once a ligand is bound to the iron-oxide surface, its chain interacts closely with the surrounding solvent. It is the part of a ligand that alters the surface properties (e.g., hydrophobicity) of a nanoparticle and determines the interactions between the nanoparticles and the surrounding solvent. A wide variety of ligand chains can provide colloidal stabilization in polar and nonpolar solvents or even serve as intermediate reactants for subsequent functionalization and polymerization, depending on which functional groups the ligand chain contains. Long linear chains containing 8 to 18 C-atoms (e.g., octadecylphosphonic acid (ODPA)) can be tightly packed and exhibit high grafting density [69] and are often used for the preparation of self-assembling monolayers [61], [76], [77]. VdW interactions between nonpolar alkyl chains induce an order that is higher for molecules with longer alkyl chains [78]. On the other hand, dendrimers with larger size and consequently larger steric barriers cannot assemble into a dense layer on the surface. A dilute ligand layer is desirable in some cases for colloidal stabilization of nanoparticles [71], [79], as shown by Prodanov et al. They used a combination of a dendrimer and shorter linear ligands that pack between the bulkier dendrimer molecules [71], [79] and increase colloidal stability.

1.4 Nematic Ferrofluids

Nematic ferrofluids are colloidal suspensions of magnetic nanoparticles, which possess long-range orientational ordering. The ordering can be caused either by the ordered surrounding liquid medium, i.e., liquid crystals, or by the anisotropic shape of the dispersed nanoparticles in isotropic liquids.

1.4.1 Liquid crystals

Liquid crystals (LCs) are fluids with anisotropic properties that are intermediate between ordinary liquids and solid crystals. They retain the fluidity and inability to support shear, shaping and merging of droplets, while expressing crystalline properties, such as molecular orientational and in some phases partial positional order, as well as anisotropy of electrical, optical and magnetic properties. Depending on the partial positional order of the molecules and/or their symmetry, different LC phases are known, such as nematic, cholesteric, smectic and columnar LC mesophases [80], [81].

1.4.1.1 Nematic liquid crystals

Nematic liquid crystal (NLC) mesophases consist of rod- or disk-shaped molecules that do not have a long-range positional order, but rather a long-range orientational order along the preferred direction denoted by a unit vector, a director $\mathbf{n}(\mathbf{r})$ ($\mathbf{r}$ stands for the position in space). Molecules rotate in all directions, but on average orient with their long axis along the $\mathbf{n}$. The $\mathbf{n}$ and $-\mathbf{n}$ directions are equal. The NLCs are sensitive to an electric and magnetic field. The orientation of $\mathbf{n}$ can be altered by the application of external fields (i.e., electric and magnetic) or by surface treatments of the confining boundary (e.g., from LC cells), which dictate the direction of the director at the surfaces. NLCs have at least two liquid phases that are either disordered, i.e., isotropic, or orientationally ordered, i.e., nematic phase. They may also have more ordered LC phases, as for example smectic phase. Thermotropic LCs undergo phase transition from a higher temperature isotropic phase to a lower temperature nematic phase at a certain temperature. In the isotropic phase, the molecules of NLCs have no long-range orientational or positional order, which makes them comparable to ordinary isotropic liquids. By lowering the temperature to the phase transition temperature, the molecules of LC orient on average along the director $\mathbf{n}$ and form the nematic phase. The densities of the isotropic and nematic phases are nearly identical. Further lowering of the NLC temperature causes the transition to the solid crystalline phase, where the molecules gain positional order. Figure 1.15 illustrates the ordering of an NLC. Alternatively, one or more liquid crystalline phases with partial positional order may exist between the nematic and crystalline phases.

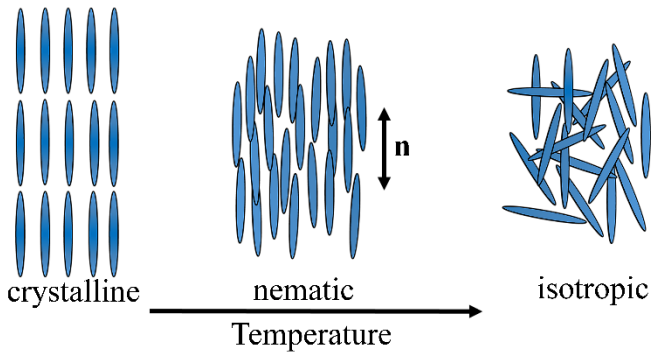

Figure 1.15: Schematic representation of orientational and positional order in the crystalline, nematic, and isotropic phases of a thermotropic LC [82]. The crystalline phase has orientational and positional order. During the phase transition to the nematic phase, the positional order is lost and during the transition to the isotropic phase, the orientational order is also lost.

1.4.1.2 Elastic properties of distorted LCs and distortions of the director field

Orientational elasticity is one of the properties that distinguish LCs from ordinary liquids. Long-range orientational order favors a uniform direction of **n** throughout the NLC. This represents the global minimum of the free energy of the system. Any deformation of **n** leads to an increase in the free energy of the system [83], and the distortion of **n** in a local region extends to a larger region. The distortion of the field leads to an increase in the elastic energy in the system, which strives to recover the original order, resulting in an elastic torque acting on **n** and forcing it to the original, uniformly ordered state. The resulting deformations are combinations of splay, twist and bend and are shown in Figure 1.16. With respect to the ordered system, in splay **n** deforms in a Japanese fan-like structure, in bend it bends, and in twist it twists in the perpendicular direction [80], [81], [83] (see Figure 1.16). The elastic constants K_1, K_2, and K_3, which correspond to the elastic distortions of splay, twist and bend, respectively, have typical values between 1 and 20 pN. A uniform orientation of **n** in the whole system gives the value of elastic energy zero, while the value changes when **n** depends on the position in the system [83].

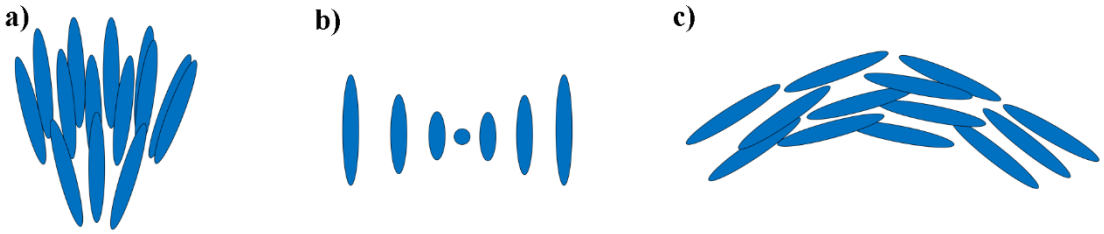

Figure 1.16: Three main types of deformations in LCs, which increase the elastic energy of the system. a) Represents splay, b) twist, and c) bend deformation [80].

1.4.1.3 Surface anchoring of LC molecules

The interaction between a surface and LC molecules is called surface anchoring. Any surface (gaseous, liquid, or solid) can affect the orientational ordering of the LC molecules, i.e., the **n**-direction. The preferred **n**-direction is referred to as the easy axis, which is denoted by a unit vector $\mathbf{n}_e$. The alignment of $\mathbf{n}_e$ on the surface can be either parallel, leading to planar anchoring, perpendicular, leading to homeotropic anchoring, or tilted. The tilted surface anchoring takes an angle between **n** and $\mathbf{n}_e$ from 0 ° to 90 °.
The surface anchoring energy $U_{\text{anchoring}}$ describes boundary conditions and is given by [83]:

$$U_{\text{anchoring}} = -\frac{1}{2} W \int (\mathbf{n}_e \cdot \mathbf{n})^2 dS \tag{1.8}$$

where W represents anchoring strength or surface energy. The anchoring strength on a substrate can also be described by a characteristic length scale, the so-called surface extrapolation length ξ, which is defined as the ratio between the elastic constant K and the anchoring strength W [83], [84]:

$$\xi = \frac{K}{W} \tag{1.9}$$

A large anchoring strength makes the extrapolation length small (on the order of a few nanometers), and **n** is equal to or very close to $\mathbf{n}_e$. A small anchoring strength leads to a large extrapolation length (up to a few micrometers). In this case, the influence of the surface on the orientation of **n** is smaller. The stable configuration of **n** around a particle that distorts the alignment compensates for elastic and surface energy [83].

The LC anchoring to larger surfaces can be controlled mechanically or chemically. Mechanical treatment such as rubbing the surfaces in one direction and washing is sufficient in most cases. For example, rubbing a polymer-layer surface with a cloth induces planar anchoring [85]. Another way to achieve the desired alignment is chemical treatment. It is the only way to change the LC anchoring on nanoparticles. Several different ways of chemically modifying the surface of nanoparticles are known and have proven successful (see Chapter 1.3.1).

1.4.1.4 Defects in LC suspensions of nanoparticles

The introduction of nanoparticles into an NLC adds a surface that distorts the **n**. The LC orientation around a nanoparticle deforms elastically, resulting in topological defects at or near the surface [81]. The elastic far field deformation of **n** around a particle in an NLC can be described as a sum of multipoles [86], analogous to the far-field distortions of electric or magnetic fields described by multipole expansion. The size and shape of the nanoparticle significantly affect the type and strength of the elastic deformation [87], [88]. Different configurations of **n** around a spherical nanoparticle are depicted in Figure 1.17. Monopoles, dipoles and quadrupoles are usually the leading-order multipoles. However, when there is no external torque acting on the embedded nanoparticle, the elastic monopole in the NLC is zero due to symmetry. Dipoles are the lowest possible order of elastic multipoles when no external fields are applied [89], [90] and are formed by spherical nanoparticles with homeotropic surface anchoring and a hedgehog point defect (see Figure 1.17a). Rotations around $\mathbf{n}_0$ (far-field uniform alignment of the **n**) have no effect on this structure, while the latter is not symmetric in the mirror plane perpendicular to the $\mathbf{n}_0$. Another elastic multipole that forms on spheres with homeotropic anchoring is a quadrupole with a disclination loop around the particle, so-called "Saturn ring" (see Figure 1.17b). Elastic quadrupoles also occur on spheres with planar anchoring (see Figure 1.17c). In this case, boojums arise as surface defects at the poles of the sphere. Quadrupoles are mirror-symmetric through the equatorial plane. A major difference between dipoles and quadrupoles is also the decrease in the elastic field. The field around a dipole decreases with a distance of $1/r^3$, while around a quadrupole it decreases with a distance of $1/r^5$ [86], [87], [91].

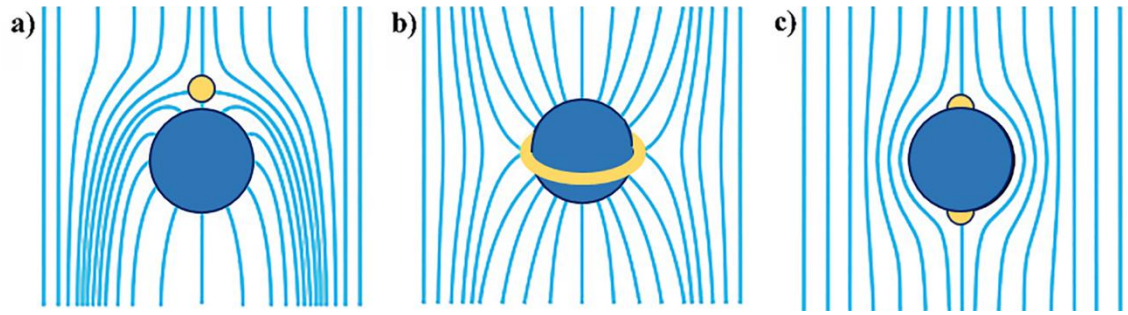

Figure 1.17: Schematic of elastic multipoles: a) the dipole, where the blue lines show the **n** configuration and the yellow dot shows the hedgehog defect, b) quadrupole with the disclination loop around the sphere's equator and axial symmetry of the **n**, c) quadrupole

with axial symmetry of the **n**, where yellow dots show two boojums at the poles of the sphere [91].

1.4.1.5 Interactions between nanoparticles in LC

The interactions between colloidal nanoparticles have already been explained in Chapter 1.2. The same interactions exist in a colloidal suspension in a LC. In an NLC, an additional nematically mediated interaction occurs due to the elastic deformations of **n** that are caused by the embedded nanoparticles [81]. The elastic deformations around two nanoparticles overlap when the nanoparticles approach each other to a certain distance. In different systems, the overlap is either energetically favorable or unfavorable. In the latter case, repulsion occurs between the particles, while in the energetically favorable case, the distance between the nanoparticles is minimized to minimize the total free energy. The distance between the nanoparticles, the type of elastic deformation, and the direction of elastic distortion are the parameters that affect the pair interaction. For example, attractive interactions exist between two elastic dipoles placed in parallel sequence to each other and between two antiparallel adjacent elastic dipoles as shown in Figure 1.18a and Figure 1.18b, respectively [92]. Elastic dipoles are most prone to the formation of chain structures [81], [89]. Elastic quadrupoles, on the other hand, attract only diagonally and can form tilted crystal-like structures, for example [81], [87], [93].

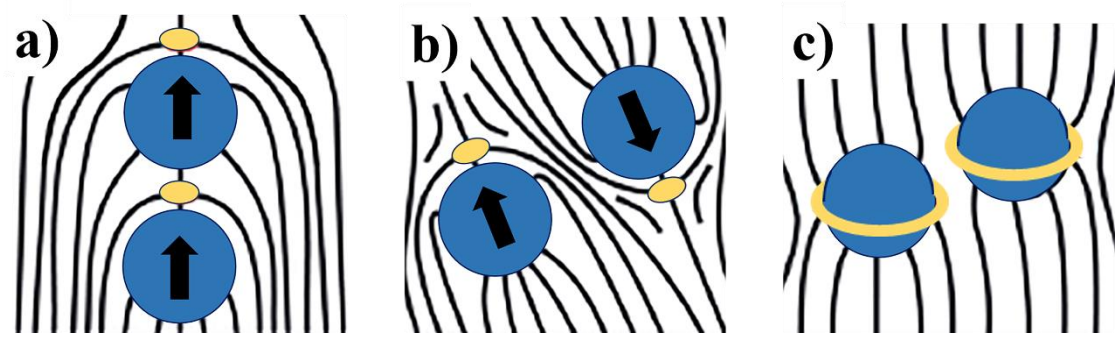

Figure 1.18: a) Formation of chain structures of two parallel elastic dipoles due to attraction along the dipoles, b) sideways attraction between two antiparallel elastic dipoles, c) two adjacent elastic quadrupoles are diagonally attracted [92]. The black lines represent the **n** configuration and the yellow dots/lines represent the defects.

1.4.1.6 Parameters affecting colloidal stability in an NLC

Nanoparticles suspended in an isotropic phase of LC are affected by interactions that also occur in other isotropic solvents. Cooling of the suspension to the nematic phase leads to ordering and nematic-mediated elastic interactions that can eventually lead to aggregation of nanoparticles. For suspended nanoparticles that disturb ordering in the nematic phase, it is energetically favorable to remain in the isotropic phase where they group and gradually form aggregates. The phase transition can lead to aggregation, which usually occurs at the phase boundary between the nematic and isotropic phases. In most cases, a successful approach to avoid aggregation is quenching (rapid cooling) of the suspension [94], [95]. This reduces the probability of aggregation during the phase transition compared to the situation during slow cooling.

The size of the nanoparticles in an NLC suspension affects the colloidal stability. Larger nanoparticles with diameter larger than 100 nm cause larger distortions of the **n**, resulting

in stronger attractive elastic interactions that lead to aggregation. Smaller nanoparticles with a diameter much smaller than 100 nm would cause the system to spend an excessive amount of energy to deform **n** [71]. This is energetically unfavorable, and therefore elastic interactions do not contribute significantly to aggregation [79]. For example, sub-micrometre spherical silica particles that induce homeotropic anchoring were used to show the effect of size on the interaction strength between particles in nematic 4-cyano-4'-pentylbiphenyl (5CB). Silica nanoparticles smaller than 100 nm formed stable structures, i.e., aggregates, but the attractive elastic interactions were negligible for the 22 nm diameter nanoparticles, where no thermally stable pairs or larger aggregates were observed [96].

The type of elastic multipole, namely dipole, quadrupole, depends on the shape of the nanoparticles. LC will spontaneously order anisotropic nanoparticles with respect to **n**. The orientation of rod-shaped and plate-shaped nanoparticles in an NLC can be tuned by the surface anchoring, where the nanoparticles orient in the direction of **n** in the case of planar anchoring, as shown in Figure 1.19a and Figure 1.19b, and have free rotation in the same direction and in the case of homeotropic anchoring they orient perpendicular to **n** (see Figure 1.19b and Figure 1.19d) [94]. Such behavior was experimentally demonstrated by Liu et al. [97]. Gold nanorods and nanoplates were surface-modified with a polymer coating that weakens the interactions between the surface of the nanoparticles and **n**, thus reducing the elastic distortions. By controlling the surface interactions, the anisotropic nanoparticles with planar surface anchoring self-aligned along **n** [97].

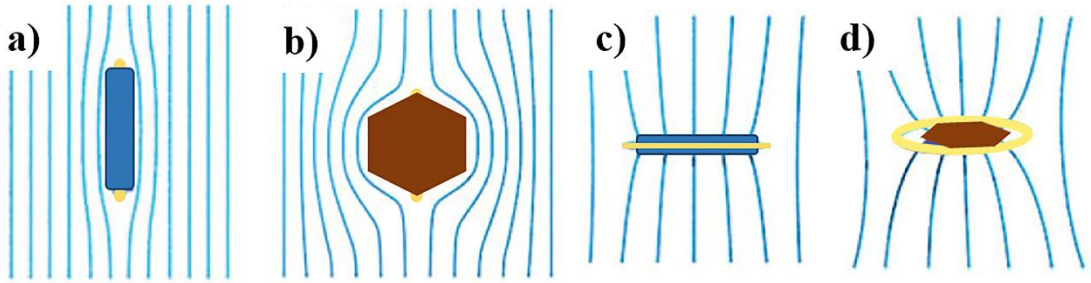

Figure 1.19: Schematic representation of the director field around rod-shaped (a, c) and plate-shaped (b, d) nanoparticles: a), b) planar and c), d) homeotropic anchoring [94]. The blue lines show the **n**-configuration and the yellow dots/lines show the defects.

The importance of surface modification for colloidal stability was discussed in 1.3.1. The modification of a nanoparticle surface affects the behavior of nanoparticles in an LC by influencing the anchoring of LC molecules [95], [98], [99]. The steric effect, electrostatic or electrosteric repulsion between nanoparticles in an LC suppresses aggregation during the phase transition [3], [71], [72]. Since the conventional methods for alignment of LC molecules, such as surface rubbing, cannot be applied to the surface of nanoparticles, chemical methods must be used.

Commonly used surface ligands for colloidal stabilization in NLCs have long linear chains, which may be part of a dendritic structure, for example. The latter affects the ordering of LC molecules, their elastic properties and also the phase transitions [72]. LCs contain so-called mesogenic units responsible for the LC properties. For example, the thermotropic LC 5CB has a rigid mesogenic biphenyl unit, shown in Figure 1.20. Surface ligands that have similar units to mesogenic unit (promesogenic units, i.e., PMUs) as part of the whole structure have been shown to greatly enhance the colloidal stability of nanoparticles in LCs [71], [72], [79], [100], [101]. Such ligands are called promesogenic

ligands. Not only do they provide steric repulsion through a large exclusion volume, but the long chains can also smooth out the disturbance of **n** [79]. Promesogenic ligand molecules consist of an anchoring group, mesogenic units, and one or more spacers to elongate the structure of the ligand, as is depicted in Figure 1.20 [70], [72], [79]. Different functionalities, chain structures and branching of promesogenic ligands affect the behavior of NLC suspensions.

Studies have shown that surface ligands must be selected not only with respect to the desired interaction with the LC molecules, but also taking into account the shape of the nanoparticles. The importance of ligand structure was demonstrated on needle-like ferromagnetic nanoparticles dispersed in 5CB. A linear and a dendritic ligand with the same (cyanobiphenyl) functionalities and anchoring group resulted in different colloidal stability for spherical or needle-like nanoparticles. The needle-like nanoparticles were stabilized by the linear ligand, while the dendritic ligand did not provide colloidal stability [72]. Nevertheless, aggregates occurred even in the case of linear-ligand-modification [72]. On the other hand, dendritic promesogenic ligands in combination with shorter linear ligands allowed the stabilization of spherical CdSe/ZnS nanoparticles in nematic 5CB [79]. The diluting of the dendrimer layer allowed the flexibility of the dendritic ligands and enabled the LC molecules to penetrate deeper into the ligand layer, which reduced the distortions of **n** and decreased the orientational energy, as shown in Figure 1.21 [72], [79]. It has been shown that diluting the layer of dendritic promesogenic surface ligands is a good approach to achieve the colloidal stability of spherical nanoparticles in an NLC [71], [79].

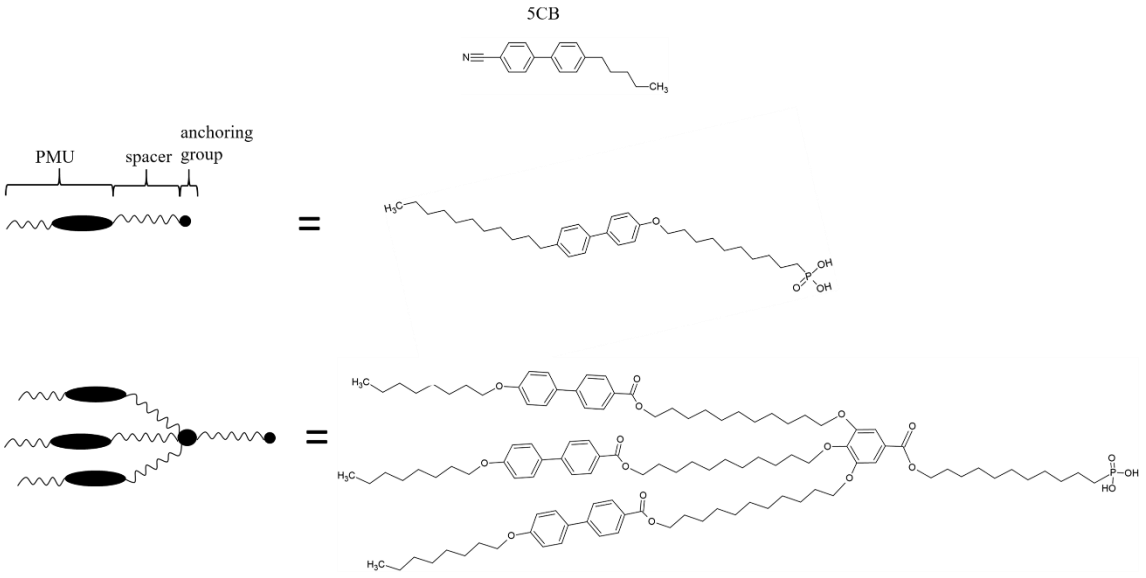

Figure 1.20: Molecular structure of 5CB and the schematic representation of linear and dendritic ligands with an example of chemical structure [70].

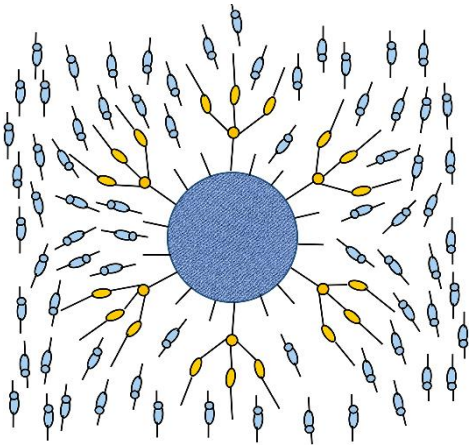

Figure 1.21: Schematic representation of the alignment of LC molecules around a spherical nanoparticle with modified surface using a combination of dendrimer and short alkyl ligand [79].

The density of the surface layer is not the only factor affecting colloidal stability [101]. It has been shown that there is an optimal length of linear promesogenic ligands that enables colloidal stability in NLCs [101]. Relatively long ligand chains (e.g., C-10) increase the excluded volume and steric repulsion between nanoparticles, while smoothing the disturbances of **n**. By elongating the linear promesogenic ligands above C-15, the structure becomes less similar to LC (5CB), which negatively affects the colloidal stability of the spherical nanoparticles. In addition, combinations of different promesogenic ligands have been shown to significantly affect colloidal stabilization. Mesogenic units with a nitrile group facing the nematic medium, as depicted in Figure 1.22, were found to be favorable for colloidal stability. On the other hand, ligands ending with an octyl tail did not enable colloidal stability and the surface layer had to be diluted with shorter linear ligands, as was also observed for dendrimers (see previous paragraph). However, the facts mentioned in this paragraph were shown only for very small (2.5 nm) cobalt ferrite nanoparticles [101].

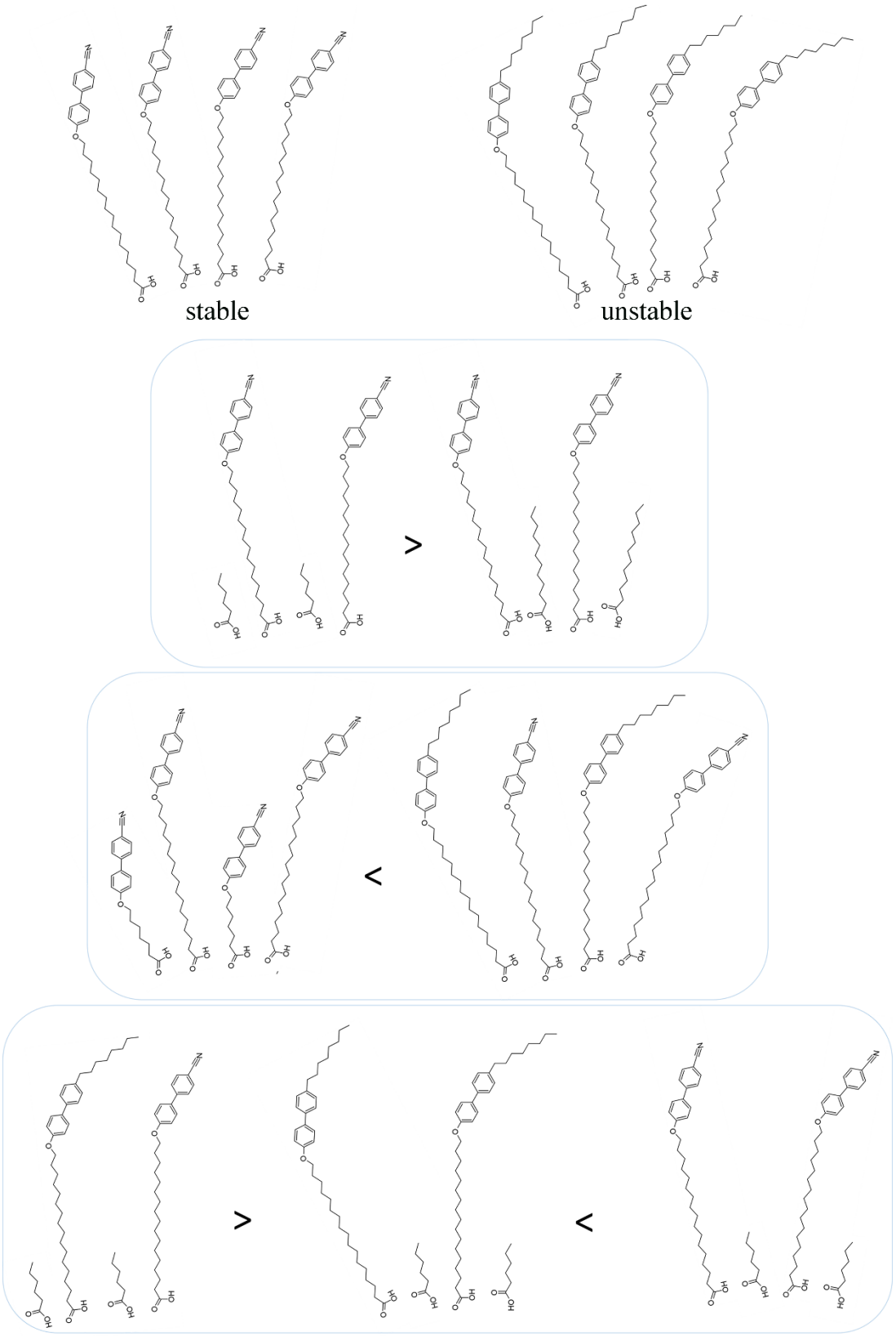

Figure 1.22: Schematic representation of different combinations of promesogenic ligands on a spherical nanoparticle surface, where < and > indicate the enhancement of colloidal stability of the as-modified spherical nanoparticle surface in nematic 5CB [101].

NLC suspensions of magnetic nanoparticles are of great interest due to their magneto-optic (MO) responsiveness [72], [102]–[104]. Additional attractive magnetic dipole-dipole interactions (see Chapter 1.2.7) present a challenge to colloidal stability in NLCs, and surface ligands that provide colloidal stabilization of nonmagnetic nanoparticles may not be efficient enough to prevent aggregation of magnetic nanoparticles [72]. The magnetic dipole-dipole interaction between the magnetic nanoparticles in the suspensions may lead to the formation of chains, resulting in the well-known magneto-viscous effect in ferrofluids. To avoid the formation of chains in an NLC host, it is better to choose nanoparticles with a quadrupolar nematic-mediated elastic interaction, as depicted in Figure 1.23. Thus, we counteract the attractive dipole-dipole interactions along the directions of magnetic moments. Surface modification of the ferrimagnetic BHF NPLs with dodecylbenzenesulfonic acid (DBSA) enables sufficient electrosteric repulsion between the NPLs. This ensures order in nematic 5CB and the formation of a ferromagnetic nematic phase, leading to a large MO response [3]. The homeotropic anchoring induced by the DBSA surface modification leads to an alignment of the NPLs with the magnetic moments parallel to **n**, as depicted in Figure 1.23. With such an alignment of the NPLs, the magnetic moments can be directed either upward or downward. The realignment of the NPLs is only possible when the NLC undergoes the phase transition to the isotropic phase, but the dispersed NPLs can still flow. Flowing in the NLC suspension does not change the topological structure. Nevertheless, the formation of regions where the magnetic moments of the NPLs are aligned in the same direction, i.e., magnetic domains may occur [3], [94].

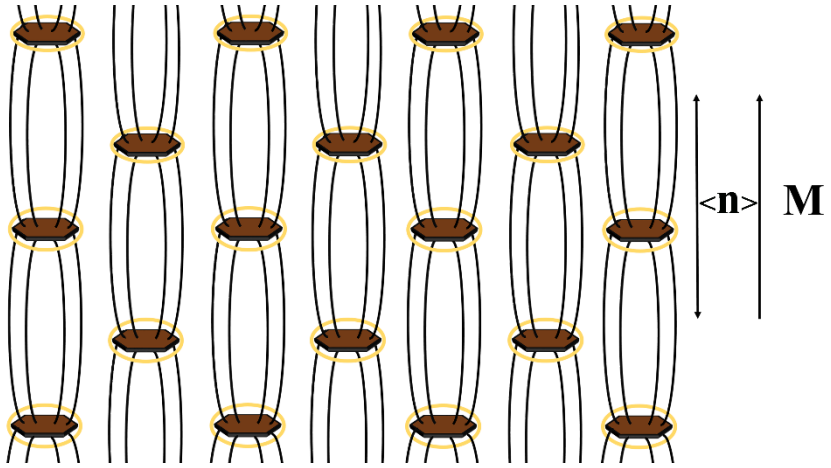

Figure 1.23: Schematic representation of the magnetic BHF NPLs in the NLC 5CB [3]. The black lines show the **n** configuration and the yellow lines represent the defects.

1.4.2 Nematic ordering of (nano)particles in isotropic solvents

Nematic ordering, i.e., the LC behavior of particles in isotropic solvents, was first observed in the early 20th century [105]–[107]. The isotropic-nematic separation was found in suspensions with different particles that had one crucial feature in common – they were all anisotropic. The nematic ordering of particles in isotropic solvents was first discovered in suspensions of vanadium pentoxide rod-shaped particles [106], tobacco mosaic rod-shaped virus [107] and plate-shaped bentonite clay particles [105]. Since then, several systems with anisotropic particles of different materials, such as gibbsite [108]–[110] and clay platelets [111]–[114] have been studied.

In colloidal suspensions of anisotropic particles, orientational correlations between neighboring particles affect the phase behavior of the suspensions, i.e., the phase transitions [115]. A theoretical explanation for the ordering of rod-shaped particles from the isotropic to the nematic phase was given by Onsager [115]. The nematic ordering may arise from a competition between orientational and packing entropy controlled by excluded-volume interactions [115]. At a sufficiently high concentration, the packing entropy favoring the nematic phase outweighs the orientational entropy favoring the isotropic phase. The nematic ordering can only be caused by the shape anisotropy of the particles [115]. The proposed explanation for the nematic ordering was also confirmed for the plate-shaped particle suspensions [116]–[118]. The effective aspect ratio of the particles, i.e., the ratio between thickness and diameter, is an important parameter affecting the phase behavior and can be tuned by the surface charge of the particles and the ionic strength of the suspension [110], [119]. Higher ionic strength of the suspension makes the particles more anisotropic by affecting their effective size. The size of the particles becomes effectively larger for approximately the value of Debye screening length and in the case of platelets the effective diameter D_{eff} is [115]:

$$D_{\text{eff}} = D + 2\left(\kappa^{-1}\right) \tag{1.10}$$

where D is the equivalent diameter (i.e., a disk diameter with an area equal to the basal surface of the platelet). The effective thickness of platelets h_{eff} is [115]:

$$h_{\text{eff}} = h + 2\left(\kappa^{-1}\right) \tag{1.11}$$

where h is the thickness of a platelet. Platelet suspensions can order in different LC phases. For example, lamellar and columnar phases have been predicted and observed in systems of nonmagnetic platelets [110], [116], [120]. The suspensions undergo the phase transition from isotropic to a more ordered phase at a certain, usually experimentally determined, threshold volume fraction ϕ_{IN}:

$$\phi_{\text{IN}} = \frac{N}{V_{\text{s}}}\langle V_{\text{i}}\rangle \tag{1.12}$$

where N/V_{s} is the number density of the particles and V_{i} is the volume of a platelet. The term threshold volume fraction is used in the rest of the text as the volume fraction (of particles) of the phase transition in isotropic solvents. Computer simulations have shown that thin nonmagnetic platelets without surface charge undergo the isotropic-nematic phase transition at an effective volume fraction between 3 and 4, with the value depending on the shape of the platelets (i.e., hexagonal, triangular, circular, etc., shape of the basal plane) [110], [121], [122]. The effective volume fraction $\phi_{\text{IN,eff}}$, also known as the dimensionless transition density, is calculated as follows:

$$\phi_{\text{IN,eff}} = \frac{N}{V_{\text{s}}}\left\langle D^3\right\rangle \tag{1.13}$$

The effective volume fraction is related to the excluded volume. For example, monodisperse platelets with aspect ratio $h/D > 1/7$ have been shown to undergo a direct phase transition from isotropic to columnar phase [116].

The surface charge has an important effect on the phase behavior, as the platelets with a surface charge become effectively larger for the value of Debye screening length in all directions. Consequently, after being rescaled by taking into account the Debye screening length, the effective volume fraction becomes larger, while the effective aspect ratio of the platelets becomes smaller [110], [114]. It has been shown that electrostatic repulsion in an intermediate range, where the Debye parameter κD is ~ 30–100, is favorable for the formation of the nematic phase at the expense of destabilization of the columnar phase [118]. In contrast, longer-ranged repulsions destabilize the nematic phase in favor of the lamellar phase. The strength and range of the electrostatic interaction can therefore be used to control the existence of different LC phases, namely nematic, lamellar (smectic), and columnar, as shown in Figure 1.24 [118].

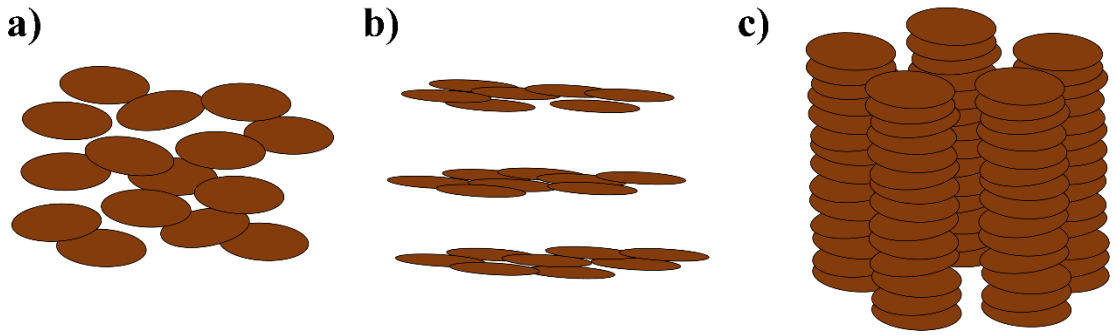

Figure 1.24: Schematic representation of a) nematic, b) lamellar or smectic, and c) columnar LC phase [108].

1.4.2.1 Nematic ordering of magnetic NPLs in isotropic solvent

The first observed ferromagnetic nematic phase, i.e., a liquid magnet made of DBSA-modified BHF NPLs suspended in 1-butanol, was formed at a volume fraction of $\phi > 28$ % [123]. In the case of BHF NPLs, the aspect ratio is not the only parameter affecting the nematic ordering. The contribution of electrostatic and magnetic interactions in the suspensions is considerable. The platelet shape together with the anisotropic screened electrostatic interaction promotes the ferromagnetic nematic ordering [124]. Moreover, strong positional and orientational correlations between NPLs are present both in the nematic phase and in isotropic dilute suspensions [124]. This can be attributed to magnetic and electrostatic interactions between the NPLs. The neighboring NPLs prefer positions, where the magnetic moments are parallel to each other and it is more likely that the NPLs form a magnetically ordered phase than spheres [124]. BHF NPLs are polydisperse in diameter, which can cause another structural force [94]. A higher concentration of smaller NPLs with a small magnetic moment around larger ones causes additional short-range entropic-like repulsion [94].

The ferromagnetic ferrofluids of BHF NPLs are very sensitive to an external magnetic field [123] and are usually studied in zero field. This means that the influence of the ambient magnetic field (e.g., the Earth's) is eliminated by suitable shielding [123]. The behavior of ferromagnetic nematic suspensions of BHF NPLs is very close to that of an ideal soft magnetic material. In the zero field, the NPLs form a closure-domain structure to minimize the magnetic field energy [94]. A simple example of a closure-domain structure in a rectangular solid layer of a soft ferromagnet is shown in Figure 1.3 [18], [19], [123]. Similar

domain structures have been observed in ferromagnetic ferrofluids of BHF NPLs with a volume fraction of NPLs $\phi > 28$ % [123].

Chapter 2

Aims and Hypothesis

2.1 Aims

The goal of this dissertation is to investigate and determine some systems that allow the preparation of colloidally stable ferromagnetic liquids with barium hexaferrite nanoplatelets, preferably with ferromagnetic coupling between the BHF NPLs. One way to achieve this is to use the surfactant DBSA. We investigated the mechanisms for stabilization of BHF NPLs modified with DBSA and the role of electrostatic forces in different alcohols. DBSA affects several parameters, such as the surface charge, ionic strength, Debye screening length, and consequently the electrostatic interaction between NPLs. Our first goal was to determine how the electrostatic interaction and colloidal stability of the suspensions are affected by the concentration of DBSA in the suspension and the dielectric constant of the solvent. This allowed us to determine and select the best alcohol for the preparation of a liquid magnet. The second goal was to investigate how the electrostatic and magnetic interactions affect the phase behavior of highly concentrated suspensions of the BHF NPLs. The change in DBSA concentration allowed us to study the influence of electrostatic interaction on the threshold volume fraction of the NPLs for the formation of nematic phase. The influence of the magnetic interaction was determined by changing the magnetization and the average equivalent diameter of the NPLs. An important parameter in the formation of the nematic phase is also the shape anisotropy, i.e., the effective ratio between the thickness and the diameter of the NPLs. The third goal was to achieve colloidal stability of ferrofluids of NPLs also in non-alcoholic isotropic solvents and to extend the understanding of stability mechanisms to achieve high concentrations of BHF NPLs even in NLC hosts. Particular attention was paid to surface-modifying ligands with a phosphonic functional group.

2.2 Hypothesis

The hypotheses based on the three goals presented in the previous section are the following:

- The concentration of dissolved DBSA in the alcohol suspensions of the BHF NPLs affects the ionic strength and the Debye screening length. The Debye length also depends on the type of alcohol and affects the colloidal stability in different alcohols. Thus, there is an optimal concentration of DBSA in a particular alcohol.
- In a particular alcohol selected for the preparation of a ferromagnetic ferrofluid and the evaluation of its phase behavior a stronger magnetic interaction between the NPLs leads to a decrease in the threshold volume fraction for the isotropic-nematic phase transition. In contrast, the electrostatic interaction plays a threefold role by affecting the excluded volume, the effective magnetic interaction, and the

effective shape anisotropy, thus affecting the isotropic-nematic threshold volume fraction.

- The fundamental understanding of interplatelet interactions in isotropic alcohol suspensions gained through the first two goals of this dissertation enables the preparation of stable colloidal suspensions in non-alcoholic solvents and in nematic hosts as well.

Chapter 3

Materials and Methods

3.1 Materials

Chemicals used for synthesis, surface modification of NPLs, and preparation of NPL suspensions were used as received without additional purification.

The following salts, acids and bases were used for the synthesis of the studied materials:

- Barium nitrate (99.95 %), Alfa Aesar
- Iron(III) nitrate nonahydrate (98+ %), Alfa Aesar
- Scandium(III) nitrate hydrate (99.9 %), Alfa Aesar
- Indium(III) nitrate hydrate (99.99 %), Alfa Aesar
- Nitric(V) acid (65 %), Sigma-Aldrich
- Sodium hydroxide (98 %), Alfa Aesar
- Ammonia solution (25 %), Merck

The following surface-modifying ligands were used and their molecular structures are presented in Figure 3.1:

- Dodecylbenzenesulfonic acid (DBSA) (97 %), Alfa Aesar
- 16-phosphonohexadecanoic acid (PHDA) (97 %), Sigma-Aldrich
- (2-{2-[2-Methoxy-ethoxy]-ethoxy}-ethyl)phosphonic acid (Pether) ($\geq$ 97 %), Sikemia
- Oleic acid (OA) (90 %), Alfa Aesar
- Ricinoleic acid (RA) ($>$ 80 %), Tokyo Chemical Industry Co. Ltd
- Dendrimer, kindly provided by Dr. Zois Syrgiannis, University of Trieste
- Hexylphosphonic acid (HPA) (95 %), Sigma-Aldrich
- Octadecylphosphonic acid (ODPA) (97 %), Sigma-Aldrich
- Alendronate sodium trihydrate (AL) (97 %), Alfa Aesar
- {[4'-cyano[1,1'-biphenyl]-4-yl)oxy]decyl}phosphonic acid (10POCB), kindly provided by Dr. Martin Cigl, FZU-Institute of Physics of the Czech Academy of Sciences
- (12-phosphono)dodecyl sulphonic acid (PSA) ($\geq$ 97 %), Sikemia

The following solvents were used:

- Deionized water
- Acetone (99.8 %), Carlo Erba Reagents
- *tert*-butanol (99.5 %), Emsure Merck
- 1-hexanol (99 %), Alfa Aesar
- 1-butanol (99.4 %), Baker Analyzed

- 2-propanol (99.9 %), Carlo Erba
- Toluene (≥ 99.5 %), VWR Chemicals BDH®
- Chloroform (≥ 99 %), Carlo Erba Reagents
- Methanol (≥ 99.9 %), Carlo Erba Reagents
- Tetrahydrofuran (THF) (100.0 %), VWR Chemicals BDH®
- Ethanol (99.5 %), Carlo Erba Reagents
- Dimethyl sulfoxide (DMSO) (≥ 99.5 %), Sigma-Aldrich

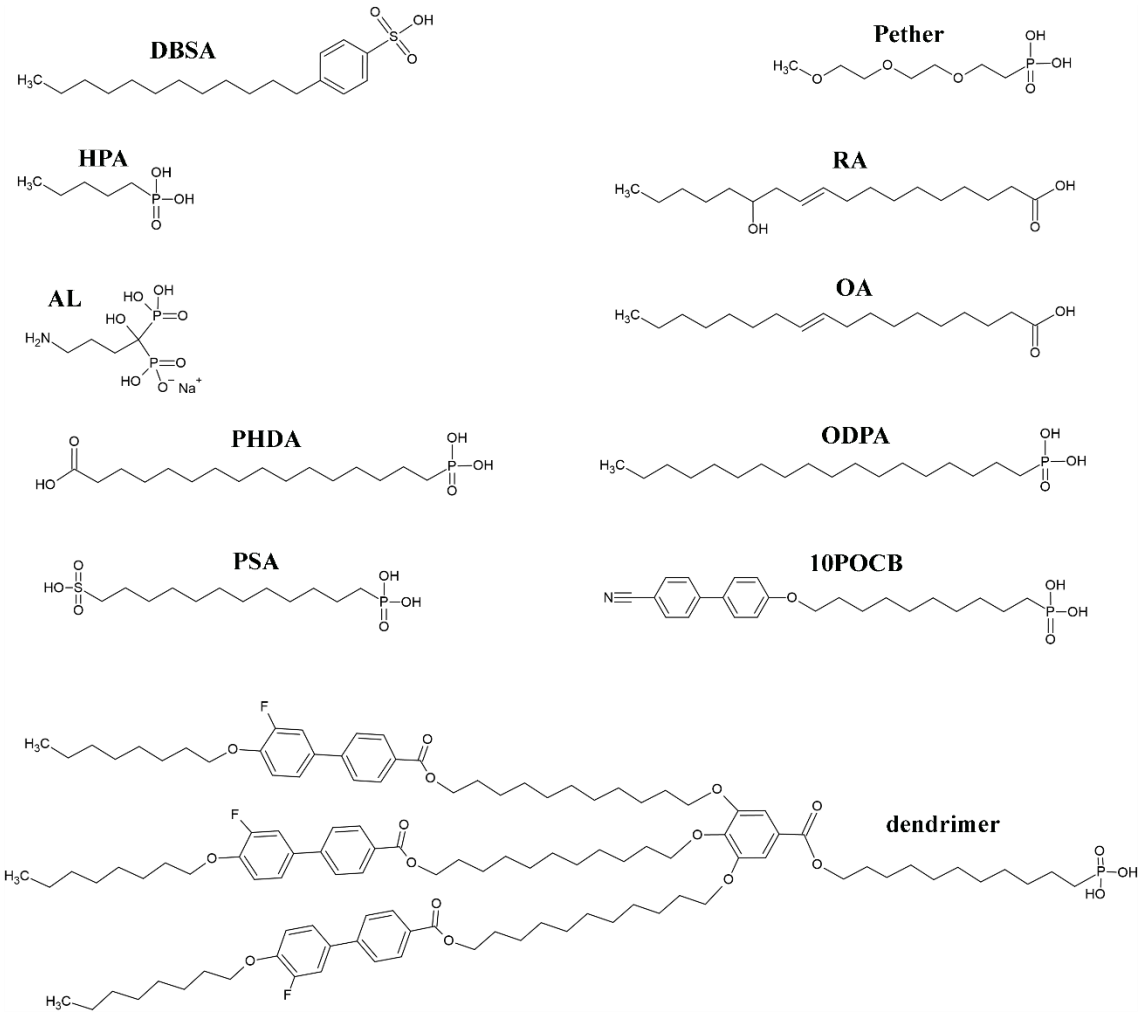

Figure 3.1: Molecular structures of the different ligands used for the surface modification of the BHF NPLs.

3.2 Synthesis of the BHF NPLs, Surface Modification and Preparation of the Suspensions

3.2.1 Hydrothermal synthesis of the bare BHF NPLs

The scandium and indium substituted BHF NPLs were hydrothermally synthesized in an Inconel autoclave (Parr Instrument Co.), as shown in Figure 3.2, following a well-established procedure [43]. Sc^{3+} and In^{3+} ions partially substitute Fe^{3+} and also some Ba^{2+}

resulting in ion vacancies (see Chapter 1.1.3). The difference between the Sc- and In-substituted sample is the saturation magnetization of the NPLs, which was the reason for the synthesis of both types of NPLs. Barium, iron(III) and either scandium(III) or indium(III) nitrates were dissolved in water in a molar ratio of 1:4.5:0.5. An excess of sodium hydroxide (to obtain 2.7 M) was added to precipitate the precursor from water. The mixture was poured into the autoclave and heated to 245 °C at a heating rate of 3 °C/min. The pressure in the autoclave increased accordingly to ~ 3.6 MPa. The mixture was immediately cooled naturally to room temperature. The NPLs prepared in this way were sedimented by centrifugation (Centrifuge 5804, Eppendorf) and washed three times with water and once with nitric acid at a pH 0.77. The final product was dispersed in water and maintained a low pH of about 2.5. The suspension was treated with an ultrasonic probe (Sonics Vibra-Cell) for 1 min at 200 W.

Figure 3.2: The autoclave used for the hydrothermal synthesis.

3.2.2 Synthesis of BHF-DBSA NPLs

The basic synthesis of DBSA-modified NPLs is similar to the procedure described in Chapter 3.2.1 and differs in a few steps after the precipitation, as described in [62]. After the precipitation of the precursor from water, DBSA was added to the mixture to obtain 23 mM and stirred for 30 minutes. The mixture was transferred to the autoclave and heated as described in Chapter 3.2.1. After cooling, the NPLs were centrifuged and washed twice with water. The NPLs were dispersed in water, the pH was adjusted to 1.5 with 5 M nitric acid, and the mixture was refluxed at 100 °C for 2 h. When the mixture cooled to room temperature, the NPLs were washed twice with water and once with acetone and dried at 60 °C to remove any acetone residue.

3.2.3 Surface modification of the bare NPLs with different surface-modifying ligands

The surface modifications described in this chapter were carried out after the original synthesis of the NPLs (described in Chapter 3.2.1). The as-synthesized NPLs were suspended in water at an acidic pH between 2 and 3. This was the initial suspension for all surface modification procedures described in the following text. The surface

modifications were performed using various ligands, whose molecular structures are depicted in Figure 3.1.

BHF-DBSA NPLs in water

DBSA solution in water (0.4 g in 50 ml) was added to the aqueous suspension of bare BHF NPLs (0.19 g NPLs) to reach a total volume of the mixture of 50 ml. The calculated number of DBSA molecules per surface of the BHF NPLs was 36 molecules/nm^2. The mixture was heated to 100 °C and stirred for 2.5 h. The NPLs were sedimented at 10621 relative centrifugal force (RCF) for 15 minutes (Centrifuge 5430, Eppendorf), washed three times with water and dispersed in water. Part of the NPLs sedimented and the stable suspension had a concentration of less than 10 g/l.

BHF-PSA NPLs

Surface modification was performed as described in [69]. 56 mg of PSA was dissolved in water (100 ml) and the suspension of NPLs in water was added (2.73 ml, 50 mg NPLs) to have 20 molecules/nm^2. The mixture was refluxed for 2 h at 80 °C. The NPLs were then collected from the cooled mixture with centrifugation and washed five times with water. Finally, the NPLs were dispersed in water. The pH of the suspension was adjusted to 10 with a 25 % NH_4OH solution. The suspension was treated with an ultrasonic probe with a pulse 1 s on, 1 s off, and a power of 150 W. A suspension in water prepared in this way was colloidally stable at a concentration of up to 5 g/l [69].

The surface modification for the final suspension in 1-butanol was similar to that described above. The modified NPLs were washed four times with water and once with acetone to remove residual water before the NPLs were dispersed in 1-butanol. The suspension was treated with an ultrasonic probe with a pulse of 1 s on, 1 s off and a power of 150 W for 1 min.

BHF-PHDA NPLs

0.152 g PHDA was dissolved in a mixture of toluene and DMSO in a volume ratio of 4:1 (total 120 ml) and the aqueous suspension of NPLs was added (7.5 ml, 150 mg NPLs) to give an excess of 17 molecules PHDA/nm^2. The mixture was heated to 50 °C for 2 h during vigorous stirring. The NPLs remained in the aqueous phase. The NPLs were washed four times with DMSO and four times with water to remove any residues of DMSO. The NPLs were dispersed in water, and a low concentration of the NPLs (< 3 g/L) remained stable after centrifugation at 1097 RCF for 3 minutes.

BHF-Pether NPLs

With ligand exchange procedure:

Pether (0.28 mmol, 30 molecules/nm^2) was dissolved in *tert*-butanol, and the suspension of BHF-DBSA (50 mg NPLs) in *tert*-butanol (prepared with procedure described in Chapter 3.2.2) was added to the solution to give a total volume of the mixture of 150 ml. The mixture was heated to 50 °C and stirred overnight. The NPLs were sedimented on a magnet, washed twice with 1-butanol and dispersed in 1-butanol. Some of the NPLs sedimented and the remaining suspension had a concentration below 10 g/l.

With direct surface modification:

The aqueous suspension of bare NPLs (47 mg) was diluted to 180 ml (0.26 g/l) and 20 ml of an aqueous solution of Pether (4.3 mM) was added (10 molecules/nm^2). The pH of the mixture was lowered from pH 6 to pH 4. The mixture was heated to 60 °C and stirred overnight. The NPLs were sedimented at 11000 RCF for 20 min, washed twice with water and dispersed in water, forming a colloidally stable suspension.

BHF-OA NPLs

The BHF-OA NPLs were prepared with minor modifications to the previously published procedure [65]. An aqueous suspension of the NPLs (0.25 g NPLs) was slowly added to an ammonia solution with a pH of 10–11. The suspension was then heated to 60 °C and OA (0.25 g) dissolved in a small amount of methanol was slowly added (within 30 min), the total volume of the mixture being 50 ml (18 molecules/nm^2). The pH of the suspension had to be kept between 10 and 11 during these first two steps. Then the reaction mixture was cooled, and 5 M nitric acid was added to lower the pH. The NPLs started to flocculate and were easily separated from the solvent. The NPLs were washed three times with water and twice with methanol and dispersed in chloroform. The suspension remained stable at a concentration below 3 g/l after some of the NPLs had sedimented.

BHF-RA NPLs (1)

The BHF-RA NPLs were prepared according to a previously published procedure [65]. An aqueous suspension of NPLs (0.44 g NPLs) was slowly added to 20 ml of ammonia solution with a pH of 10.97. The suspension was then heated to 60 °C and RA (0.44 g) dissolved in a small amount of acetone was slowly added (19 molecules/nm^2). The pH of the suspension had to be kept between 10 and 11 during these first two steps. The reaction mixture was mixed for 20 min. With the addition of 5 M nitric acid to lower the pH, the NPLs started to flocculate and were easily separated from the solvent. The NPLs were washed with water, acetone, methanol and again with acetone. Finally, the BHF-RA NPLs were dispersed in toluene. The NPLs remained colloidally stable at a concentration below 2 g/l after some of the NPLs had sedimented.

BHF-RA NPLs (2)

The BHF-RA NPLs (2) were prepared with minor modifications to the previously published procedure [65]. An aqueous suspension of the NPLs (0.25 g NPLs) was slowly added to an ammonia solution with a pH 10–11. The suspension was then heated to 60 °C and RA (0.25 g) dissolved in a small amount of methanol was slowly added (in 30 min), the total volume of the mixture being 50 ml (19 molecules/nm^2). The pH of the suspension had to be kept between 10 and 11 during these first two steps. Then the reaction mixture was cooled, and 5 M nitric acid was added to lower the pH. The NPLs started to flocculate and were easily separated from the solvent. The NPLs were washed three times with water and twice with methanol and dispersed in chloroform. The suspension remained stable at a concentration below 3 g/l.

BHF-dendrimer NPLs

Surface modification took place at a phase boundary between nonpolar and polar solvent. 178 mg of dendrimer was dissolved in 100 ml of toluene (25 molecules/nm^2) and the aqueous suspension (100 ml) of BHF NPLs (20 mg NPLs) was added. The mixture was stirred at room temperature for 12 h and at 50 °C for another 2h. An obvious evidence that the reaction was completed was the change in the color of the organic and aqueous phases; the brown NPLs transferred to toluene when their surface was covered with the ligands and made the surface of the NPLs nonpolar as schematically shown in Figure 3.3. The cooled reaction mixture was transferred to a separating funnel and separated. The organic part (toluene) containing the modified NPLs was sedimented and washed. Washing with toluene was repeated three times after precipitation by centrifugation [71]. Finally, the NPLs were dispersed in toluene with some of the NPLs sedimenting and the remaining stable suspension having a very low concentration of less than 1 g/l.

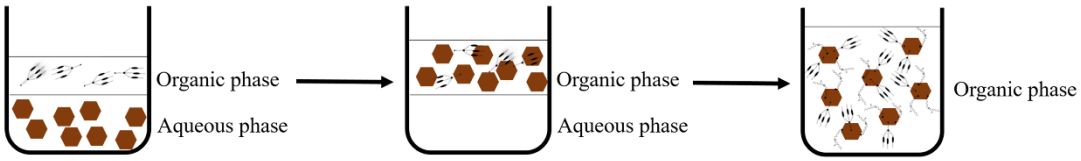

Figure 3.3: Schematic representation of the surface modification at an oil-water interface. Initially, the NPLs are in the aqueous phase (bottom) and the ligand is in the organic phase (top). During surface modification, the hydrophobized NPLs are transferred to the organic phase (top) and separated from the remaining transparent water.

BHF-RA-dendrimer NPLs

30 mg of the dendrimer was dissolved in 2 ml of toluene (12 molecules/nm^2), and two drops of pyridine were added together with the toluene suspension BHF-RA (5 ml, 7 mg NPLs) prepared according to procedure (1). The mixture was flushed with Ar and refluxed at 50 °C for 12 h. The NPLs were then separated from the other species by the addition of ethanol and centrifugation. They were washed twice with toluene and finally dispersed in toluene. A part of the dispersed NPLs sedimented and the concentration of the stable suspension was very low, only estimated to ~ 1 g/l before transferring the NPLs to 5CB.

BHF-HPA-dendrimer NPLs

Surface modification took place at a phase boundary between nonpolar and polar solvent. Dendrimer (20 mg) and HPA (9 mg) in a molar ratio 1:5 (equivalent to 4:20 molecules/nm^2) were dissolved in 10 ml of toluene with a small addition of pyridine. The solution was added to a dilute suspension of the NPLs (10.7 ml, 15 mg NPLs) in water. The mixture with a visible phase boundary was flushed with Ar and refluxed for 24 h at room temperature and 2 h at 50 °C. An obvious evidence that the reaction was finished was the change in the color of the organic and aqueous phases; the brown NPLs transferred to toluene when their surface was covered with the ligands and made the surface of the NPLs nonpolar. The cooled reaction mixture was transferred to a separating funnel and separated. The organic part (toluene) containing the modified NPLs was sedimented and washed. The washing with toluene was repeated twice after precipitation with ethanol and centrifugation [71]. Finally, the NPLs were dispersed in toluene [71], where a part of the NPLs sedimented and the concentration of the suspension was very low, only estimated to ~ 1 g/l before transferring the NPLs to 5CB.

BHF-ODPA-dendrimer NPLs

A solution of ODPA (0.7 mg) and dendrimer (15 mg) (1:4 molecules/nm^2) in a mixture of toluene and 1-hexanol (volume ratio 3:1) in a total volume of 7 ml was added to a suspension of BHF-NPLs in water (5 ml, 15 mg NPLs). The reaction mixture with a visible phase boundary between nonpolar and polar solvent was stirred for 2 h at room temperature. The reaction indicated the end when all NPLs were transferred from water to the organic solvent. Precipitation of the modified NPLs was performed with ethanol and centrifugation. The NPLs were washed with toluene. The washing procedure was repeated three times, and the NPLs were dispersed in toluene, where they were treated with an ultrasonic probe with a pulse of 1 s on, 1 s off for 1 min at a power of 100 W. The suspension remained colloidally stable at a low concentration ~ 1 g/l, because a part of the NPLs sedimented.

BHF-10POCB NPLs

73 mg 10POCB (20 molecules/nm^2) was dissolved in a mixture of THF and H_2O (volume ratio 1:2, 125 ml). BHF NPLs in water (2.73 ml, 50 mg NPLs) were added to the solution of 10POCB and refluxed for 4.5 h at 55 °C. The NPLs were collected from the cooled mixture by centrifugation and washed three times with a mixture of THF and H_2O and once with THF. Finally, the NPLs were dispersed in ethanol to form a stable colloidal suspension with a very low concentration below 1 g/l.

BHF-10POCB-AL NPLs

10POCB:AL 1:1

25 mg 10POCB and 20 mg AL (1:1 ratio, 7:7 molecules/nm^2) were dissolved in a mixture of THF and water (volume ratio 2:1, 60 ml), and BHF NPLs (2.73 ml, 50 mg NPLs) in water were added. After the mixture was refluxed at 52 °C for 2 h, the NPLs were collected by centrifugation, washed five times with a mixture of THF and water (volume ratio 2:1) and three times with THF to remove any water residues. The washed product was dispersed in THF and ethanol, where a part of the NPLs remained colloidally stable only in ethanol at a very low concentration. The NPLs were then directly transferred into isotropic 5CB from THF and ethanol.

10POCB:AL 3:1 NPLs

76 mg 10POCB and 20 mg AL (3:1 ratio, 21:7 molecules/nm^2) were dissolved in a mixture of THF and water (volume ratio 2:1), and BHF NPLs (2.73 ml, 50 mg NPLs) in water were added. After the mixture was refluxed at 55 °C for 2 h, the NPLs were collected by centrifugation and washed four times with a mixture of THF and water (volume ratio 2:1), once with water and once with THF. The washed product was dispersed in THF and in ethanol and some of the NPLs remained colloidally stable only in ethanol at a very low concentration. The NPLs were then directly transferred into isotropic 5CB from THF and ethanol.

BHF-PSA-10POCB NPLs

24.1 mg 10POCB was dissolved in a mixture of THF and water (volume ratio 2:1) and 7 ml of the aqueous suspension of BHF-PSA NPLs (as prepared according to the procedure described in the beginning of Chapter 3.2.3) with a concentration of 2.4 g/l was added. The reaction mixture was refluxed at 50 °C for 2 h. The NPLs were then collected from the cooled mixture by centrifugation and washed three times with a mixture of THF and H_2O (volume ratio 4:1), once with water and once with THF. The NPLs were dispersed in THF, where they did not form a stable colloidal suspension but were immediately transferred to isotropic 5CB.

3.2.4 Preparation of suspensions for detailed analyses

Suspensions for evaluation of electrostatic interaction

The dried DBSA-modified NPLs (prepared with the procedure in 3.2.2) were dispersed in *tert*-butanol, 1-hexanol, 1-butanol and 2-propanol. The suspensions were treated with an ultrasonic probe with a pulse of 1 s on, 1 s off at a power of 150 W for 1 min. The BHF-DBSA alcohol suspensions were prepared at mass concentrations γ higher than 60 g/l and then diluted to 30 g/l, 15 g/l, 5 g/l, and 1 g/l [55].

Suspensions for phase behavior analysis

The suspensions were prepared from the DBSA-modified NPLs (see Chapter 3.2.2). A known amount of NPLs was dispersed in 1-butanol to prepare a suspension at $\phi \sim 3$ % [125]. The suspensions with $\phi \sim 3$ % were concentrated by centrifugation at 20817 RCF (Centrifuge 5430, Eppendorf) for 15 min in 2 ml centrifuge tubes. After centrifugation, the suspensions were pipetted out of the centrifugation tube in thirds (top, middle and bottom part), as shown in Figure 3.4. The centrifugation was repeated several times until we reached the threshold volume fraction for the phase transition from isotropic to nematic phase. The suspensions in the initial state (top, middle and bottom) differ by the volume fraction of NPLs and the average equivalent diameter of NPLs. The top part has the lowest ϕ and the smallest average diameter, while the bottom has the highest ϕ and the largest average diameter. The nematic suspensions (usually middle and bottom part) were diluted with DBSA solution (4 mM–5 mM) in a suitable alcohol to form the isotropic phase. The concentration of dissolved DBSA (c_{dis}) was determined by measuring the conductivity of the top part (see the procedure in Chapter 3.4.2). To reach the ϕ_{IN} (volume fraction of the isotropic-nematic phase transition), the isotropic and the original nematic suspensions of the same part were mixed in different ratios as shown in Figure 3.4 [125].

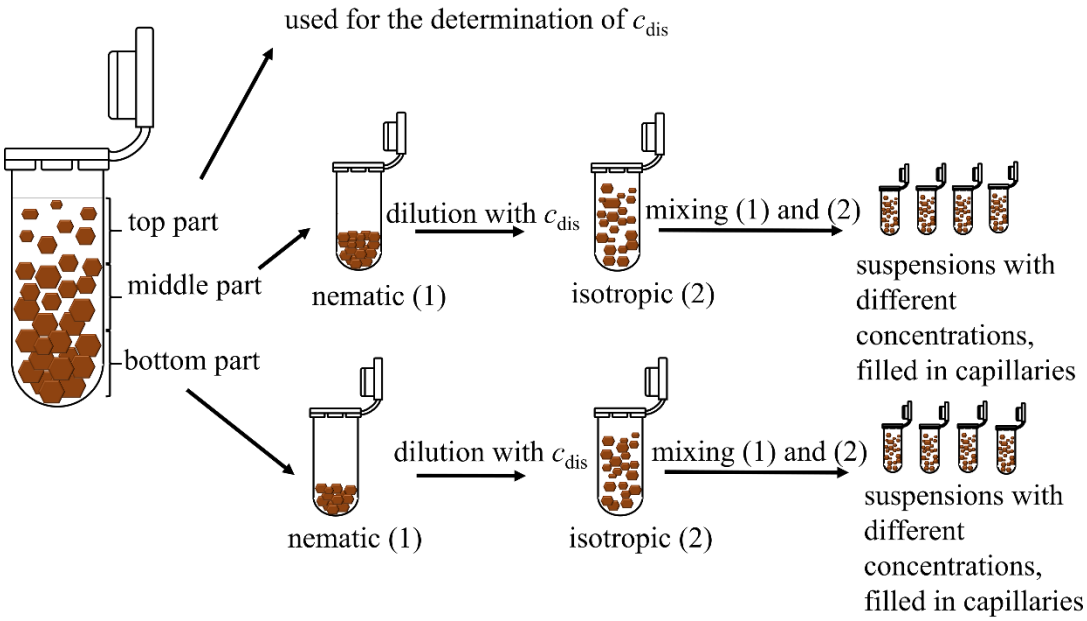

Figure 3.4: Schematic representation of centrifuged suspension and preparation of suspensions for phase behavior observation [125].

Suspensions in an LC host

The colloidal suspensions in an LC host were all prepared in the LC 5CB. 5CB was heated to 60 °C to undergo the transition to the isotropic phase. A suspension of the BHF NPLs in a volatile solvent was added to 5CB. The mixture was left at 60 °C until the volatile solvent evaporated, while the NPLs remained in pure 5CB. Colloidal stability was evaluated in the isotropic and nematic phases of 5CB. The suspensions were quenched from the isotropic to the nematic phase to avoid any aggregation during a slow phase transition. Quenching is performed by pipetting an isotropic 5CB suspension onto a cold surface of a glass vial, which allows rapid cooling to the nematic phase. The stability of the nematic suspensions was evaluated by centrifuging the quenched suspension for 3–5 min at 10000

RCF, sedimenting any aggregates formed during quenching. The short time of centrifugation ensures that the NLC suspensions do not heat up beyond the phase transition temperature.

3.3 Experimental Methods

Transmission electron microscopy (TEM)

TEM is an analytical method that allows an image to be formed based on the transmission of electron beam through the sample. The shape and equivalent diameter of the NPLs were estimated from the TEM images, as shown in Figure 3.5, taken with the Jeol JEM-2100 transmission electron microscope at 200 kV accelerating voltage. The microscope is equipped with an electron source and Gatan charge-coupled device (CCD) camera ORIUS. The sample for TEM was prepared by drop deposition of a dilute suspension of NPLs on a Cu grid-supported perforated transparent carbon foil (holey carbon coated mesh 3 mm). The equivalent diameter of NPLs lying flat on the supporting carbon foil was determined from TEM images using a DigitalMicrograph Gatan Inc. software, with at least 250 particles measured.

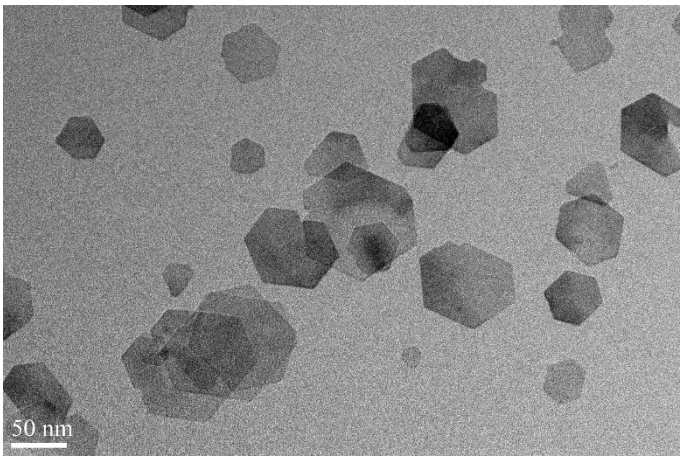

Figure 3.5: TEM image of BHF NPLs.

Magnetic measurements

The magnetic properties of the dried BHF NPLs were measured using a Lakeshore 7400 Series vibrating sample magnetometer (VSM). The dried and ground sample with a mass between 10 mg and 40 mg was placed in a plastic holder and tightly compressed. The plastic holder was placed in a uniform magnetic field in the range between 10 kOe and -10 kOe and vibrated sinusoidally. The result of the measurement was a magnetic hysteresis loop typical of hard magnetic materials [15].

Thermogravimetric analysis (TGA) and mass spectrometry (MS)

The mass fraction of DBSA in the sample was determined by TGA. The sample was heated in a chamber furnace (Bosio) to 700 °C at a heating rate of 3 °C/min (or to 500 °C at a heating rate of 0.5 °C/min) and remained at this temperature for 2 h. Both conditions allowed quantitative decomposition of DBSA. The difference in temperature and heat rate did not affect the final result [55], [125].

Thermal analyses (TA) of a ligand and dried surface-modified NPLs were carried out at the University of Nova Gorica simultaneously with thermogravimetry and differential scanning calorimetry (DSC) (TGA/DSC 2, Mettler Toledo) at University of Nova Gorica.

The thermal analyzer was coupled with a mass spectrometer (MS, Thermostar300, Vacuum Pfeifer). The samples were heated at a heating rate of 20 °C/min from 40 °C to 1100 °C in a static air atmosphere.

Infrared spectroscopy (IR)

The surface-modified NPLs were examined by IR spectroscopy to follow the changes on the surface of the NPLs after surface modification. The surface-modified dried NPLs and the pure ligands were analyzed by Fourier transform IR spectroscopy using a PerkinElmer Spectrum 400 FT-IR/FT-FIR spectrometer. Spectra were taken with a Universal attenuated total reflectance sampling accessory in the range 4000–650 cm^{-1}.

Small-angle X-ray scattering (SAXS)

SAXS measurements [55] were performed at the Faculty of Chemistry and Chemical Technology in Ljubljana using an in-lab-modified Kratky camera (Anton Paar KG, Graz, Austria) connected to a standard X-ray generator (GE Inspection Technologies, SEIFERT ISO-DEBYEFLEX 3003). The incident beam ($\lambda = 0.154$ nm) was generated with a Cu anode operated at 40 kV and 50 mA. The beam passed through the Göbel mirror and block collimation system to result in a line-collimated monochromatic primary beam. Standard quartz capillaries with an outer diameter of 1 mm and a wall thickness of 10 µm were filled with the BHF-DBSA suspensions (in *tert*-butanol, 1-hexanol, 1-butanol, and 2-propanol) at a concentration 1 g/l. The capillaries were thermostated at 25 °C using a Peltier element. The intensity of the scattered X-rays was detected using a Mythen 1K microstrip solid-state diode-array detector (Dectris, Baden, Switzerland) in the small-angle scattering vector regime between 0.065 nm^{-1} and 7 nm^{-1} [55].

Conductivity measurements

Conductivity measurements were performed using the Conductometer Knick-Portamess 913 to determine the c_{dis} in the alcohol suspensions to calculate the Debye screening length. Measurements were performed in alcohol suspensions of BHF-DBSA NPLs with different suspension concentrations (5 g/l, 15 g/l, and 30 g/l) at 27 °C in a GFL water bath and in water and alcohol solutions of DBSA. Conductivity was measured as a function of DBSA concentration in the suspensions/solutions after the addition of known amounts of a DBSA solution (of known concentration) in a suitable solvent [55], [125].

Electrophoretic mobility measurements

Electrophoretic mobility measurements were performed using an AntonPaar Litesizer 500 and a ZetaPALS instrument (Brookhaven Instruments Corporation). Phase analysis light scattering (PALS) is used to determine the electrophoretic mobility of charged suspended particles by analyzing the rate of phase shift between modulated reference beam and light scattered from the sample [126]. The phase change is plotted with time as depicted in Figure 3.6. The electrophoretic mobility measurements were used to determine the zeta potential in the suspensions using Henry's equation (Eq. (1.3) [48]). For aqueous suspensions, we used a disposable cuvette (on the ZetaPALS instrument) and Omega Cuvette Mat.No. 225288 (on the AntonPaar Litesizer instrument). For non-aqueous solvents, a Univette and a Univette Low Volume measuring cell were used. Measurements were performed in:

- 1 g/l suspensions of DBSA-modified NPLs in 1-hexanol, 1-butanol and 2-propanol at 25 °C and at 26 °C in *tert*-butanol with an applied voltage of 40 V. For the measurements with increasing DBSA concentration, an applied voltage of 30 V was used, and the measurements were performed at 27 °C in *tert*-butanol and at 25 °C in 1-butanol [55].

- Aqueous and alcohol suspensions of other surface-modified NPLs with automatically applied voltage at temperatures between 20 °C and 25 °C.
- Isotropic 5CB suspensions at 45 °C and 55 °C. The zeta potential measured in the isotropic 5CB was close to zero in most cases, because the phase plot was close to zero, as shown in Figure 3.6b. The reason why we do not get a good measurement despite the presence of charge-carrying functional groups could be a layer of 5CB around the dispersed NPLs. Another reason leading to this result is the presence of aggregates that may interfere with mobility under the applied electric field.

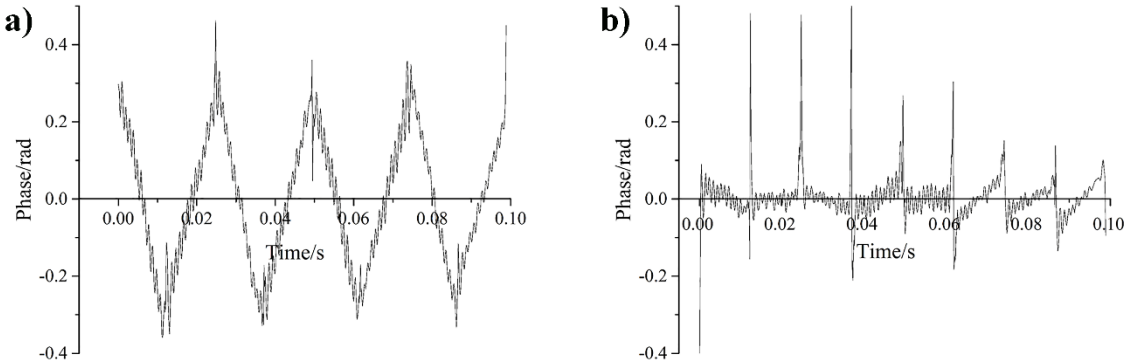

Figure 3.6: a) A good example of a measured phase plot for zeta potential measurement compared to b) a phase plot close to zero, indicating an unreliable result.

Dynamic light scattering (DLS)

DLS measurements were performed using an AntonPaar Litesizer 500 instrument on 1 g/l suspensions in 1-butanol and *tert*-butanol. Due to the relatively high melting temperature of *tert*-butanol, it is undercooled at ambient conditions. This affects its viscosity, which was required for the determination of the zeta-potential from electrophoretic mobility measurements (see Chapter 4.1.3). In DLS, the laser light is scattered by the particles in all directions. The suspended particles that undergo Brownian motion cause constant fluctuations in concentration and consequently fluctuations in the scattering intensity. In the experiment, the intensity autocorrelation function at a given scattering angle θ is calculated and the diffusion coefficient of the particles can be extracted from it [127]. For suspensions of monodisperse particles, the autocorrelation function is an exponentially decaying function. The BHF-DBSA suspensions in 1-butanol (at 25 °C) and in *tert*-butanol (from 20 °C to 28 °C) were side-scattered in a series of measurements [55].

Polarized optical microscopy (POM)

POM is used to examine materials with more than one refractive index, meaning that the optical properties of the materials are not the same in all directions. In addition to an ordinary optical microscope, POM incorporates two polarizers (polarizer and analyzer) into the system. The polarizer polarizes the light coming from the source that illuminates the sample, while the polarization of the transmitted light can be analyzed by rotating the analyzer.

In the studies of the phase behavior of the liquid magnet suspensions [125], the birefringence of the samples was measured using POM in combination with a custom-made system for magnetic field manipulation. The setup is represented in Figure 3.7. The camera was FLIR BFLY-U3-23S6M-C and the objectives were Nikon plan fluor 10x/0.30 or Mitutoyo plan apo NIR 50x/0.42. The Zerotesla system (see Figure 3.7) consisting of three pairs of

coils was used to eliminate the ambiental magnetic field, while the Oscitesla system (see Figure 3.7) consisting of one pair of coils was used to apply a well-defined magnetic field (up to 1.4 mT) to the sample. To eliminate the effect on the ordering of the NPLs from external sources (e.g. Earth magnetic field), a Zerotesla magnetic field manipulation system was used to compensate the unwanted fields to field strengths below 1 µT. The suspensions were filled in rectangular capillaries (0.05 mm × 1.00 mm, length 50 mm) and observed between the crossed polarizer and analyzer, with the long axis of the capillary oriented at an angle of 45° to the polarizer orientation [125].

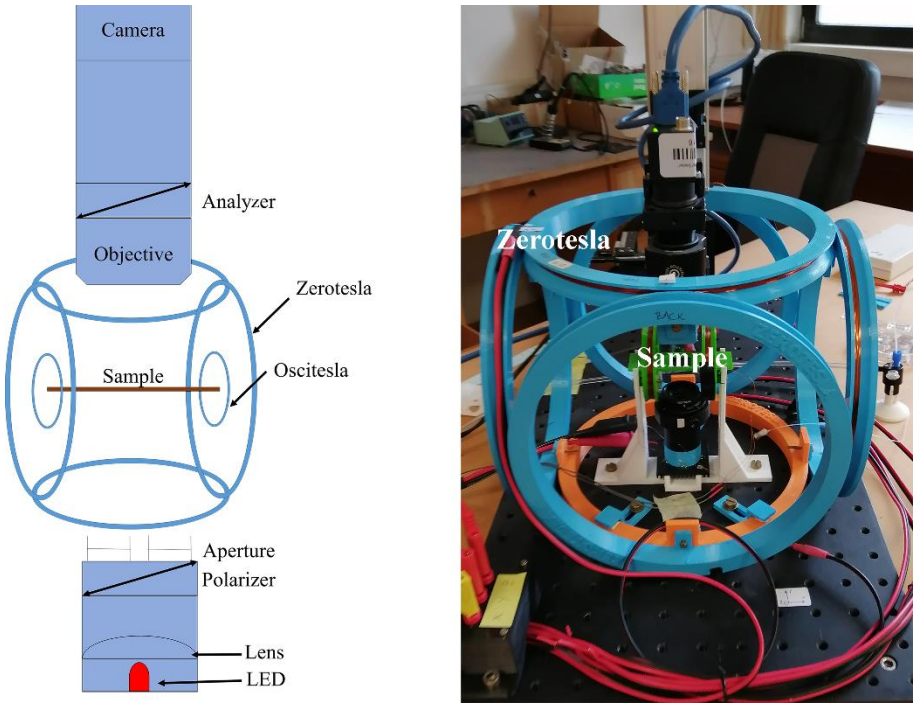

Figure 3.7: Schematic of the POM with a custom-made system for field manipulation on the left and an image of the setup on the right. The Zerotesla setup is blue and orange, while Oscitesla is green and positioned near the sample.

To observe the behavior in an LC host, the suspensions were prepared as described in Chapter 3.2.4. A drop of an isotropic 5CB suspension was observed with POM (Nikon) without polarizers to detect possible aggregates and between crossed polarizers for MO response. Suspensions were then quenched to the nematic phase and again observed (in one drop) between crossed polarizers to see MO response and possible aggregates. Stable nematic suspensions were additionally centrifuged (10000 RCF, 3–5 min) to remove aggregates. Suspensions that remained colloidally stable after the transition to the nematic phase were examined in a 20 µm LC cell without and under applied magnetic field $\mathbf{B}$ up to 20 mT) parallel and perpendicular to $\mathbf{n}$ using a custom-made electromagnet. Also slow phase transition with a slow decrease of temperature from isotropic to nematic phase was observed in a drop of suspension between crossed polarizers. Aggregation was expected. Aggregates formed during the transition were heated back to the isotropic phase to observe possible reversibility of aggregation.

3.4 Analysis of Results

3.4.1 Small-angle X-ray scattering

The length of the scattering vector q is defined as [128]:

$$q = \frac{4\pi}{\lambda}\sin\left(\frac{\theta}{2}\right) \tag{3.1}$$

where λ is the wavelength of illumination and θ is the scattering angle. The data obtained were corrected for capillary scattering and X-ray absorption and put to the absolute intensity scale, using water as the secondary standard [129]. The resulting data were still experimentally smeared due to the finite dimensions of the primary beam [130]. Therefore, the data were additionally desmeared with the iterative Lake algorithm [131]. The final data could then be compared to the calculated theoretical scattering intensities [55].

The SAXS intensities for model populations of NPLs were calculated assuming that the NPLs are disks of thickness h and radius R. The scattering amplitude $f(q)$ of a disk was calculated as follows [55]:

$$f(q) = \Delta\rho V_{\mathrm{i}} \frac{4\sin\left(hq_{\mathrm{P}}/2\right) J_1(x)(q_{\perp}R)}{hRq_{\perp}q_{\mathrm{P}}} \tag{3.2}$$

where $\Delta\rho$ is the contrast between the solvent and a disk, V_{i} is the volume of a disk, $J_1(x)$ is the Bessel function of the first kind, $q_{\perp}$ and q_{P} are the components of the length of the scattering vector q perpendicular and parallel to the disk axis. If we assume independent scattering from a single disk, the scattering intensity I is [55]:

$$I = \left\langle \left| f(q) \right|^2 \right\rangle \tag{3.3}$$

$\langle\ \rangle$ denoting the average over all orientation and diameters of the disks using the log-normal distribution function with the (measured) average equivalent diameter and standard deviation, as depicted in Figure 4.1a [55].

3.4.2 Conductivity measurements and Debye screening length

Based on the conductivity measurements, we were able to calculate the c_{dis} value and the molar concentration of the adsorbed DBSA c_{ads} using the standard addition method. The conductivity of the suspensions was measured after subsequent additions of DBSA, which increased the conductivity and gave a linear dependence on the molar concentration of added DBSA Δc_{dis} as shown in Figure 3.8a. The concentration of c_{dis} in the initial alcohol suspension was calculated as the quotient of a and b, i.e., the intercept and the slope of the linear fit, respectively [132]:

$$\sigma_{\mathrm{s}} = a + \left(b \cdot \left(\Delta c_{\mathrm{dis}}\right)\right) \tag{3.4}$$

where σ_{s} is the conductivity of the alcohol suspension. The difference between the total amount of DBSA (c_{tot}) and c_{dis} is the c_{ads}. The conductivity measurements also allowed us to estimate the dissociation degree of DBSA in the suspensions. We measured conductivity

in water after the subsequent additions of DBSA, as depicted in Figure 3.8b, and compared it to conductivity of the suspensions with additions of DBSA (see Figure 3.8a). The dissociation degree in alcohols was calculated under the following assumptions: (1) that DBSA is totally dissociated in water and (2) that Walden's rule is valid [133]:

$$\Lambda^{\infty}\eta \approx \text{constant} \tag{3.5}$$

where Λ^{∞} is the molar conductivity at infinite dilution. The molar conductivity is defined as [133]:

$$\Lambda = \frac{\sigma_e}{c_i} \tag{3.6}$$

where σ_e is the conductivity of an electrolyte and c_i is its molar concentration. This gives the following expression for the calculation of the ion concentration in alcohols $c_{i,alcohol}$ [55]:

$$c_{i,alcohol} = \frac{c_{i,H_2O}}{\sigma_{H_2O}} \cdot \frac{\eta_{alcohol}}{\eta_{H_2O}} \cdot \sigma_{alcohol} \tag{3.7}$$

where $c_{i,H2O}$ is the number density of ions in water, σ_{H_2O} the conductivity in water, $\sigma_{alcohol}$ the conductivity in a given alcohol, η_{H_2O} and $\eta_{alcohol}$ are the viscosity of water and a given alcohol, respectively. Eq. (3.7) was used for the subsequent calculation of the Debye screening length κ^{-1} (see Eq (1.4) [46]). For the evaluation of electrostatic interactions (see Chapter 4.1) experimental results were used only for the suspensions of concentrations 5 g/l, 15 g/l, and 30 g/l. For the suspension with a concentration of 200 g/l, we assumed that the value of c_{dis} is 5 mM, since almost complete saturation occurs at 30 g/l, where c_{dis}/c_{tot} is ~ 7 % (see Table 4.1 in Chapter 4.1.1) and the mass fraction of DBSA in the dry part was experimentally determined to be 13.6 % [55]. In the phase behavior studies (see Chapter 4.2) of the alcohol suspensions, c_{dis} was determined from conductivity measurements in the top part of the centrifuged suspensions (see Chapter 3.2.4) [125].

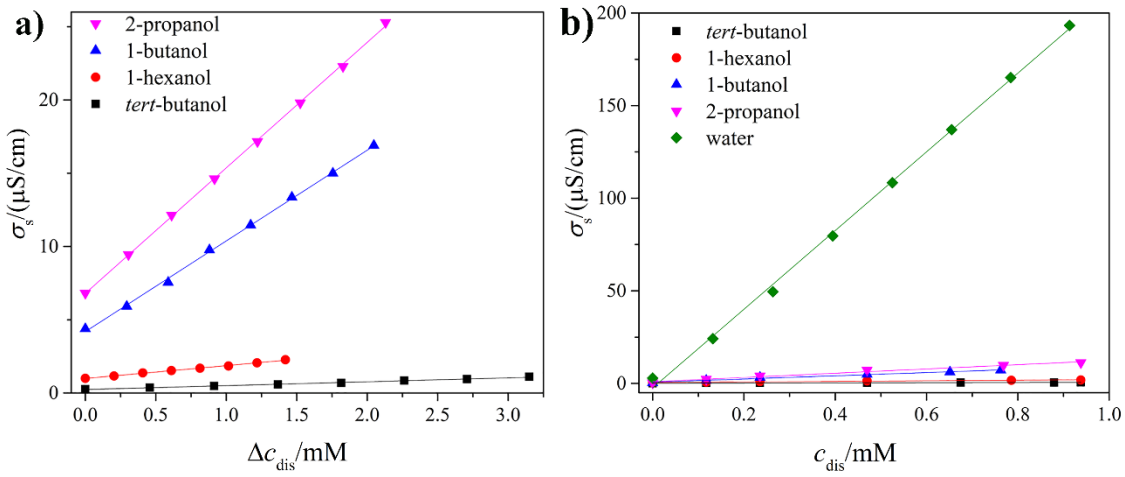

Figure 3.8: Conductivity dependence on Δc_{dis} and c_{dis}. a) for the 30 g/l alcohol suspensions of NPLs and b) for the water and alcohol solutions of DBSA.

3.4.3 Dynamic light scattering measurements

We obtained intensity autocorrelation functions of DLS measurements from a series of measurements for the BHF-DBSA *tert*-butanol suspensions in the range (20–28) °C and the 1-butanol suspension at 25 °C. The DLS measurements provide the characteristic decay rate (f_1) of the correlation function. The decay rate f_1 is proportional to the diffusion coefficient D_c [127]:

$$f_1 = D_c q_s^2 \tag{3.8}$$

where q_s is the length of the scattering vector q multiplied by the refractive index of the solvent. The diffusion coefficient for a spherical particle is inversely proportional to η and is defined as [127], [133]:

$$D_c = \frac{k_B T}{6\pi\eta R_s} \tag{3.9}$$

where R_s is the radius of the spherical particle. D_c deviates slightly for platelets, but is still proportional to η^{-1} [127], [134]. All correlation functions fall into a master curve when time is rescaled by f_1, as shown in Figure 3.9. This confirms that the viscosity of *tert*-butanol $\eta_{tert\text{-butanol}}$ can be calculated from [55], [127]:

$$\frac{f_{1\text{–butanol}(25°C)}}{f_{tert\text{–butanol}}} = \frac{\eta_{tert\text{–butanol}}}{\eta_{1\text{–butanol}(25°C)}} \tag{3.10}$$

where to determine f_1, background y_0 and amplitude A_{Amp}, the correlation functions were fitted using [55]:

$$g_2 = A_{Amp} \cdot e^{-2(f_1 \cdot \tau)^{s_1}} + y_0 \tag{3.11}$$

where τ is the delay time. The stretched exponent s_1, which accounts for polydispersity, was identical for all measurements, $s_1 = 0.88$. Eq. (3.10) gives the values of $\eta_{tert\text{-butanol}}$, listed in Table 3.1 [55].

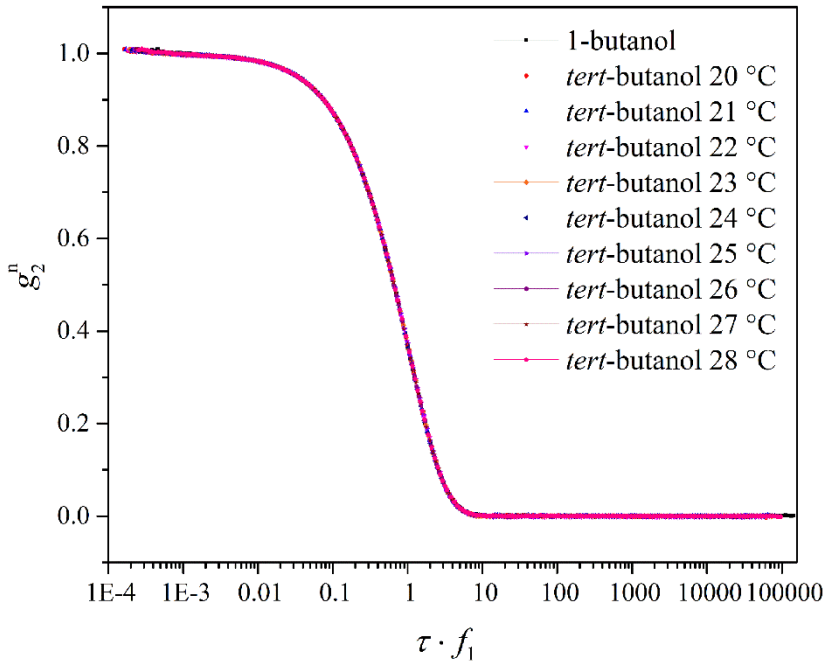

Figure 3.9: Identical curves of normalized correlation functions $g_2^{\mathrm{n}} = (g_2 - y_0)/A_{\mathrm{Amp}}$ vs $\tau \cdot f_1$ confirm that the viscosity of *tert*-butanol can be calculated from Eq. (3.10) [55].

Table 3.1: Calculated viscosity of *tert*-butanol at different temperatures [55].

T/ °C	20	21	22	23	24	25	26	27	28
η /(mPa s)	5.9	5.6	5.3	5.0	4.7	4.4	4.2	4.0	3.8

3.4.4 Calculations of interplatelets interactions

In the case of BHF NPLs, short-range VdW interactions can be neglected because the long-range electrostatic U_{el} and the magnetic dipole-dipole interactions U_{dip} prevail at distances relevant in this case. The total interaction energy U is therefore [55]:

$$U = U_{\mathrm{dip}} + U_{\mathrm{el}} \tag{3.12}$$

where the contributions of the magnetic dipole-dipole and electrostatic interactions depend on the distance between the NPLs and their orientation. An example of the average interaction energy is given in Figure 3.10. Figure 1.12 shows two thin disks describing magnetic NPLs with magnetic moment p_{i} perpendicular to the plate's plane. The unit vector $\mathbf{n}_{\mathrm{i}}$ denotes the orientation of p_{i}, $\mathbf{r}$ is a vector connecting the two plates and r its absolute value. Magnetic dipolar interaction between two NPLs also depends on the relative orientations of the NPLs. The relative orientations of the NPLs are described with the expression in the parentheses in Eq. (1.5), which has values between -2 and 2. In the case where the second dipole is parallel to the first dipole, $\mathbf{n}_2 \parallel \mathbf{n}_1$, and located on the symmetry axis of the first dipole $\mathbf{r} \parallel \mathbf{n}_2$, as depicted in Figure 3.11, Eq. (1.5) simplifies to Eq. (1.7). This is the case when the magnetic interaction between two NPLs is the strongest and the orientation of the NPLs, i.e., the disks in the calculation, resembles the situation in a ferromagnetic nematic suspension.

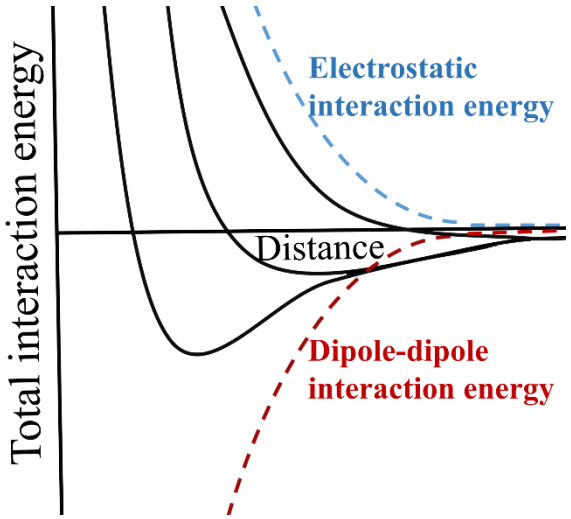

Figure 3.10: An example of the total interaction energy (Eq. (3.12)) shown with black lines as a function of the distance between two NPLs.

Between two charged disks with charges $Z_1 e_0$ and $Z_2 e_0$ there is a repulsive electrostatic interaction which can be described by [135]:

$$U_{\mathrm{el}} = \frac{Z_1 Z_2 e_0^2}{4\pi\varepsilon\varepsilon_0} f(\kappa R_1, \kappa R_2, \mathbf{n}_1, \mathbf{n}_2) \frac{e^{-\kappa r}}{r} \tag{3.13}$$

where R_1 and R_2 are the radii of the two thin plates, the anisotropy function f describes the contribution of the anisotropic shape and can be approximated as follows [135]:

$$f \approx 4 \frac{I_1(\kappa R_1 \sin\vartheta_1)}{\kappa R_1 \sin\vartheta_1} \frac{I_1(\kappa R_2 \sin\vartheta_2)}{\kappa R_2 \sin\vartheta_2} \tag{3.14}$$

ϑ_{i} is the angle between $\mathbf{r}$ and $\mathbf{n}_{\mathrm{i}}$ and $I_1(x)$ is a modified Bessel function of order 1. The possible values of κR_{i} in the BHF-DBSA suspensions range from 0.3 to 2.8, giving the possible values of f between 1 and 6. The anisotropy function is 1 in the case when the second dipole is parallel to the first, $\mathbf{n}_2 \parallel \mathbf{n}_1$, and located on the symmetry axis of the first dipole $\mathbf{r} \parallel \mathbf{n}_2$ (see Figure 3.11) and Eq. (3.13) is simplified for $U_{\mathrm{el,par}}$ to [125], [135]:

$$U_{\mathrm{el,par}} = \frac{Z_1 Z_2 e_0^2}{4\pi\varepsilon\varepsilon_0 r} e^{-\kappa r} \tag{3.15}$$

Therefore, the total interaction energy $U_{\mathrm{tot,par}}$ between two parallel NPLs located on the symmetry axis as depicted in Figure 3.11 can be simplified to [125]:

$$U_{\mathrm{tot,par}} = -\frac{\mu_0 p_1 p_2}{2\pi r^3} + \frac{Z_1 Z_2 e_0^2}{4\pi\varepsilon\varepsilon_0 r} e^{-\kappa r} \tag{3.16}$$

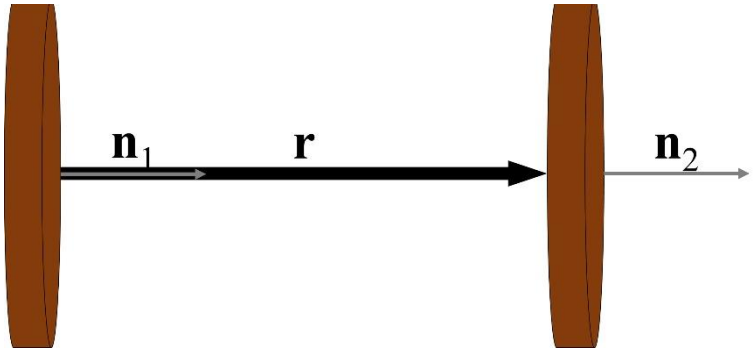

Figure 3.11: Schematic representation of two parallel platelets located on the symmetry axis, where **r** is the vector connecting the centers of the platelets and $\mathbf{n}_i$ vector is denoting their orientation [125].

The measured zeta potential values were used to estimate an average effective surface charge of the NPLs, which was calculated as follows [136]:

$$Ze_0 = 4\pi\varepsilon\varepsilon_0\kappa R_{eq}^2 k_B T / e_0 \times (2\sinh(e_0\psi_s / (2k_B T)) + 4/(\kappa R_{eq})\tanh(e_0\psi_s / (4k_B T)) \quad (3.17)$$

assuming that the charge of a disk is similar to the charge of a sphere with the same volume and radius R_{eq} and that the surface potential $\psi_s \approx \zeta$ [137]. R_{eq} stands for the sum of radius of the platelet and the DBSA layer. Averaging the total interaction U (Eq. (3.12)), over NPL orientation assuming the Boltzmann probability distribution $p(\mathbf{n}_1,\mathbf{n}_2,\mathbf{r})$ [55]:

$$p(\mathbf{n}_1,\mathbf{n}_2,\mathbf{r}) = \frac{1}{A}\mathrm{e}^{-U/k_B T} \quad (3.18)$$

gives the average interaction $\langle U(r)\rangle$ at a given position **r**. A is the normalization constant [55]:

$$A = \int e^{\frac{U}{k_B T}} d\Omega_1 d\Omega_2 \quad (3.19)$$

the integration is performed over all solid angles Ω_i [55].

3.4.5 Polarized optical microscopy

3.4.5.1 Phase behavior in an isotropic solvent

To distinguish between the isotropic and nematic phases of a suspension, a suspension was placed in a rectangular capillary and observed by custom-built POM. Between crossed polarizers, an isotropic suspension looks dark (black) and a nematic suspension is bright with areas of different brightness that are magnetic domains. The difference in brightness is depicted in Figure 3.12.

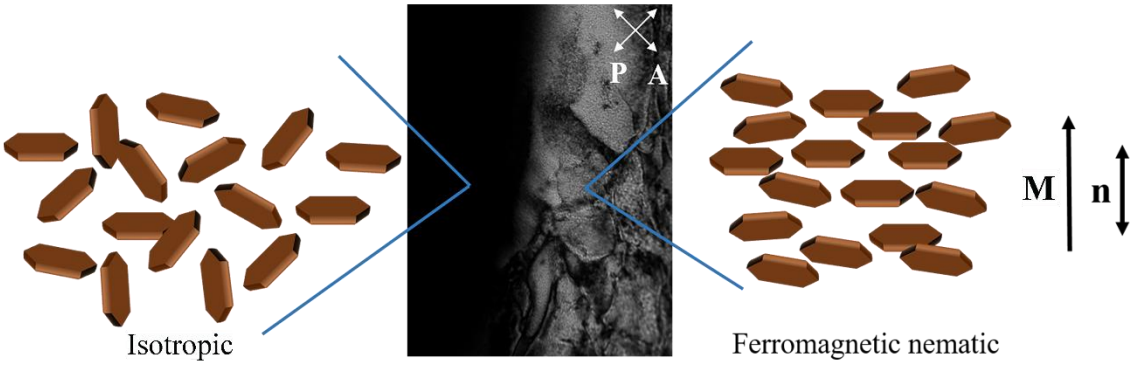

Figure 3.12: Schematic representation of NPL orientation in the isotropic black part (left) and in the greyish nematic part of a BHF NPL suspension, where magnetic domains can also be observed.

Birefringence measurements were used to determine the ϕ_{IN} and were performed by POM with the magnetic field applied along the long axis of the capillary, i.e., in the direction of 45 ° to the direction of the polarizer. From the transmission image, the light yield was extracted as the average pixel-intensity value in the region of interest that was 256 px × 256 px (77 µm × 77 µm) divided by the exposure time. This allowed us to compare images with different exposure times and effectively have a higher dynamic range. To calculate the birefringence, we first obtained the normalized intensity j/j_0 by scaling the light yield between 0 and 1 with a shift toward 0 for the minimal value and dividing by the maximum value to be scaled to 1. The birefringence Δn was calculated from [125]:

$$\frac{j}{j_0} = \sin^2\left(\frac{k d_c \Delta n}{2}\right) \tag{3.20}$$

where k is the wavenumber equal to $2\pi/\lambda$ and d_c is the thickness of the capillary [125].

3.4.5.2 Behavior in an LC host

The MO response in ferromagnetic NLCs differs from the MO response of a pure LC by its sensitivity to the sign of the magnetic field. No change in the **n** orientation is observed when a magnetic field is applied to a monodomain sample along the magnetization. Therefore, most magnetic moments are oriented along the direction of the applied magnetic field. When the magnetic field is applied in the opposite direction, the response is observed above a threshold value of the field. At this point, the magnetization starts to reorient until it reaches the saturation value again, which means that all magnetic moments are reoriented in the opposite direction. The reorientation can be observed with POM. During the reorientation, the POM image changes from dark to bright, as shown in Figure 3.13 and Figure 3.14, due to the twist of **n** and the magnetic moments at the center of the LC cell. The direction of **n** at the boundaries is fixed due to the anchoring of the LC director to the cell surface. At elevated field (10 mT), some white lines known as surface π-domain walls may appear. In these lines, the orientation of **n** at the surface is turned by π. The π-domain walls separate the twisted and undeformed part of the sample and can travel through the sample. By moving across the sample, the π-domain walls leave behind an undeformed area [94]. Figure 3.14a and Figure 3.14b represent the alignment of the magnetic NPLs in the zero field and Figure 3.14c and Figure 3.14d under the applied magnetic field in two directions. Black lines represent the **n**. In Figure 3.14b, the sample

between crossed polarizers appears black due to the orientation of the NPLs. When a uniform field is applied (see Figure 3.14c, Figure 3.14d), only the NPLs with the opposite magnetization direction realign, while no realignment occurs in the regions with the same magnetization direction as the external magnetic field direction. The angle of rotation is determined by the competition between elastic and magnetic torques [138].

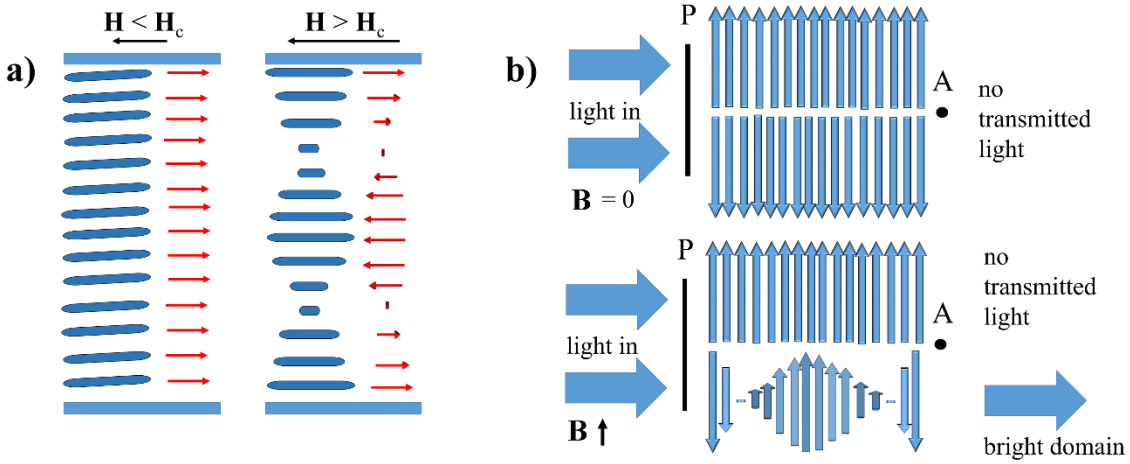

Figure 3.13: a) The blue ellipsoids represent the **n** orientation and the red arrows represent the magnetization orientation. With an applied magnetic field in the opposite direction to the magnetization, above a critical value, **n** and the magnetization reorient. b) Schematic representation of the MO effect. Above is an example of magnetic domains with opposite magnetization direction but the same **n** in the zero field. No light is transmitted through the sample between crossed polarizers. In the bottom part of the image, a magnetic field is applied along **n** and the domain with the magnetization direction opposite to the applied magnetic field reorients. This results in a bright POM image of such domains. The surface π-domain walls are white lines that appear between the domains. In these domains, **n** is turned by π [94].

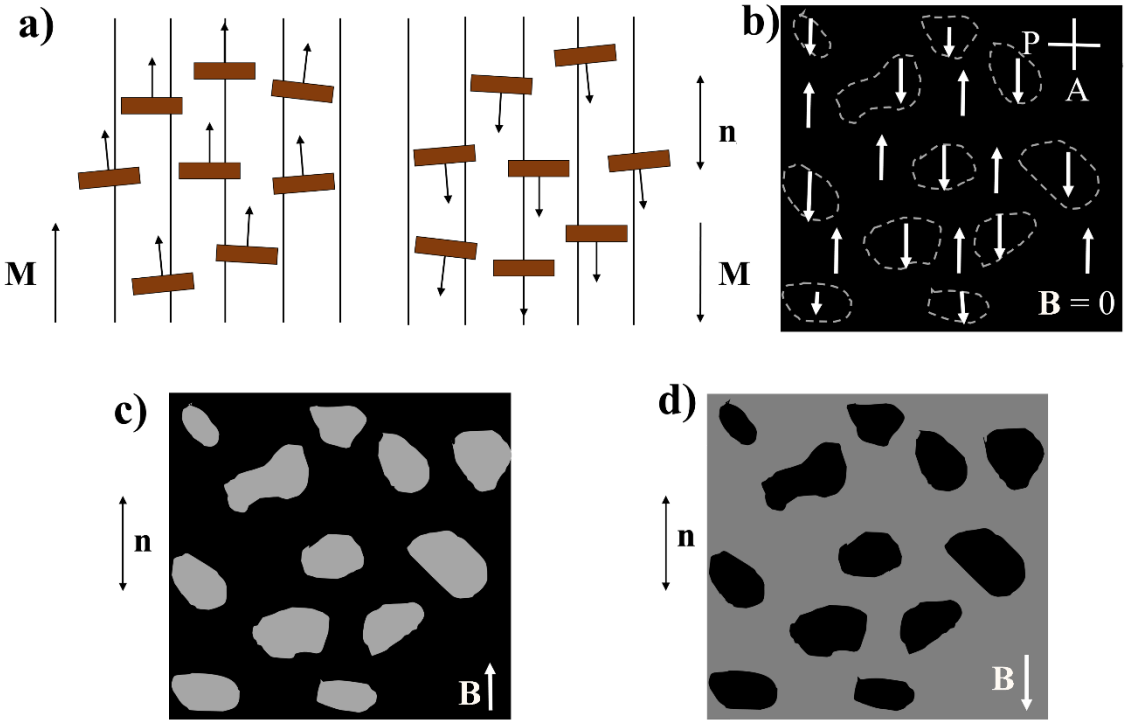

Figure 3.14: Schematic representation of the MO response in a ferromagnetic NLC. a) A ferromagnetic NLC in zero field, where the magnetization in the magnetic domains is along **n**. b) Corresponding schematic representation of a POM image for a), where the polarizer and analyzer are at 90°. The analyzer is located along **n** and the domain walls are drawn (not seen in the actual POM image in zero field). c) Domains after applied magnetic field that causes realignment of only those domains that are antiparallel to the direction of the applied magnetic field. d) When the direction of the applied magnetic field is reversed, the alignment is also reversed. The brightness of the domains is reversed compared to c) [94], [138].

Chapter 4

Results and Discussion

DBSA colloidally stabilizes BHF NPL suspensions in various alcohols and thus fulfills the conditions for liquid magnet formation (see Chapter 1.4.2.1). However, DBSA is also the reason that alcohol suspensions are a very complicated system in terms of interparticle interactions. To evaluate the interparticle interactions, we need to consider electrostatic and magnetic interactions. In the first part of Chapter 4, we present the study of the electrostatic interactions between the BHF NPLs in selected alcohols. The obtained results are crucial for a better understanding of the interactions in the liquid magnet and for its fabrication, since the interplatelets interactions are important for the ferromagnetic nematic ordering. In the second part of Chapter 4, we focus on the evaluation of the phase behavior of the 1-butanol suspensions of BHF NPLs. In the last part of Chapter 4, we discuss other surface modifications for BHF NPLs to prepare stable colloidal suspensions and ferromagnetic liquids.

4.1 Electrostatic Interactions in the Suspensions of BHF NPLs in Alcohols

The results in this chapter (as well as the parts in Chapter 3 used to obtain them) have been published and are reproduced with permission [Patricija Hribar Boštjančič, Matija Tomšič, Andrej Jamnik, Darja Lisjak, and Alenka Mertelj
The Journal of Physical Chemistry C 2019 123 (37), 23272-23279
DOI: 10.1021/acs.jpcc.9b07455] [55]. Copyright [2019] American Chemical Society. https://pubs.acs.org/doi/10.1021/acs.jpcc.9b07455.

The hydrothermally synthesized BHF NPLs (with procedures described in Chapters 3.2.1 and 3.2.2) used to determine the electrostatic interactions in alcohol suspensions had an average equivalent diameter of 55 nm with a statistically determined standard deviation of 20 nm. The equivalent diameter distribution of the NPLs is depicted in Figure 4.1a. The magnetic hysteresis, shown in Figure 4.1b, expresses the typical hard-magnetic behavior with the M_s of the bare NPLs being 39 A m^2/kg. The mass fraction of DBSA W_{DBSA} in the dry part was determined to be 13.6 % using [55]:

$$W_{DBSA} = \frac{m_{DBSA}}{m_{DBSA} + m_{NPLs}} \tag{4.1}$$

where m_{DBSA} and m_{NPLs} are the mass of DBSA and the mass of bare NPLs, respectively.

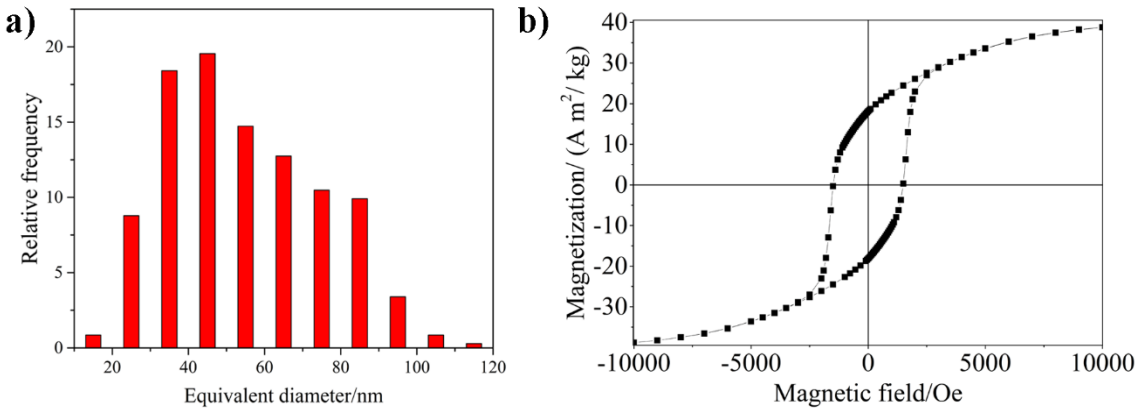

Figure 4.1: a) Equivalent diameter distribution and b) magnetic hysteresis of the BHF NPLs used to determine the electrostatic interaction in alcohol suspensions [55].

The DBSA-modified BHF NPLs formed stable colloidal suspensions in *tert*-butanol, 1-hexanol, 1-butanol, and 2-propanol, which was confirmed by SAXS measurements. The SAXS results, presented as desmeared SAXS curves on an absolute scale, are presented in Figure 4.2a and prove that there are no significant differences between the NPLs in suspensions in all four alcohols. The thicknesses of the NPLs, previously determined [44] based on crystal structure of the BHF NPLs, vary with the number of R blocks from 3.0 nm to 4.1 nm and 5.3 nm [44]. The expected scattering intensity was calculated for disks with a defined thickness and log-normal distribution of diameters (see Figure 4.1a) and the measured SAXS intensities were fitted by a sum of the calculated intensities corresponding to the NPL thicknesses of 3.3 nm, 4.4 nm, 5.6 nm, and 6.6 nm. The thickness value of 6.6 nm was not determined from the crystal structure [44], but we added it to account for aggregate formation. The parameters of the fit were the amplitudes of the calculated intensities presented in Figure 4.2b. The amplitudes allowed us to estimate volume fractions of 76 % (1 ± 0.09) of 3.3 nm, 22 % (1 ± 0.1) 4.4 nm, 2 % (1 ± 0.7) 5.6 nm, and 0.008 % (1 ± 1.5) 6.6 nm NPL thickness [55].

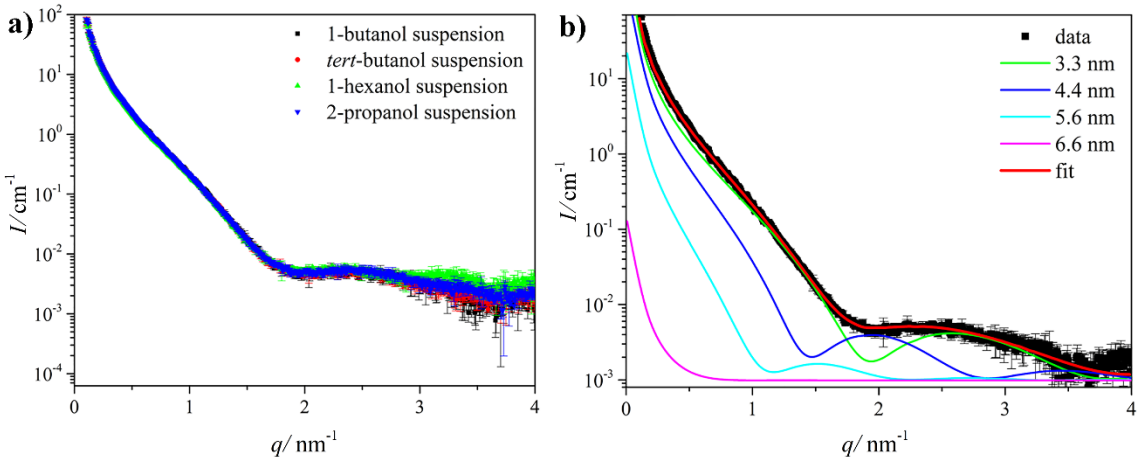

Figure 4.2: a) Desmeared experimental SAXS curves of the NPL suspensions, which were desmeared by the iterative Lake algorithm [131], b) the black squares represent desmeared experimental SAXS curve on an absolute scale and the red line is fit. The fit is the weighted sum of the contributions from the NPLs of various thicknesses marked in the graph [55].

Surface modification of the NPLs with DBSA is carried out in water at acidic pH (1.5), ensuring the positive charge on the NPLs surface and dissociation of DBSA. The electrostatic interaction between the NPLs and DBSA leads to the formation of a hydrophobic layer on the surface of the NPLs, as shown in Figure 4.3a. The DBSA molecules bind to the NPLs with the sulfonic group, while the hydrophobic tail faces the surrounding solvent and coils (see Figure 4.3a). The hydrophobic NPLs are not stable in water and flocculate. During the washing step in acetone and drying the NPLs (see procedure in 3.2.2), we remove (most of) the water (and acetone) residues that would affect colloidal stability in other solvents. The dried NPLs with the adsorbed DBSA are neutral (see Figure 4.3b). When these NPLs are dispersed in different alcohols, the DBSA is partially dissociated and the NPL's surface is partially protonated. The dissociated DBSA molecules are electrostatically attracted to the positively charged surface sites on the NPLs (see Figure 4.3c), similar to the water system (see Figure 4.3a). The nondissociated, i.e., neutral DBSA molecules dissolve in the alcohol and form a double layer due to the hydrophobic interactions between the nonpolar alkyl tails of the bound and unbound DBSA, as shown in Figure 4.3c and Figure 4.4 [62]. The rest of the unbound surface sites are positively charged, most likely due to ionic impurities in the system (either water or HNO_3 from the synthesis). The DBSA double layer is in dynamic equilibrium with the system and changes, for example, with the concentration of the suspension [55]. The dynamic equilibrium between adsorbed and dissolved DBSA depends on the conditions in the suspension, i.e., the concentration of the suspension and the type of solvent.

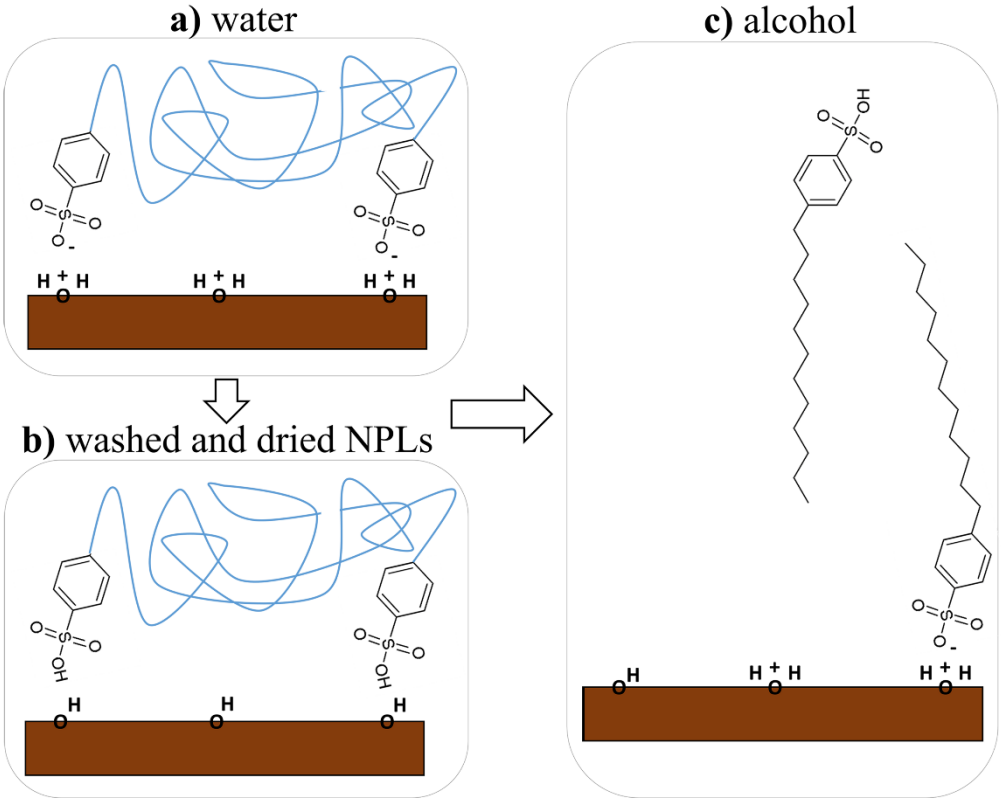

Figure 4.3: Schematic representation of the proposed mechanism of charge formation of the BHF NPL-DBSA-solvent system, showing a) the system in water with collapsed alkyl chains (blue), b) the dried BHF-DBSA NPLs, and c) the system in alcohol.

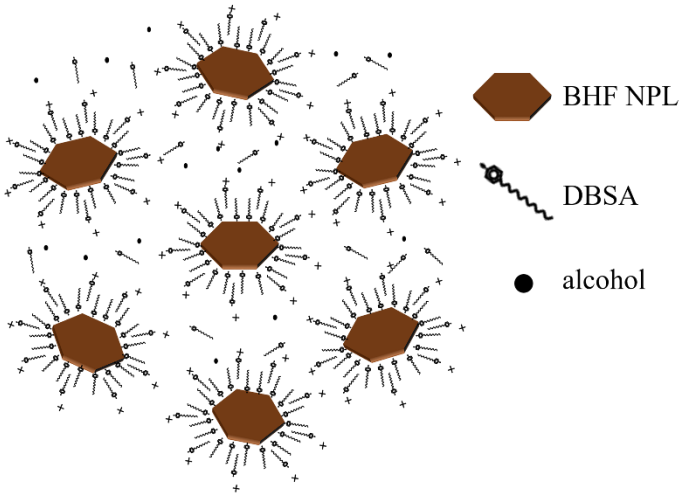

Figure 4.4: A schematic representation of DBSA-modified NPLs alcohol suspension [55].

We prepared suspensions with concentrations of 5 g/l, 15 g/l, and 30 g/l in *tert*-butanol, 1-hexanol, 1-butanol, and 2-propanol to investigate the effects of the alcohol's polarity and the suspension concentration on the surfactant behavior and electrostatic interactions in the suspensions.

4.1.1 Surfactant behavior in the alcohol suspensions

The behavior of the surfactant in the alcohol suspensions affects the colloidal stability. As mentioned before, the formation of the DBSA double-layer is triggered by dispersing the BHF DBSA-modified NPLs in alcohol. Part of the DBSA molecules remains dissolved in the surrounding alcohol. A part of this dissolved DBSA is also dissociated, which significantly affects the ionic strength in the suspensions. The c_{ads} and c_{dis} represent the molar concentrations of adsorbed and dissolved DBSA (the latter should not be confused with dissociated DBSA) and were obtained from the conductivity measurements (see Chapter 3.4.2) in *tert*-butanol, 1-hexanol, 1-butanol, and 2-propanol suspensions [55]. The results are shown in Table 4.1. The polarity of the alcohols affects the value of c_{dis}, which is lower in more polar 2-propanol and 1-butanol suspensions than in less polar 1-hexanol and *tert*-butanol suspensions. The concentration of the suspension also affects the c_{dis} value. With the dilution from 30 g/l to 15 g/l and 5 g/l, the adsorbed DBSA is additionally dissolved from the surface of the NPLs in all four studied alcohol suspensions. The quotient between the molar concentration of c_{ads} and c_{tot} in the sample (c_{ads}/c_{tot}) enables a proper evaluation of the adsorbed fraction of DBSA on the surface of the NPLs. The comparison of c_{ads}/c_{tot} values showed that the suspensions with a concentration of 30 g/l were similar in the samples studied. Decreasing the suspension concentration from 30 g/l to 15 g/l and further to 5 g/l causes a change in the c_{ads}/c_{tot} value due to the additional dissolution of DBSA. The degree of this additional dissolution depends on the polarity of the alcohol. The dissolution from the surface of the NPLs is stronger in less polar *tert*-butanol and 1-hexanol than in more polar 1-butanol and 2-propanol. This indicates that the increased polarity of the alcohols decreases the dissolution of DBSA from the surface of the NPLs [55].

Table 4.1: Molar concentrations of adsorbed c_{ads}, dissolved c_{dis} and c_{ads}/c_{tot} of DBSA in the studied alcohols at different suspension concentrations γ [55].

Alcohol	ε	γ /(g/l)	c_{dis}/mM	c_{ads}/mM	c_{ads}/c_{tot}
tert-butanol	12.1 [139]	5	0.71	1.38	0.66
		15	0.92	5.33	0.85
		30	0.93	11.57	0.93
1-hexanol	13.1 [140]	5	0.31	1.77	0.85
		15	0.59	5.66	0.91
		30	0.90	11.60	0.93
1-butanol	17.3 [139]	5	0.27	1.81	0.87
		15	0.49	5.76	0.92
		30	0.68	11.81	0.95
2-propanol	18.9 [141]	5	0.25	1.84	0.88
		15	0.50	5.75	0.92
		30	0.79	11.71	0.94

4.1.2 Debye screening length

The conductivity measurements enabled the determination of the dissociation degree of the DBSA in the studied alcohols. The determined dissociation degree increases with the polarity of the alcohol and is presented in Table 4.2.

Table 4.2: Dissociation degree in the studied alcohols [55].

	tert-butanol	1-hexanol	1-butanol	2-propanol
Dissociation degree/ %	0.6	2.1	8.6	9.0

The concentration of dissociated DBSA in the suspensions contributes to the ionic strength and consequently significantly influences the Debye screening length κ^{-1}. The values of κ^{-1} are presented in Table 4.3 and were calculated using Eq. (1.4). As expected from the differences in the nature of different alcohol suspensions, the value of κ^{-1} changes not only with the choice of alcohol but also with the concentration of the suspension. The suspensions in less polar *tert*-butanol and 1-hexanol have larger κ^{-1} values than the suspensions in 1-butanol and 2-propanol (see Table 4.3). At first instance, this may seem surprising, since the values of κ^{-1} increase with decreasing dielectric constant of a solvent, although they are proportional to $\sqrt{\varepsilon}$. But the lower dissociation degree of DBSA in less polar alcohols lowers the ionic strength of the suspension. The low ion concentration of dissociated DBSA molecules leads to weak shielding of the charge of the NPLs, resulting in stronger electrostatic repulsive forces between NPLs and thus a larger κ^{-1}. Decreasing suspension concentration, and thus c_{dis}, causes an increase in the κ^{-1} in the suspensions in all four alcohols [55].

Table 4.3: κ^{-1} in the alcohol suspensions at different suspension concentrations γ [55].

	γ /(g/l)	*tert*-butanol	1-hexanol	1-butanol	2-propanol
κ^{-1} /nm	5	78	70	44	41
	15	78	49	32	30
	30	70	41	26	25
	200	29	16	9	9

4.1.3 Zeta potential of the DBSA-modified NPLs alcohol suspensions

The zeta potential values for the DBSA-modified NPLs in *tert*-butanol, 1-hexanol, 1-butanol and 2-propanol were obtained from the electrophoretic mobility measurements (see Chapter 3.3) using Eq. (1.3). The results are listed in Table 4.4 [55].

Table 4.4: The values of electrophoretic mobility μ and zeta potential ζ for the DBSA-modified NPLs suspended in the studied alcohols [55].

Alcohol	ε	η /(mPa s)	$T_{\text{measurement}}$ /° C	μ /(µm cm/(V s))	ζ /mV
tert-butanol	12.3 [139]	4.2	26	0.159 ± 0.005	92 ± 3
1-hexanol	13.3 [140]	4.6 [142]	25	0.135 ± 0.006	79 ± 4
1-butanol	17.6 [139]	2.6 [143]	25	0.303 ± 0.009	75 ± 2
2-propanol	19.3 [141]	2.0 [144]	25	0.406 ± 0.007	70 ± 1

The zeta potential values calculated from the measured electrophoretic mobility decrease with an increase in the dielectric constant of the alcohol (see Table 4.4). Similar results were obtained by Ovtar et al. [62], who observed a clear link between the dielectric constant (i.e., polarity of the solvent) and the zeta potential values. Nevertheless, the zeta-potential values for the NPLs in *tert*-butanol suspension were higher than expected with respect to the dielectric constant. The DBSA concentration in the suspension affects the ionic strength and may affect the colloidal stability of the suspension. Therefore, to eliminate the influence of small experimental variations in DBSA concentration ($\Delta\, c_{\text{tot}}$), the zeta potential was determined after known amounts of DBSA were subsequently added to the suspension in 1-butanol and in *tert*-butanol to change c_{tot} (see Table 4.5). The zeta-potential values remain constant after small changes of c_{tot} in 1-butanol. However, the *tert*-butanol suspension differs from the 1-butanol suspension after the first addition, i.e., when $\Delta\, c_{\text{tot}} = 0.56$ mM (Table 4.5). The zeta-potential value decreases after the first increase in DBSA, but then remains constant after all subsequent DBSA additions (see Table 4.5). This behavior in the *tert*-butanol suspension can most likely be attributed to the lower dissociation degree (see Chapter 4.1.2) and the better solubility (Table 4.1) of DBSA in *tert*-butanol than in 1-butanol. Minor changes in c_{tot} do not significantly affect the zeta-potential values. However, larger additions of DBSA do affect colloidal stability. At $\Delta\, c_{\text{tot}}$ higher than 120 mM, the suspension started to sediment and lost its colloidal stability [55].

Table 4.5: The zeta potential values after changing the DBSA concentration ($\Delta\, c_{\text{tot}}$) [55].

1-butanol			*tert*-butanol		
$\Delta\, c_{\text{tot}}$ /mM	ζ /mV	μ /(µm cm/(V s))	$\Delta\, c_{\text{tot}}$ /mM	ζ /mV	μ /(µm cm/(V s))
0	75 ± 2	0.301 ± 0.007	0	98 ± 5	0.174 ± 0.009
0.29	74 ± 2	0.297 ± 0.009	0.56	80 ± 4	0.142 ± 0.007
0.40	73 ± 3	0.29 ± 0.01	0.78	80 ± 5	0.142 ± 0.008
0.79	75 ± 2	0.302 ± 0.006	0.90	79 ± 4	0.141 ± 0.007
0.97	75 ± 2	0.302 ± 0.009	1.12	82 ± 4	0.146 ± 0.006
1.18	76 ± 3	0.31 ± 0.01	1.31	81 ± 5	0.145 ± 0.008

4.1.4 Interplatelet interactions

The colloidal stability of the alcohol suspensions depends on the interactions between the NPLs. Theoretical insights into the interplatelet interactions provide an understanding of the system in which long-range magnetic dipole-dipole interactions and electrostatic interactions prevail. Attractive magnetic dipole interactions would prevail over short-range repulsive interactions at a short distance, leading to aggregation. For example, the magnitude of dipolar interaction at $r = 10$ nm is higher than 700 $k_B T$ for the NPLs with average magnetic moments of $\sim 2 \cdot 10^{-18}$ A m^2. Therefore, stable colloidal suspensions cannot be prepared by steric stabilization alone, but sufficiently strong repulsive electrostatic interactions between the NPLs are required. The repulsive electrostatic interactions between the NPLs are provided by the high surface charge.

In the calculations of the average interaction energy (Eq. (3.12); the sum of Eq. (1.5) and Eq. (3.13)) for a pair of platelets, the orientation of the first disk $\mathbf{n}_1$ along the x-axis was fixed and the average interaction $\langle U(r) \rangle$ of the second disk was calculated. A comparison of the $\langle U(r) \rangle$ along the direction $\mathbf{n}_1$ (x-axis) and perpendicular to it (y-axis) (see Figure 1.12) is shown in Figure 4.5a. The comparison was made for the alcohols with κ^{-1} as estimated for the 30 g/l suspensions (see Table 4.3) and zeta potentials given in Table 4.4. The effective surface charge was calculated using Eq. (3.17) and was $14e_0$, $15e_0$, $22e_0$, and $22e_0$ in *tert*-butanol, 1-hexanol, 1-butanol, and 2-propanol, respectively. The numerically calculated $\langle U(r) \rangle$ for the disks in 1-butanol ($\kappa^{-1} = 26$ nm) in the xy-plane are shown in Figure 4.5b. We observed that the interaction between the disks is repulsive and anisotropic. Decreasing the Debye screening length increases the anisotropy of the interaction. The disks can come to a closer distance oriented in the x-direction (i.e., when oriented face to face). In this direction, a finite barrier of a few tens of $k_B T$ occurs. When the barrier is smaller than about 10 $k_B T$, the disks aggregate irreversibly. Comparison of the barriers for the suspensions in all four alcohols showed that 1-butanol is the alcohol that provides the best colloidal stability among the alcohols studied. Decreasing the κ^{-1} increases the barrier (see Figure 4.5c) because the effective charge of the NPLs (Eq. (3.17)) increases with decreasing κ^{-1}. However, if the Debye length becomes too small, the magnetic dipole energy prevails and the NPLs can come into direct contact and aggregate. A small enough κ^{-1} causes a minimum in $\langle U(r) \rangle$ to appear on each side of the disk (see Figure 4.5c and Figure 4.5d). When these minima deepen more than about $k_B T$, the disks begin to flocculate, which can lead to sedimentation or, in the case of a concentrated suspension, reversible aggregation [55].

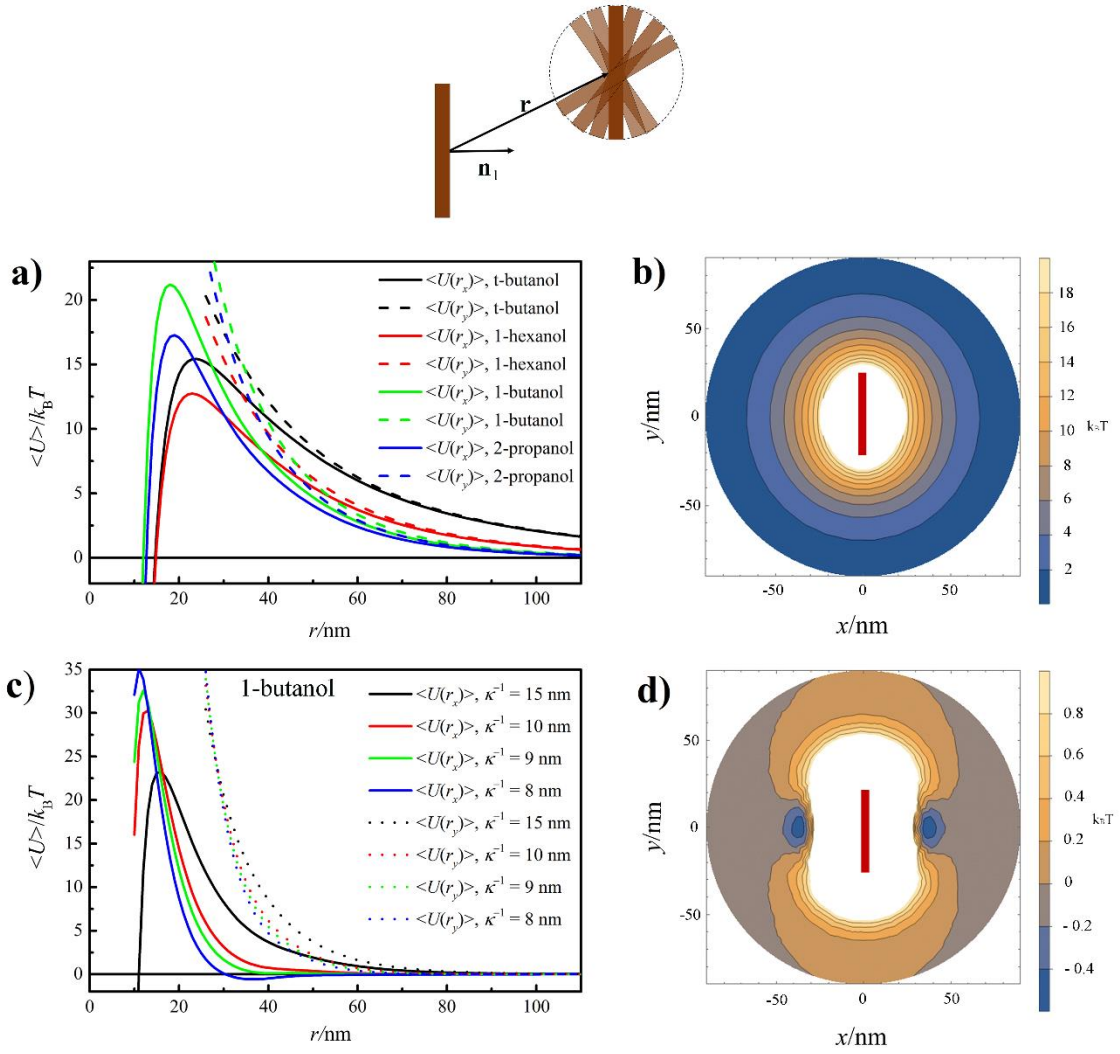

Figure 4.5: The average interaction calculated numerically (as the sum of Eq. (1.5) and Eq (3.13)) for a pair of disks with different relative orientations, as shown at the top of the figure. $\mathbf{r}$ is a vector connecting the centers of the disks, and $\mathbf{n}_1$ is a vector denoting the orientation of a disk. a) Average interaction between disks in the studied alcohols for the suspensions with a concentration of 30 g/l and $\boldsymbol{\kappa}^{-1}$ from Table 4.3, b) contour plot for the interaction in 1-butanol at $\boldsymbol{\kappa}^{-1} = 26$ nm, c) comparison of the interactions between disks in 1-butanol at different $\boldsymbol{\kappa}^{-1}$ values, d) contour plots of the interaction in 1-butanol at $\boldsymbol{\kappa}^{-1} = 8$ nm, where the side view of the first disk is schematically shown as a dark red rectangle ($\mathbf{n}_1$ fixed along the x-axis) as in b) [55].

In the first part of the dissertation, we have studied the electrostatic interactions between the DBSA-modified NPLs dispersed in different alcohols. The second part will deal with the phase behavior of the ferromagnetic nematic suspensions that were prepared first in 1-butanol [123]. The importance of the DBSA for the colloidal stability was shown earlier [62]. The total fraction of DBSA in alcohol suspensions significantly affects the volume fraction of NPLs required for the formation of the ferromagnetic nematic phase due to the dynamic equilibrium between adsorbed and dissolved DBSA. High concentrations of dissolved DBSA increase the ionic strength of the suspensions and can eventually lead

to aggregation by high screening of the charge and reducing the κ^{-1}. At the same time, too low concentration of adsorbed DBSA may also lead to aggregation by diluting the surface coverage that provides colloidal stability. 1-Butanol proved to be the best solvent among the investigated alcohols for the preparation of highly stable ferromagnetic nematic suspensions. This was confirmed despite moderately smaller κ^{-1} than *tert*-butanol and 1-hexanol, because 1-butanol suspensions still have a sufficiently high surface charge and, at the same time, a sufficiently low dielectric constant [55].

Based on these results, our choice of solvent for the next chapter on the phase behavior of BHF-DBSA-modified NPLs was limited to 1-butanol.

4.2 Phase Behavior of 1-butanol Suspensions with BHF NPLs

The discovery of a liquid magnet prepared from DBSA-modified BHF NPLs by Shuai et al. [123] presented a new interesting ferromagnetic system that led us to perform more detailed studies. To evaluate the phase behavior of alcohol suspensions, we considered parameters that we expected to affect the isotropic-nematic volume fraction ϕ_{IN}, also based on the results presented in Chapter 4.1. We studied the effects of the average equivalent diameter of the NPLs, their magnetization, and electrostatic interaction energy on the ϕ_{IN} in the studied suspensions. The obtained results are presented in the following chapters.

The results in this chapter (as well as the parts in Chapter 3 used to obtain these results) have been published and are reproduced from [125] [Patricija Hribar Boštjančič, Žiga Gregorin, Nerea Sebastián, Natan Osterman, Darja Lisjak, and Alenka Mertelj Journal of Molecular Liquids 2021

DOI: 10.1016/j.molliq.2021.118038 [125]. Copyright [2021] Elsevier. https://www.sciencedirect.com/science/article/abs/pii/S016773222102763X

4.2.1 Properties of the nematic suspensions

The suspensions used for the phase behavior evaluation were prepared using the centrifugation procedure described in Chapter 3.2.4. The nematic parts of the centrifuged scandium-substituted sample were Sc-middle and Sc-bottom, while in the case of indium substituted sample only In-bottom was ordered to the nematic phase. The nematic suspensions were characterized to determine the initial volume fraction of the NPLs ϕ, the average equivalent diameter, and the magnetic properties of the NPLs, which distinguish in different centrifuged parts, namely bottom, middle, and top. The results are shown in Table 4.6, Figure 4.6 and Figure 4.7. The bottom parts of the samples had on average more NPLs with larger equivalent diameter than the middle and the top parts. The separation in diameter of the NPLs was observed from the TEM images, shown in Figure 4.8 [125].

Table 4.6: Properties of the as-prepared suspensions and NPLs [125].

Sample	In-bottom	Sc-bottom	Sc-middle	Sc-top
Equivalent diameter/nm	52	54	45	31
Standard deviation/nm	22	21	18	14
M_s/(A m^2/kg)	29	38	39	35
ϕ after centrifugation / %	8.2	7.4	5.2	1.2

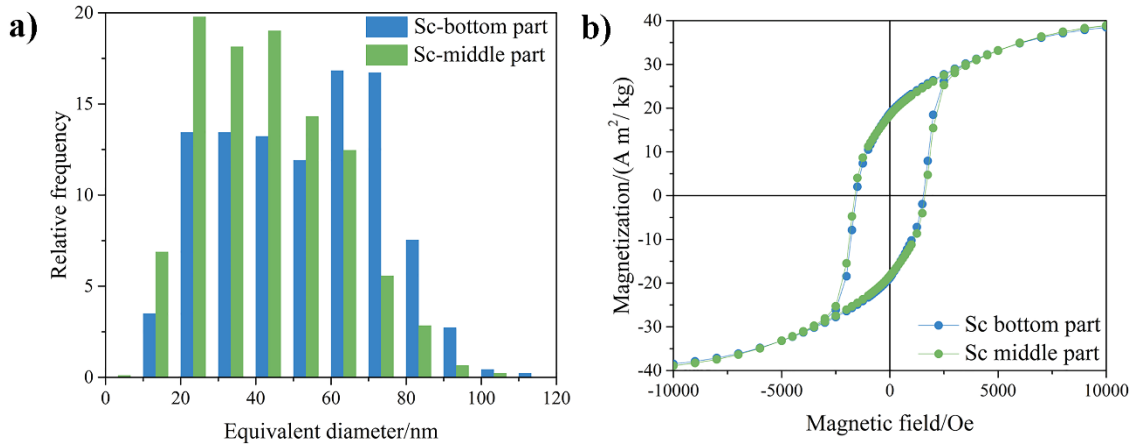

Figure 4.6: a) Equivalent diameter distributions and b) magnetic hysteresis loops of the Sc-middle and Sc-bottom [125].

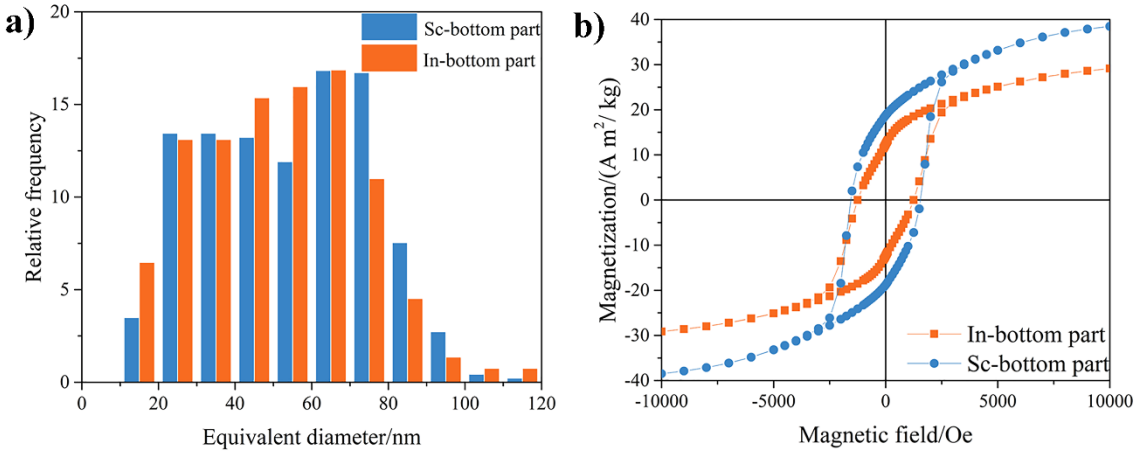

Figure 4.7: a) Equivalent diameter distributions and b) magnetic hysteresis loops of the Sc-bottom and In-bottom samples [125].

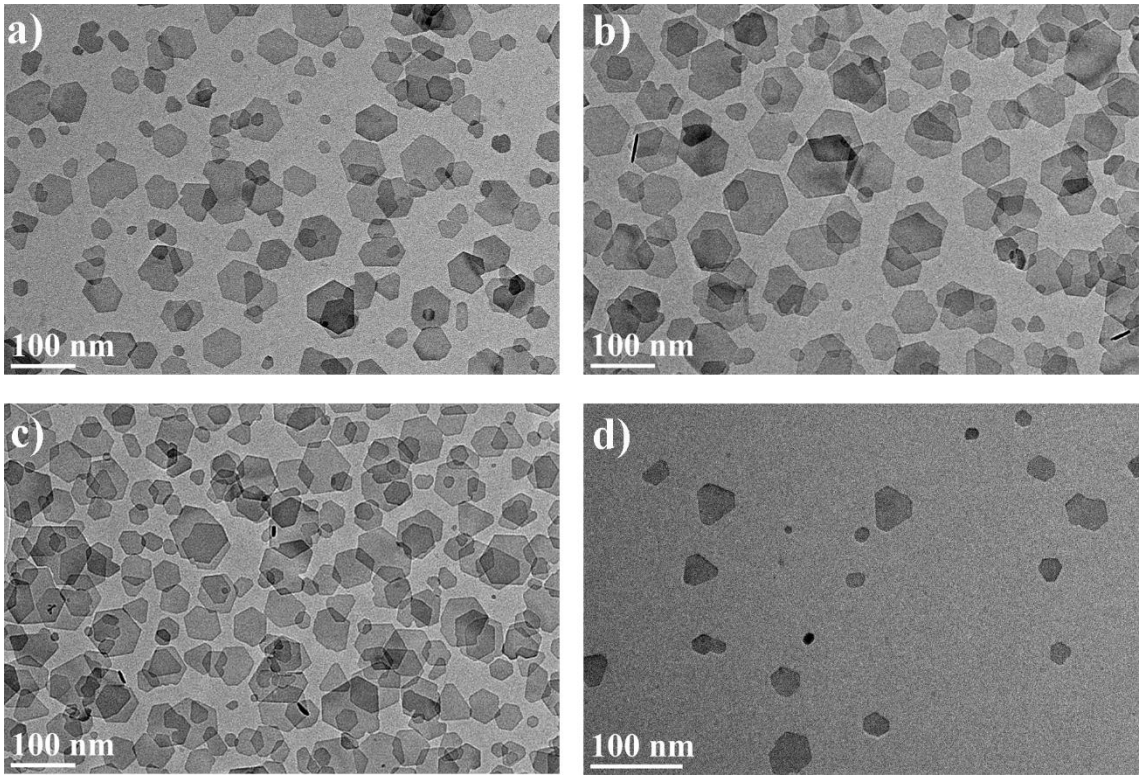

Figure 4.8: TEM images showing the difference in the size of the NPLs from the Sc-sample between a) the sample before centrifugation, b) Sc-bottom, c) Sc-middle, d) Sc-top.

The as-prepared nematic suspensions had about five times lower ϕ than was the ϕ of the first-prepared ferromagnetic ferrofluid ($\phi > 28$ %) [123] or some nonmagnetic systems [145], [146]. The reason for this is our optimized experimental procedure in which we adjusted the c_{dis}, magnetization, and average diameter of the NPLs. The MO response of our nematic suspensions with lower ϕ of the NPLs is significantly faster and takes less than a second compared to the response of the suspension with $\phi > 28$ %, which took several minutes or hours [123]. An external magnetic field affects the domain structure of the sample and moves the domain walls towards a single-domain state with magnetization aligned along the direction of the external magnetic field. The ordering process in the suspension can be observed with POM between crossed polarizers. The brightness of the sample changes when all NPLs are oriented on average in the same direction compared to the sample in zero field. Figure 4.9a shows a suspension in a capillary in zero field between crossed polarizers, with the black part (bottom) representing the isotropic phase and the fragmented brighter part (top) representing the nematic phase with magnetic domains. The angle between the polarizers and the capillary is 45°. When a magnetic field is applied along the capillary, as shown in Figure 4.9b, the sample appears bright due to ordering of the NPLs on average in the same direction [125].

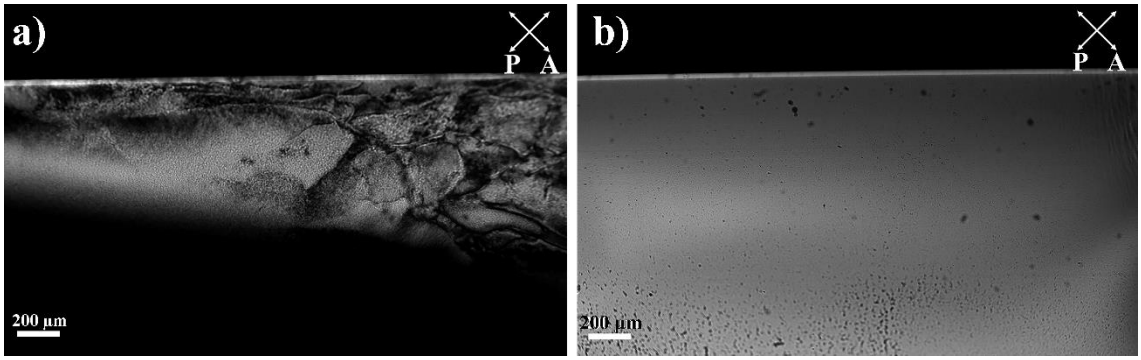

Figure 4.9: a) BHF NPLs nematic-isotropic suspension in 1-butanol in zero field and b) the same suspension as in a) under applied magnetic field of 1.4 mT in the → direction [125].

4.2.2 Influence of the equivalent diameter distribution of the NPLs

The NPLs were separated in diameter by the centrifugation procedure (see Chapter 3.2.4). The Sc-middle and Sc-bottom were both in the nematic phase. This allowed us to compare samples with the same saturation magnetization and electrostatic properties, but with different equivalent diameter distributions (see Figure 4.6 and Table 4.6). After centrifugation, the volume fraction of the Sc-middle was $\phi = 5.2$ % and the volume fraction of the Sc-bottom $\phi = 7.4$ %. The POM images of the Sc-middle and Sc-bottom nematic samples are shown in Figure 4.10a and Figure 4.10b, respectively. The smallest dilution (to $\phi = 5.1$ %) of the Sc-middle resulted in the transition to the isotropic phase, showing that the sample was already exactly at the ϕ_{IN}. In contrast, the Sc-bottom (Figure 4.10b) had to be diluted several times to reach the ϕ_{IN}, which was estimated to be at $\phi_{IN} = (4.6 \pm 0.1)$ %. Slightly below the ϕ_{IN} (at $\phi = 4.3$ %), we observed phase coexistence of isotropic and nematic phases [115]. The nematic phase formed thread-like structures that were surrounded by the isotropic phase (Figure 4.10c) [125].

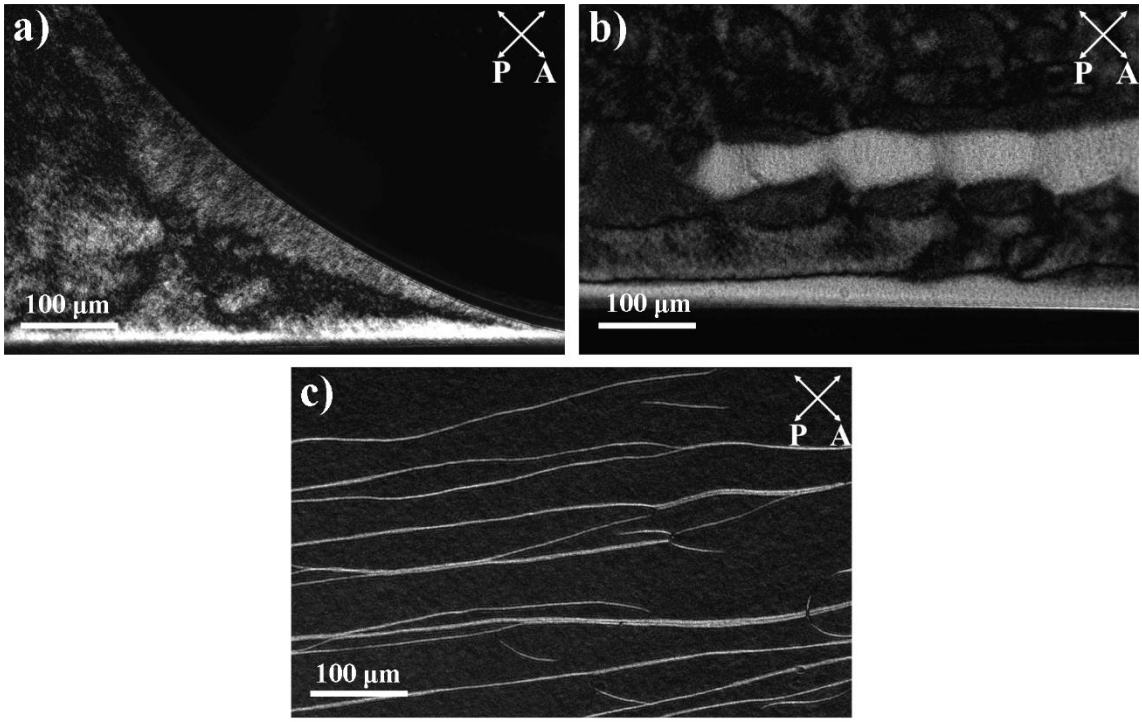

Figure 4.10: POM images of a) the Sc-middle at $\phi = 5.2$ % at the meniscus in the capillary, b) the Sc-bottom at $\phi = 4.7$ % and c) the phase coexistence in the Sc-bottom at $\phi = 4.3$ % [125].

4.2.3 Influence of DBSA concentration

As discussed in Chapter 4.1, the amount of DBSA in the suspension affects the ionic strength and thus, the electrostatic interactions between the NPLs. To evaluate the effect of c_{dis} on the ϕ_{IN}, we added known amounts of the DBSA solution with a concentration of 1.55 M to the nematic Sc-middle and Sc-bottom. The Sc-middle had an initial volume fraction of $\phi = 5.2$ % and the Sc-bottom was diluted accordingly just above the ϕ_{IN} value. In this case, the addition of the DBSA solution decreased the ϕ (due to the added solvent) while increasing the c_{dis} value. The Sc-middle, which was as-prepared right at its ϕ_{IN}, became isotropic after the first additions of the DBSA solution, as shown in Figure 4.11. However, after diluting the suspension for $\phi \sim 0.2$ % and increasing $c_{\text{dis}} > 28$ mM, the transition to the nematic phase was again observed (see Figure 4.11), which can be seen in the POM image shown in Figure 4.12a. A similar behavior was also observed for the Sc-bottom, where the ϕ_{IN} value decreased for ~ 0.6 % at $c_{\text{dis}} = 37$ mM (Figure 4.12b). Thus, we have shown that a sufficient increase in c_{dis} decreases the ϕ_{IN} value. The c_{dis} affects the κ^{-1} and the range of electrostatic interactions. At higher c_{dis}, the screening of the surface charge is stronger. Consequently, the κ^{-1} is smaller and the NPLs move to a closer distance, where a stronger magnetic interaction acts between neighboring NPLs. This shows the importance of the interplay of magnetic and electrostatic interactions between the NPLs for a nematic phase formation. In addition, the c_{dis} affects the effective shape anisotropy of the NPLs, which also affects the nematic phase formation [125].

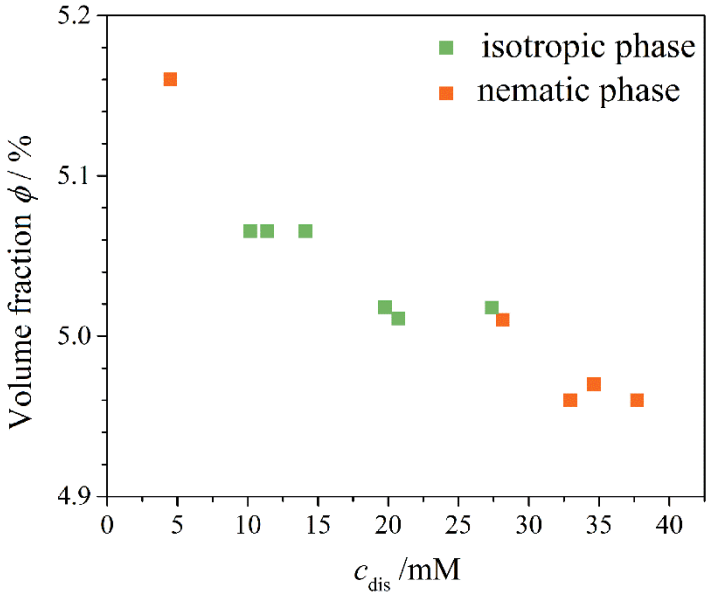

Figure 4.11: The change of phase with increasing c_{dis} in suspension. The initial Sc-middle with $c_{dis} = 4.5$ mM was in nematic phase. Dilution of the suspension with DBSA solution triggered the phase transition from nematic to isotropic phase, followed by an isotropic to nematic phase transition at $c_{dis} > 28$ mM. The suspension became nematic again at a ~ 0.2 % lower volume fraction than the volume fraction of the initial nematic suspension (ϕ = 5.16 %) [125].

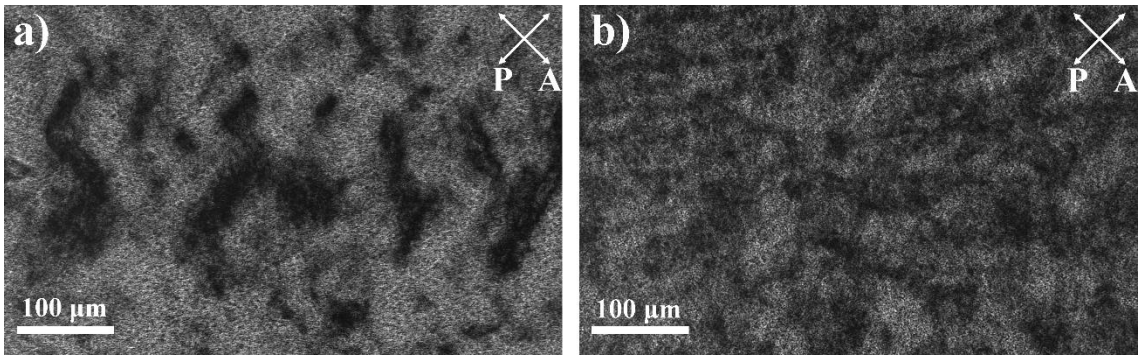

Figure 4.12: POM images after the addition of DBSA a) of the nematic Sc-middle at ϕ = 5.0 % and $c_{dis} = 28$ mM and b) the Sc-bottom at ϕ = 3.9 % and $c_{dis} = 37$ mM [125].

After the addition of the DBSA solution, the Sc-middle remained in the isotropic phase at c_{dis} below 28 mM, while an increase in the c_{dis} above 45 mM led to aggregation. Aggregation of the suspensions at higher amounts of DBSA can be observed with the naked eye. The suspensions lose the distinctive shine of colloidally stable suspensions and become opaque and lighter in color, as can be seen in Figure 4.13. Such an effect can also be observed locally in the suspensions after small additions of the DBSA solution. In this case, the opacity disappears after thorough mixing of the suspension, so the aggregation in this case is reversible. Another observation is that subsequent additions of the DBSA solution to the nematic suspensions slow down the MO response (under an applied magnetic field of 1.4 mT) to the point where the external field of 1.4 mT can no longer move the structures and the MO response disappears completely, which is a sign of gelation [125].

Figure 4.13: Aggregated (brighter and opaque) suspension with increased c_{dis} on the left and colloidally stable suspension (dark, shiny) on the right [125].

4.2.4 Influence of the magnetization of the NPLs

The contribution of magnetization to the phase behavior of the suspensions was evaluated by comparing Sc-substituted and In-substituted NPL suspensions based on the difference in their M_{s}. In order to obtain NPLs with different M_{s} and comparable equivalent diameter distribution (see Figure 4.7 and Table 4.6), a different type of substituting ion (Sc^{3+} and In^{3+}) was used. As expected, the In-substituted sample exhibited lower magnetization than the Sc-substituted one [43] (see Figure 4.7). After centrifugation, the two bottom parts were in the nematic phase (see Chapter 3.2.4) with initial volume fractions of $\phi = 7.4$ % (Sc) and 8.2 % (In). The phase transition to the isotropic phase occurred at ~ 2 % higher volume fraction in In-bottom sample than in the Sc-bottom sample (see Chapter 4.2.2), i.e., at $\phi_{\mathrm{IN}} = (6.6 \pm 0.2)$ % versus $\phi_{\mathrm{IN}} = (4.6 \pm 0.2)$ %, respectively. The results are shown in Figure 4.14.

We expected that mixing the Sc- with In-substituted NPLs would decrease the magnetization of the mixed sample and shift the ϕ_{IN} into the region of ϕ between threshold volume fractions of the pure Sc- and In-samples. Our expectations were confirmed. The ϕ_{IN} of the Sc-bottom and In-bottom (1:1) mixture was $\phi_{\mathrm{IN}} = (5.2 \pm 0.1)$ % (see Figure 4.14). At the same time, some interesting structures formed in the mixed suspensions, which can be seen in Figure 4.15. Such string-like structures are not present in the pure Sc- and In-bottom, from which the mixture was prepared. The structures were visible in zero field (see Figure 4.15a) and after an applied magnetic field of ≤ 1.4 mT. The field oriented the NPLs and the suspension was bright, while revealing long string-like aggregate structures that were eventually broken with an alternating field (1.4 mT, 10 Hz). The interesting behavior prompted us to prepare a mixture with a larger difference in the interplatelet interactions of the basic components, i.e., by mixing Sc-bottom with In-middle (still isotropic). The structures were also observed in this mixture in the absence of an external magnetic field (see Figure 4.15b) and rapidly separated in the alternating field (1.26 mT, 10 Hz). However, the structures began to form again ~ 20 min after the field was switched off. One way to explain the formation of the string-like structures is based on the difference in the magnetic moments of the two mixed samples. As will be explained

in the next chapter, the interaction between the Sc-NPLs with the larger magnetic moment is predominantly attractive and they tend to order into nematic phase, while the interaction between the In-NPLs with the smaller magnetic moment is repulsive and, at given ϕ, they remain in the isotropic phase. Consequently, phase separation of the Sc-rich regions (nematic, bright) and In-rich regions (isotropic, dark) is observed as string-like structures (see Figure 4.15) [125].

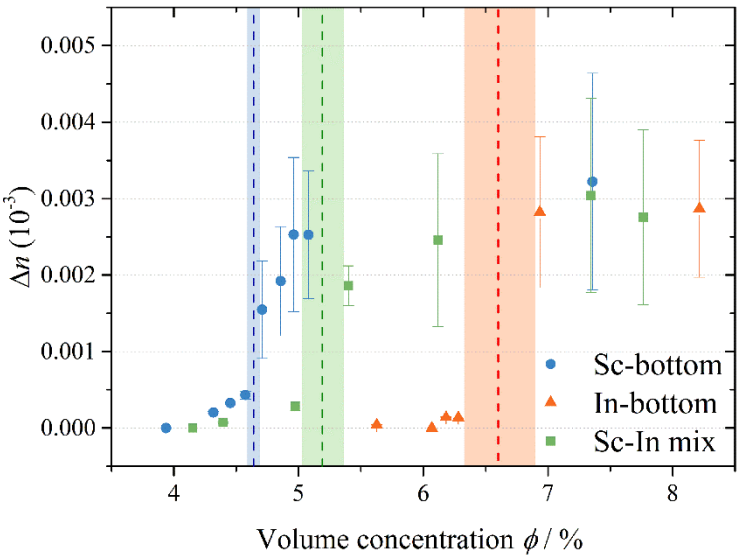

Figure 4.14: Birefringence for the Sc-bottom, In-bottom and the mix of both suspensions, where the colored columns represent the threshold volume fractions (ϕ_{IN}) of these samples [125].

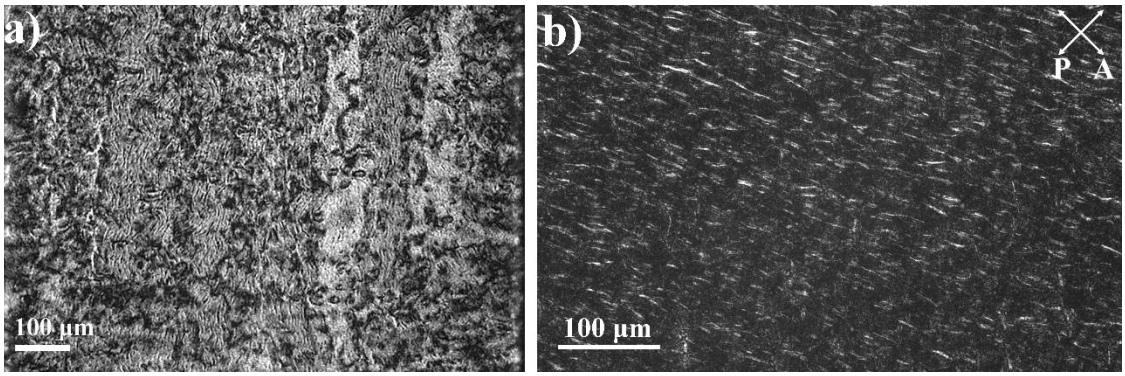

Figure 4.15: POM images in the zero field. String-like structures formed in a mixture of a) Sc-bottom and In-bottom at $\phi = 7.3$ % and b) Sc-bottom and In-middle at $\phi = 4.7$ % [125].

4.2.5 Polydispersity and the interplatelets interactions

The main interplatelet interactions in the alcohol suspensions of the DBSA-modified NPLs are magnetic and electrostatic [55]. The latter are affected by the concentration of DBSA, while the anisotropic magnetic interactions depend on the NPLs size and type; in our case, the In- or Sc-substituted sample. The polydispersity of the NPLs, shown in Figure 4.6a and Figure 4.7a, affects the interplatelet interactions and makes them polydisperse. The

polydispersity of the interplatelet interactions was calculated between two parallel NPLs, placed as schematically shown in Figure 4.16 and separated by a distance r. Such an orientation is most likely present in the ferromagnetic nematic suspensions and in this orientation the magnetic interaction energy between the NPLs is the strongest. The total interaction was calculated with Eq. (3.16). The results are shown in Figure 4.16a, where the interaction energy is averaged over the equivalent diameter distribution of the NPLs (see Figure 4.6a and Figure 4.7a) for the Sc-middle, Sc-bottom, and In-bottom. Figure 4.16b–d depicts the variation of the total interaction energy with the size of the NPLs. It is repulsive between smaller NPLs, while it becomes attractive between larger NPLs at a distance of about 40 nm. The average interaction energy changes with Debye screening length, as shown in Figure 4.16e for Sc-middle NPLs. At a closer distance, the minimum deepens and can lead to reversible aggregation. This is in agreement with the experimental observation where the aggregation of the suspensions was observed after the addition of DBSA. The latter increased the ion concentration and consequently decreased the Debye length (see Chapter 4.2.3) [125].

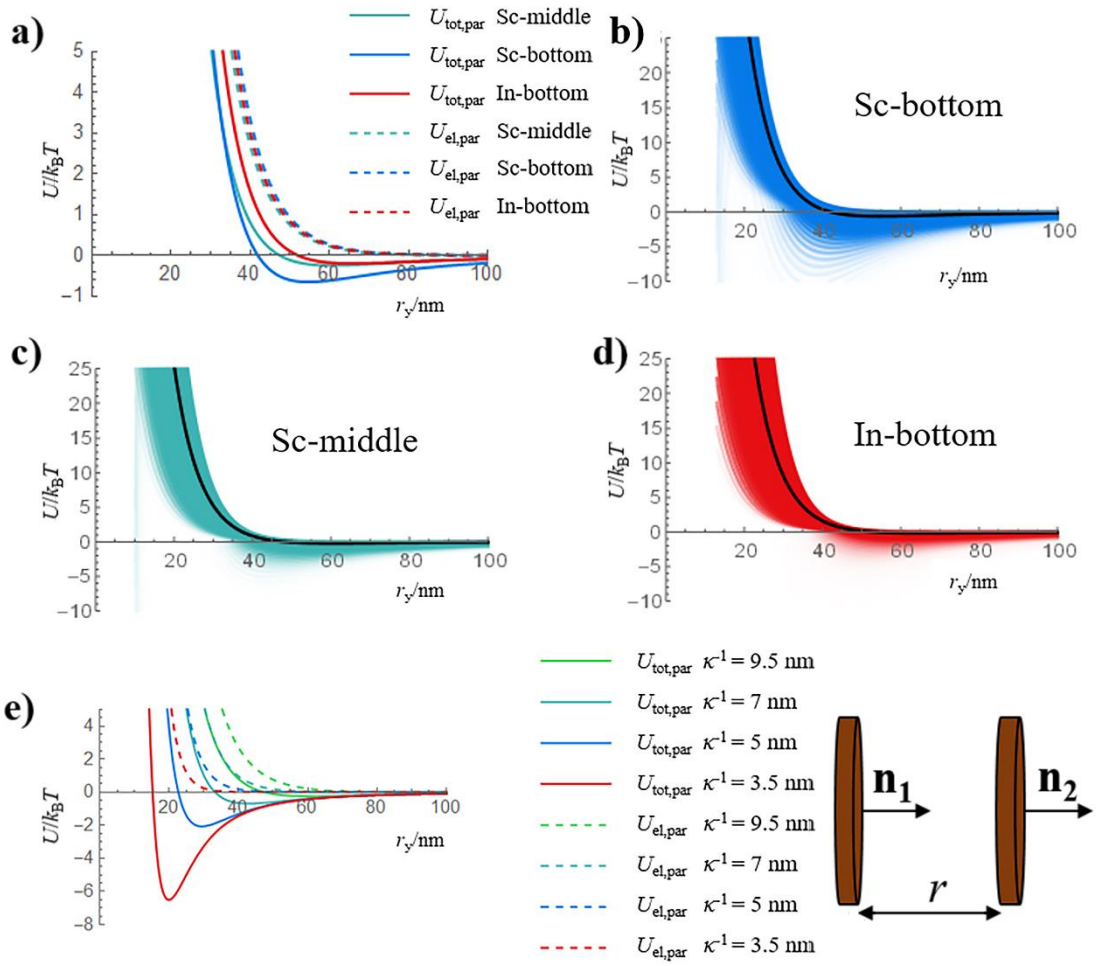

Figure 4.16: a) Calculated electrostatic $U_{el,par}$ (dashed lines) (Eq. (3.15)) and total (solid lines) interaction energy $U_{tot,par}$ (Eq. (3.16)). b), c), d) The polydispersity of the interaction, total interaction energy for all combinations of NPLs diameters in histograms (see Figure 4.6a and Figure 4.7a). e) Dependence of the average interaction energy between two parallel platelets on the Debye length for Sc-middle [125].

4.2.6 Summary of phase behavior and stability

Nematic ordering is common in suspensions of nonmagnetic platelets, e.g. [118], [145], [147]. The effective volume fraction $\phi_{\mathrm{IN,eff}}$, above which a suspension of uncharged nonmagnetic platelets is in nematic phase, is related to the excluded volume and has been shown to be between 3 and 4 [110], [121], [122]. Table 4.7 lists the experimentally determined threshold volume fractions ϕ_{IN}, the calculated effective volume fractions $\phi_{\mathrm{IN,eff}}$ defined with Eq. (1.13) and the rescaled volume fractions defined as follows:

$$\phi_{\mathrm{IN,resc}} = \frac{N}{V_{\mathrm{s}}} \langle V_{\mathrm{eff}} \rangle \tag{4.2}$$

and

$$\phi_{\mathrm{IN,eff,resc}} = \frac{N}{V_{\mathrm{s}}} \left\langle D_{\mathrm{eff}}^3 \right\rangle \tag{4.3}$$

where

$$V_{\mathrm{eff}} = \frac{\pi}{4} D_{\mathrm{eff}}^2 h_{\mathrm{eff}} \tag{4.4}$$

The values are represented for Sc-middle, Sc-bottom, and In-bottom. κ^{-1} was determined to be 9.5 nm using the procedure described in detail in Chapter 3.4.2 [55]. The values of κD are therefore around 5. The aspect ratio h/D of the BHF NPLs depends on the diameter of the NPLs since the thickness is approximately constant [44], [55]. The calculated effective volume fractions are very small, between 1.1 and 1.6 (see Table 4.7), while the effective rescaled volume fractions, for which the NPLs were assumed to be for a Debye length larger (larger for 9.5 nm in each direction), are between 2.4 and 3.4 [125], much more similar to the values determined for nonmagnetic systems [121], [122].

Table 4.7: The experimentally determined threshold volume fractions and calculated properties for the suspensions studied [125].

		Sc-middle	Sc-bottom	In-bottom
Experimentally determined threshold volume fraction	ϕ_{IN}	0.052	0.046	0.066
Aspect ratio	$\langle h/D \rangle$	0.10	0.08	0.09
Magnetic moment	$\langle p_{\mathrm{m}} \rangle / (10^{-18}$ A m$^2)$	1.37	1.96	1.35
Effective surface charge	$\langle e_0 \rangle / e_0$	43	52	49
Effective volume fraction	$\phi_{\mathrm{IN,eff}} = \frac{N}{V_{\mathrm{s}}} \langle D^3 \rangle$	1.1	1.1	1.6
Rescaled volume fraction	$\phi_{\mathrm{IN,resc}} = \frac{N}{V_{\mathrm{s}}} \langle V_{\mathrm{eff}} \rangle$	0.20	0.16	0.23
Effective rescaled volume fraction	$\phi_{\mathrm{IN,eff,resc}} = \frac{N}{V_{\mathrm{s}}} \left\langle D_{\mathrm{eff}}^3 \right\rangle$	2.6	2.4	3.4
Debye parameter	$\langle \kappa D \rangle$	4.7	5.7	5.5

The dipolar magnetic interaction between the NPLs is strongly anisotropic and on average attractive. Without electrostatic repulsion, the NPLs would aggregate because the magnetic interaction directs the assembly of the NPLs into columns. The pair interaction energy, which is a combination of dipole magnetic and electrostatic interactions, provides an explanation for the complicated many-body problem of ferromagnetic nematic ordering. The pair interaction energy can be repulsive at all distances or repulsive at larger distance and attractive at shorter ones. This can be seen as a minimum of the interaction energy leading to the formation of columns if it is too deep (see Figure 4.16) [148] due to positional and orientational correlations between the NPLs. SAXS and small-angle neutron scattering (SANS) measurements show that there are short-range positional and orientational correlations between the NPLs. However, no significant formation of columns was observed in the alcohol suspensions of the BHF NPLs [124], [149]. The reason could be that the large columns (aggregates) sediment during the centrifugation procedure used in sample preparation due to strong forces and are subsequently discarded. The second reason that affects the formation of columns is the polydispersity in the diameter of the NPLs, which in our case is 40 %. Polydispersity is known to be an important parameter that disfavors the formation of columns in favor of the lamellar phase [120]. The polydispersity in the diameter of the NPLs affects the polydispersity of the interaction, as depicted in Figure 4.16b–d. The Sc-NPLs with larger magnetic moments (see Table 4.7) move closer together and form elongated regions of ordered nematic phase. In contrast, the electrostatic interaction prevails over the magnetic attraction between the In-NPLs with smaller magnetic moment (see Table 4.7) and the NPLs remain in the isotropic phase.

The surface charge of the NPLs determines the magnitude of the electrostatic interaction and the Debye screening length determines the range of the electrostatic interaction. The NPLs in the In-bottom and Sc-middle have similar magnetic moments but different surface charges (see Table 4.7), which is due to the different diameter of the NPLs. The NPLs in Sc-middle with a lower surface charge tend to order to nematic phase at lower volume fractions than the NPLs in the In-bottom sample, because the NLPs with a lower surface charge can move closer in the direction, where they align ferromagnetically (see Figure 4.16a). The Debye screening length is affected by the addition of DBSA. A higher concentration of c_{dis} decreases the Debye screening length and shifts the ϕ_{IN} to lower values. However, the NPLs can also get stuck in a minimum of the interaction, leading to a reversible destabilization of the suspension, as observed when the c_{dis} is increased.

The results show that the ϕ_{IN} is controlled by the combination of the repulsive screened electrostatic interaction and the attractive dipolar magnetic interaction. The ϕ_{IN} can be decreased by increasing the magnitude of the magnetic interaction and by changing the magnitude and/or range of the electrostatic interaction. One can see that the change in magnetic interaction has the most significant impact on the ϕ_{IN}. However, the magnetic interaction energy must be balanced with the electrostatic interaction energy to keep the attractive interaction in the intermediate range (which favors the nematic ordering) and to have a short-range repulsive interaction energy (which prevents aggregation) [125].

4.3 Other Strategies for Colloidal Stabilization of BHF NPLs

The detailed study of suspensions containing DBSA-modified NPLs described in the first two parts of this dissertation provided an insight into the mechanisms for colloidal stabilization of the NPLs in isotropic and nematic phases. In this chapter, we focused on possible surface modifications of the BHF NPLs that would enable colloidal stability in other isotropic solvents and NLC 5CB. For this purpose, we used non-promesogenic and promesogenic ligands.

The non-promesogenic ligands used are DBSA, PSA, PHDA, Pether, OA, and RA (see their structure in Figure 3.1). The first three were used for colloidal stabilization in water (PSA and Pether also in alcohol) because they contain functional groups that can bind to the surface of the NPLs and/or provide a surface charge. On the other hand, OA and RA have been shown to be suitable ligands for surface modification and colloidal stabilization of iron oxide nanoparticles in nonpolar solvents [65]. Therefore, we decided to modify the surface of BHF-NPLs with OA and RA for colloidal stabilization in toluene, chloroform, and 5CB. Other promising ligands for stabilization of small spherical particles in NLCs are promesogenic ligands [71], [79], [101]. We have used two types of promesogenic ligands (dendrimer, 10POCB (see their structure in Figure 3.1)) for the surface modification of NPLs. Since the surface modification with only one type of promesogenic ligand did not stabilize the NPLs in either isotropic or nematic medium, we decided to modify the NPLs with a combination of promesogenic with other ligands (RA, HPA, ODPA and AL). A summary of the results obtained in this chapter can be found in Table 4.8 (see Chapter 4.3.3).

4.3.1 Surface modification with one type of ligand

4.3.1.1 BHF-DBSA NPLs in water

Since surface modification with DBSA provides good colloidal stability in alcohols, our goal was to prepare NPLs with a double layer of DBSA in water by post-synthetic surface modification of the NPLs (see the procedure in Chapter 3.2.3). The zeta potential values of BHF-DBSA NPLs in water were determined by lowering the pH from 11 to 3. The values between pH 11 and pH 6 match with the zeta potential values of the bare BHF NPLs, as depicted in Figure 4.17, suggesting that the DBSA molecules are not bound to the NPLs. Lowering the pH below the isoelectric point of the bare BHF NPLs results in a positive zeta potential (see Figure 4.17). Positively charged NPLs electrostatically attract dissociated DBSA molecules, which attach to the surface of the NPLs. The remaining DBSA forms a double layer that is negatively charged below the isoelectric point. The dissociated sulfonic group (see the DBSA structure in Figure 3.1) in the second layer ensured that the zeta potential of the NPLs is negative at pH below 6 (see Figure 4.17), even at very low pH values (pKa < 1). Such behavior is typical for acidic functional groups (e.g. carboxyl, phosphonic) on a surface, e.g., [69], [150]. On the other hand, the zeta potential of DBSA-modified NPLs in alcohols is positive (see Table 4.4) and is explained by a different mechanism (see Chapter 4.1), which does not occur in water. In aqueous suspension of BHF-DBSA, the excess of DBSA provides the formation of the double layer and the colloidal stability.

The aqueous BHF-DBSA suspension had very poor colloidal stability compared to the alcohol suspensions of DBSA-modified NPLs. The aqueous suspension sedimented within a few weeks.

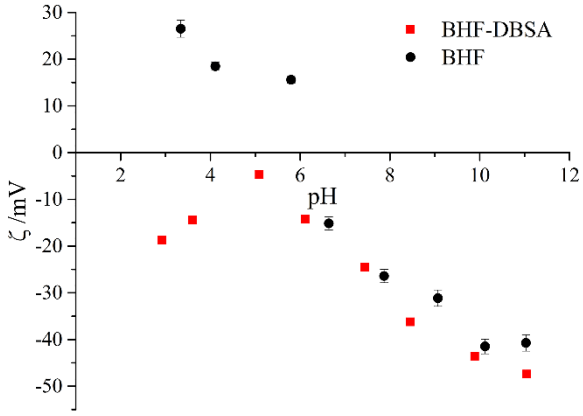

Figure 4.17: Zeta potential values of the BHF-DBSA NPLs in water compared to the zeta potential of the bare BHF NPLs.

4.3.1.2 BHF-PSA NPLs

PSA is a ligand with two functional groups, namely sulfonic and phosphonic (see the ligand structure in Figure 3.1), separated by a 12-C alkyl chain. In the IR spectrum of PSA, shown in Figure 4.18a [69], typical bands for phosphonic group are observed between 1264 cm^{-1} and 1203 cm^{-1}, and between 1088 cm^{-1} and 1046 cm^{-1} attributed to P=O and P-OH [151], [152]. Strong bands that could be assigned to P-O-C and P-C are also present at 994 cm^{-1}, 777 cm^{-1}, 791 cm^{-1} and 716 cm^{-1} [152]. The distinct bands for the phosphonic group overlap with some typical bands for the sulfonic functional group, i.e. SO_2, SO_3, and SO vibrations at 1168 cm^{-1} and 1046 cm^{-1} [152], [153]. Thus, some bands can be assigned to one of the two functional groups. After the binding of PSA to the surface of the NPLs, the typical phosphonic group bands merge between 1100 cm^{-1} and 900 cm^{-1} [76], [151]. This is the main difference between free and bound phosphonic acid and an indicator that the ligands are bound to the surface of the NPLs. At the same time, the sharp intense band for S=O vibrations disappears at 1223 cm^{-1}, indicating that the PSA is bound to the surface of the NPLs also with the sulfonic group. The result may be a combination of free sulfonic acid and phosphonic acid groups or neither, i.e., a hydrophobic surface.

The negative zeta potential of the BHF-PSA NPLs throughout the pH range of the measurement (pH 2–11) confirms the successful surface modification (see Figure 4.18b) [69]. The negative potential values may be a consequence of dissociated sulfonic acid or a combination of both, i.e., sulphonic and phosphonic acid. The BHF-PSA suspensions are colloidally stable in both water and 1-butanol. The zeta potential measured in 1-butanol had a value of (–57.3 ± 2.6) mV. The zeta potential value is different from that of the DBSA-modified NPLs in alcohols, which were positive (see Table 4.4), although in both cases a sulfonic group interacts with the solvent. The main difference must be the charging mechanism.

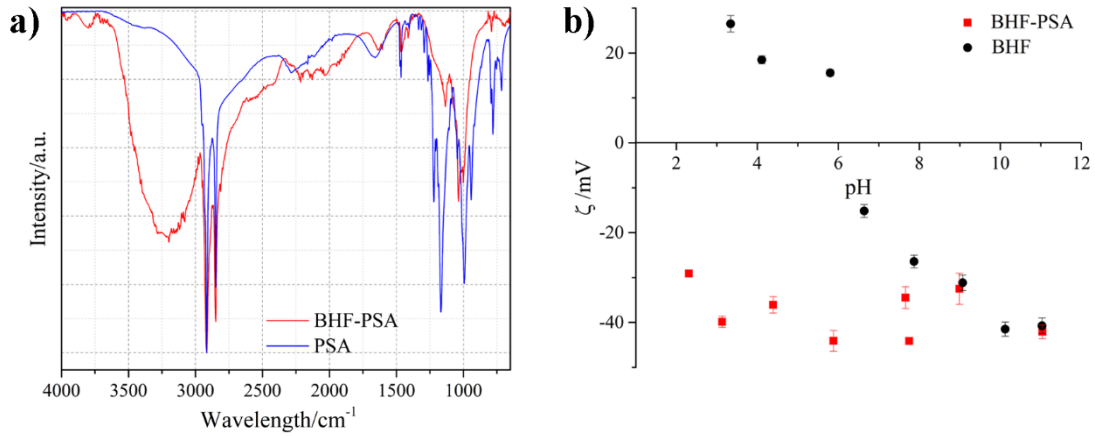

Figure 4.18: a) IR spectra of the ligand PSA and the PSA-modified NPLs and b) zeta potential values of the BHF-PSA NPLs compared to the zeta potential of the bare BHF NPLs [69].

4.3.1.3 BHF-PHDA NPLs

PHDA is a ligand with two functional groups, namely carboxylic and phosphonic, separated by a 16-C alkyl chain (see structure in Figure 3.1). In the IR spectrum of PHDA, shown in Figure 4.19a, there are strong bands for the C-H alkane stretching at 2916 cm^{-1} and 2850 cm^{-1}, which can also be observed in the IR spectrum of BHF-PHDA NPLs. At 1670 cm^{-1}, there is a strong C=O band originating from the vibrations of the carboxyl group. The band at 1467 cm^{-1} can be attributed to the in-plane C-O-H bending, while the band at 1207 cm^{-1} and several bands between 1106 cm^{-1} and 933 cm^{-1} are attributed to the P=O and P-OH [151], [152]. These bands are combined into a broad band at 1041 cm^{-1} when PHDA is bound to the NPLs (BHF-PHDA). The band in the IR spectrum of BHF-PHDA at 1558 cm^{-1} may be attributed COO^- stretching vibrations and newly formed carboxyl complexes [64], [152], suggesting that the binding of PHDA to the iron oxide surface was not exclusively via phosphonic groups but also via the carboxyl group. The zeta potential of BHF-PHDA NPLs dispersed in water is negative above pH 2 (see Figure 4.19b), confirming that the surface modification was successful.

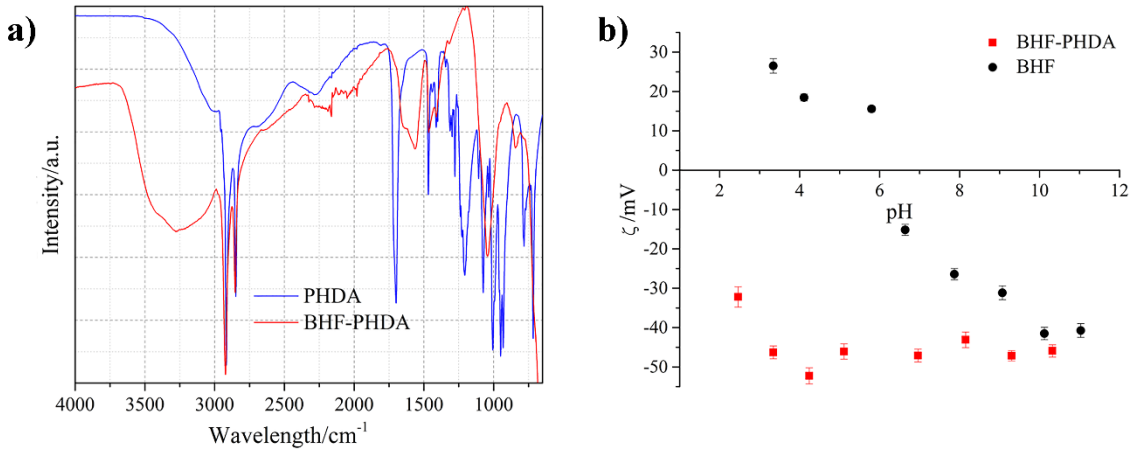

Figure 4.19: a) IR spectra of the ligand PHDA and the modified NPLs and b) zeta potential values of the modified BHF-PHDA NPLs compared to the zeta potential of bare BHF NPLs.

4.3.1.4 BHF-Pether NPLs

The BHF-Pether NPLs were prepared by direct surface modification of the bare NPLs and by a ligand exchange procedure (see procedure in Chapter 3.2.3). Two suspensions in different solvents (i.e., 1-butanol and water) with different properties were obtained, as shown in Figure 4.20.

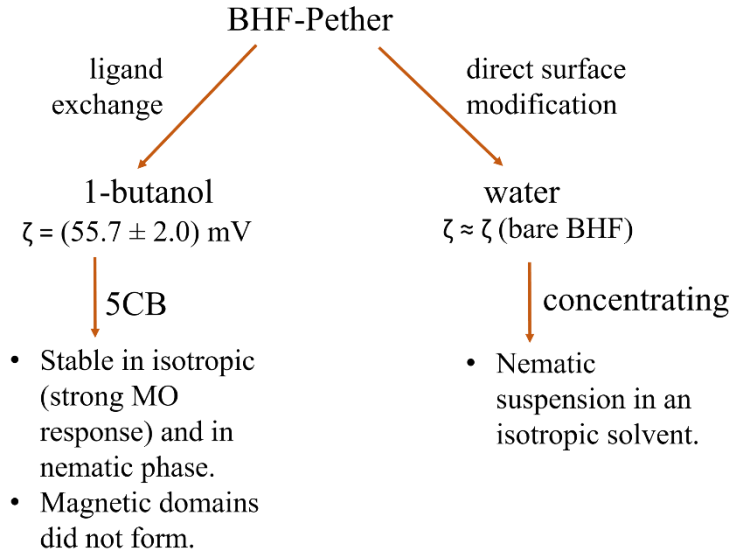

Figure 4.20: Schematic of the behavior of the BHF-Pether NPLs in different solvents with respect to the Pether surface modification procedure.

In the IR spectrum of the ligand, shown in Figure 4.21, typical bands for the phosphonic group are present, namely for P=O, P-O-H, P-C, ranging from 1085 cm^{-1} to 712 cm^{-1} [151], [152]. The bands overlap with the C-O stretch band for the ether groups in the ligand

chain (see structure in Figure 3.1), which is expected around 1100 cm^{-1}. The BHF-Pether NPLs dispersed in 1-butanol (denoted as BHF-Pether (1-butanol)) were prepared from a colloidally stable 1-butanol suspension of BHF-DBSA NPLs by ligand-exchange (see procedure in Chapter 3.2.3). The IR spectrum of the BHF-Pether NPLs (1-butanol) was compared with the IR spectrum of the original, i.e., BHF-DBSA NPLs and the Pether ligand (see Figure 4.21). The individual bands in the range between 1150 cm^{-1} and 900 cm^{-1} in the ligand spectrum combine to form a broad band in the case of BHF-Pether NPLs. This indicates that the Pether binds to the surface of the NPLs during ligand exchange. Comparing the BHF-Pether and BHF-DBSA NPLs spectra, we can see that the bands attributed to DBSA (benzene ring and sulfonic group) at 1409 cm^{-1}, 1202 cm^{-1}, 1155 cm^{-1}, 1130 cm^{-1}, 1039 cm^{-1} and 1009 cm^{-1} [62], [154] are absent in the BHF-Pether spectrum, or they overlap with the bands of the Pether ligand. We can conclude that most of the DBSA has been replaced by Pether. However, the IR analysis alone does not prove that the ligand exchange was complete. The BHF-Pether NPLs dispersed in water, i.e., BHF-Pether NPLs (water), were prepared using a direct surface modification procedure (see procedure in Chapter 3.2.3).

The IR spectrum of the BHF-Pether NPLs (water) confirmed that Pether is bound to the surface of the NPLs, as evidenced by a significant broadening of the phosphonic bands (see Figure 4.21).

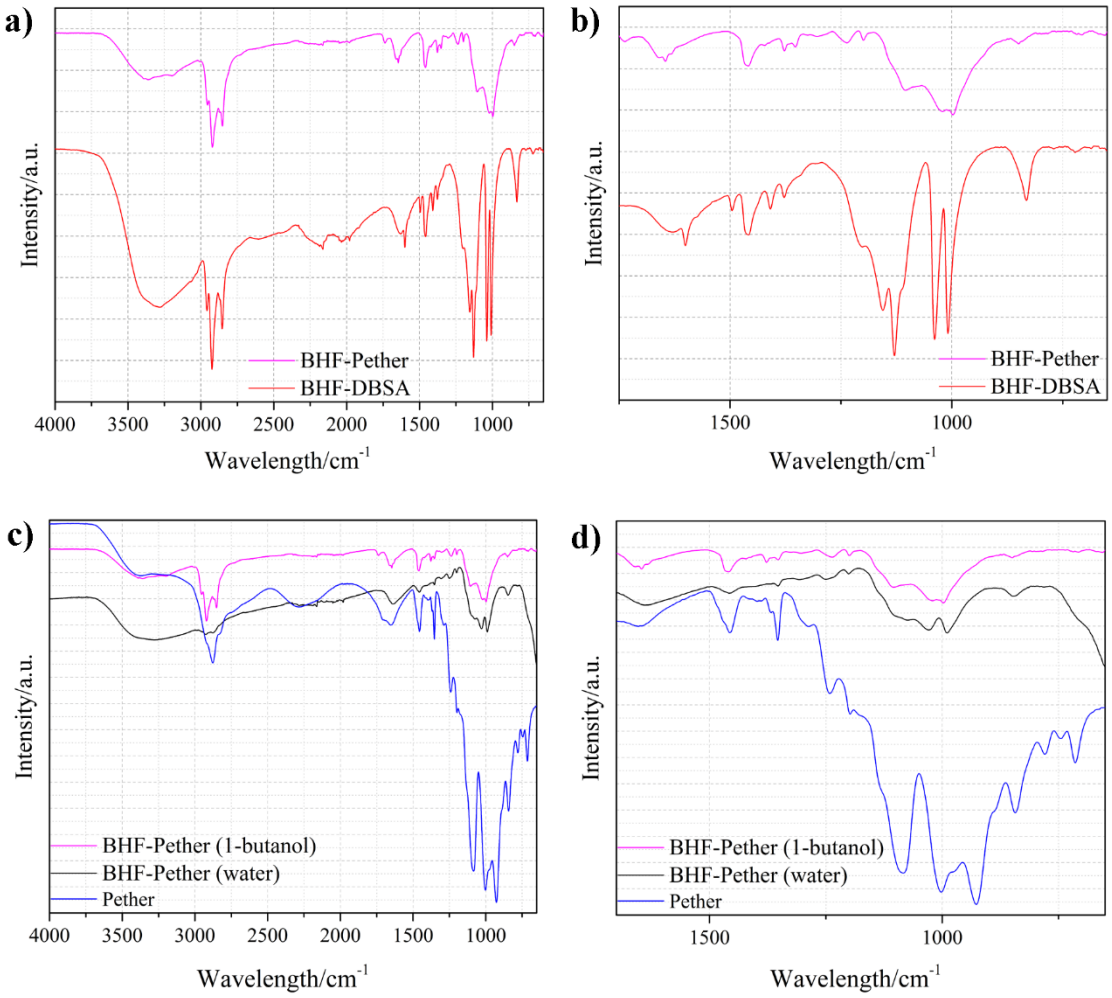

Figure 4.21: IR spectra of a) BHF-Pether (1-butanol) compared to BHF-DBSA NPLs, b) zoomed IR spectra a), c) BHF-Pether (1-butanol) compared to BHF-Pether (water) and ligand Pether, d) zoomed IR spectra c).

The mass fraction of the Pether at NPLs (from water and 1-butanol) was determined with TGA. The results are shown in Figure 4.22. BHF-Pether (water) contains 12.5 % Pether, which corresponds to a number of 3 molecules/nm^2. The BHF-Pether (1-butanol) suspension had a concentration below 10 g/l. The mass fraction of the ligand determined with TGA was 20.4 % (see Figure 4.22). The fraction corresponds to the 10 molecules/nm^2. Since the BHF-Pether (1-butanol) were prepared from very stable BHF-DBSA NPLs, a MS analysis was performed to verify that the ligand exchange on the surface of the NPLs was complete. The mass fractions from MS spectra of the TG-MS analysis shown in Figure 4.23 and Figure 4.24 confirm the presence of Pether on the NPLs from both surface modifications. M/z 15, m/z 44, m/z 31, and m/z 45 can be attributed to CH_3^+, CO_2, OCH_3^+, and $CH_2OCH_3^+$, respectively. The most common signals of benzenesulfonic acids at 64 m/z, 65 m/z, 80 m/z, and 91 m/z [155] are absent. However, the signal at 81 m/z, which can be attributed to SO_3H^+, was observed only in the BHF-Pether (1-butanol), not in the BHF-Pether (water). This means that the residues of DBSA are still present in the 1-butanol suspension.

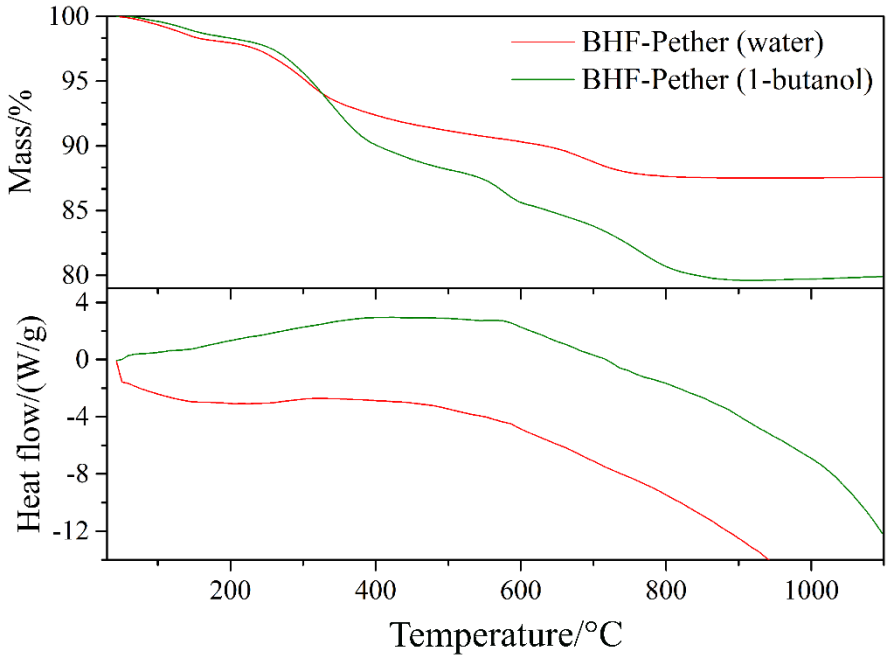

Figure 4.22: Thermal decomposition of BHF-Pether (water) and BHF-Pether (1-butanol): TGA (top) and DSC (bottom).

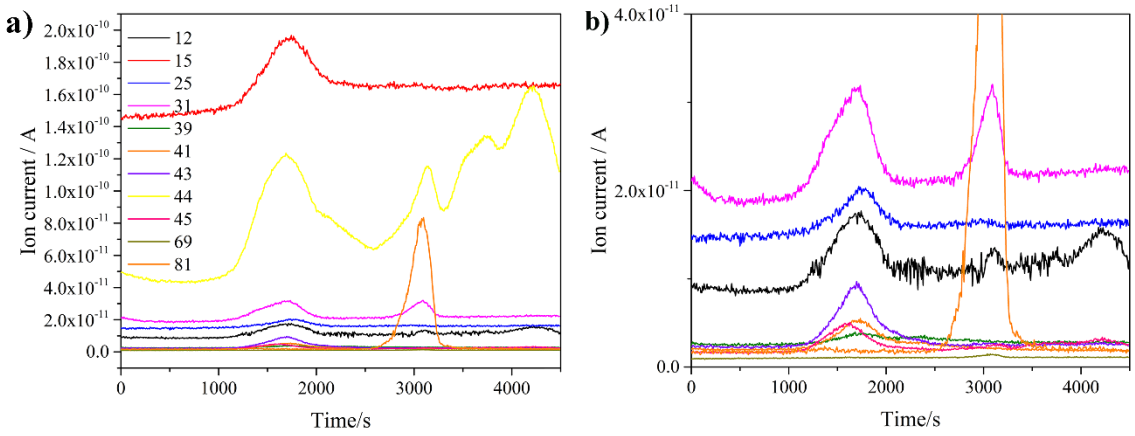

Figure 4.23: a) MS spectra with a corresponding legend, b) zoomed graph a) for the m/z with the lowest signal.

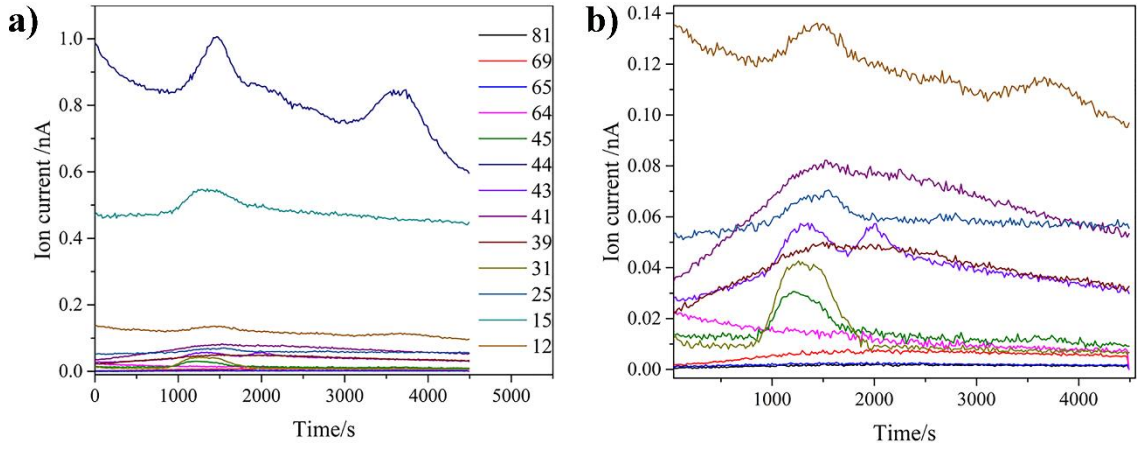

Figure 4.24: a) MS spectra for the thermal decomposition of BHF-Pether (water), b) zoomed graph a) for the m/z with the lowest signal.

The zeta potential of the BHF-Pether NPLs (water) prepared by direct surface modification (see procedure in Chapter 3.2.3) was measured in the pH range between pH 2.5 and pH 10. The BHF-Pether has an isoelectric point between pH 5 and pH 6, similar to the bare BHF-NPLs, as shown in Figure 4.25. The approximately 1 nm long ligand with three ether groups in the ligand chain (see Figure 3.1) binds to the surface of the NPLs with the phosphonic group. The latter is the only functional group that could provide a surface charge, but it can also bind to the surface of the NPLs, leaving the rest of the chain in contact with the solvent. Pether is unlikely to form a double layer. The BHF-Pether NPLs show high colloidal stability in water at very high concentrations required for the formation of the ferromagnetic nematic phase. The BHF-Pether (water) suspension was slowly concentrated in a vial with a magnet in a period of 2–3 weeks. The suspension was then transferred to a capillary where it was further concentrated to obtain the nematic phase. The nematic ferrofluid is shown in Figure 4.26.

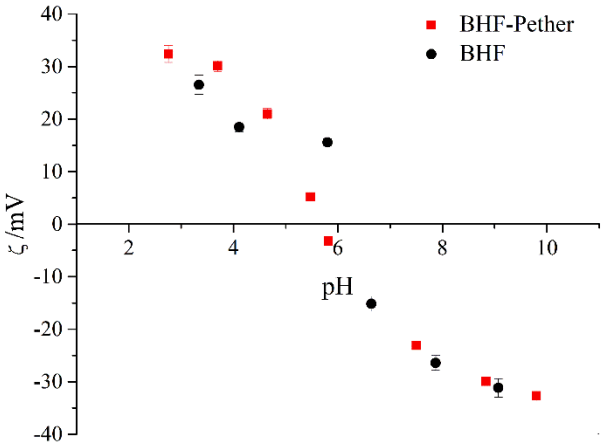

Figure 4.25: Zeta potential values of the modified BHF-Pether NPLs (water) compared to the zeta potential of the bare BHF NPLs.

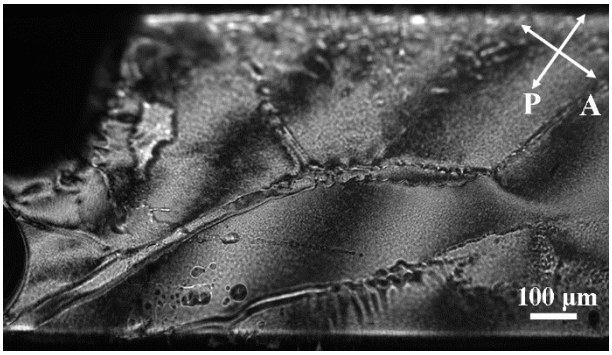

Figure 4.26: POM image of the nematic sample BHF-Pether (water) in zero field.

The zeta potential of BHF-Pether NPLs (1-butanol) was measured in one point. It was (55.7 ± 2.0) mV, which is ~ 20 mV lower than the zeta potential of BHF-DBSA in 1-butanol (see Table 4.4). The positive zeta potential value, as well as the difference in TG-MS between BHF-Pether (water) and BHF-Pether (1-butanol) could be a consequence of DBSA residues in BHF-Pether (1-butanol). To investigate this intriguing behavior in 1-butanol, we transferred the BHF-Pether (water), which had 3 molecules/nm^2, into 1-butanol. The NPLs transferred directly from water to 1-butanol were not colloidally stable. However, when the BHF-Pether (water) NPLs were transferred to a 2 mM 1-butanol solution of Pether, the NPLs remained stable with the zeta potential of (54.2 ± 2.0) mV. The value is in agreement with (55.7 ± 2.0) mV measured in the BHF-Pether (1-butanol). This confirms that a possible DBSA residue is not the (only) reason for the colloidal stability and high zeta potential value of BHF-Pether NPLs in 1-butanol, but also the free Pether in the 1-butanol suspension contributes to the colloidal stability.

Despite the presence of DBSA residues, the behavior of BHF-Pether in 5CB is different from that of BHF-DBSA NPLs. The BHF-Pether NPLs (1-butanol) transferred to 5CB formed a stable suspension (see Figure 4.20) in the isotropic phase with a strong MO response. The zeta potential measurement of the BHF-Pether NPLs in the isotropic 5CB gave an unreliable result. The reason may be a layer of 5CB molecules around the NPLs or some aggregates present, both of which hinder the mobility of the NPLs. The 5CB suspension remained stable after quenching to the nematic phase and centrifugation at 10000 RCF for 5 min to remove aggregates. The concentration of NPLs in the nematic suspension was very low, because some of the NPLs aggregated during the phase transition to the nematic phase. The sample was transferred to a 20-µm LC cell to observe the MO behavior. The nematic sample brightened homogeneously when a minimum field of 3.2 mT was applied, as shown in Figure 4.27. Domain formation was not observed due to the very low concentration of the NPLs in the 5CB, which could not be increased. The 5CB suspension showed a strong MO response in the isotropic phase at 60 °C. Slowly lowering the temperature (in a drop of the suspension) to 40 °C revealed the separation of the isotropic and nematic phases, as shown in Figure 4.28, resulting in the formation of some aggregates that slowly dissolved after increasing the temperature to undergo the transition back to the isotropic phase. After the aggregates dissolved, a strong MO response was again observed. The dissolution of the aggregates is an improvement compared to BHF-DBSA in 5CB. Despite the fact that the BHF-DBSA are stable in the nematic phase of 5CB and form a ferromagnetic nematic phase [3], the aggregates form when the suspension is cooled slowly through the phase transition and they do not dissolve after the sample is heated back to the isotropic phase.

The equivalent diameter distribution of colloidally stable BHF-Pether dispersed in 1-butanol and nematic 5CB is comparable, with an average equivalent diameter of 48 nm

and a standard deviation of 20 nm, as seen in Figure 4.29. However, comparison with the average diameter of the original BHF-DBSA NPLs that were used for the ligand exchange procedure shows that some larger NPLs are lost during the surface modification and centrifugation procedure (see Figure 4.29). Interestingly, in 5CB, some of the very small NPLs seemed to aggregate and were removed by centrifugation.

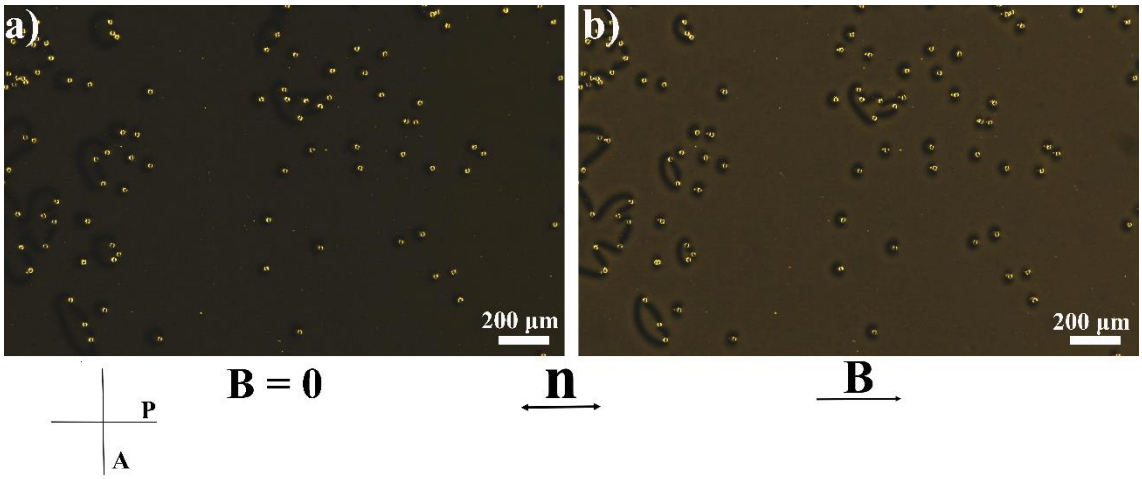

Figure 4.27: POM image of the BHF-Pether NPLs in nematic 5CB in an LC cell between crossed polarizers showing the MO response at an applied magnetic field a) 0 mT and b) 12 mT in parallel to **n**.

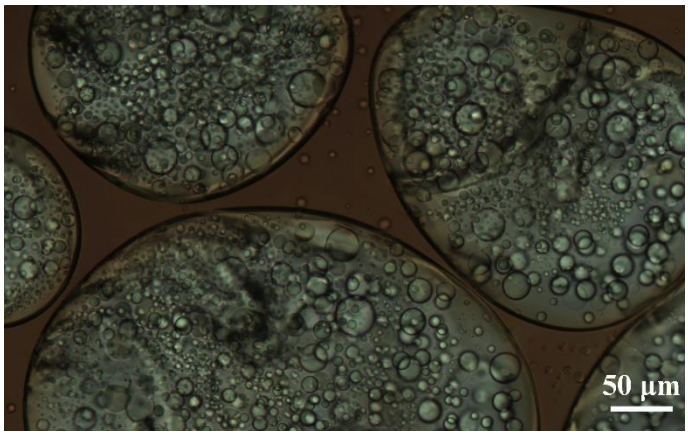

Figure 4.28: Suspension of BHF-Pether in 5CB at 40 °C during slow cooling, with bubbles in the nematic phase surrounded by the isotropic phase (brown).

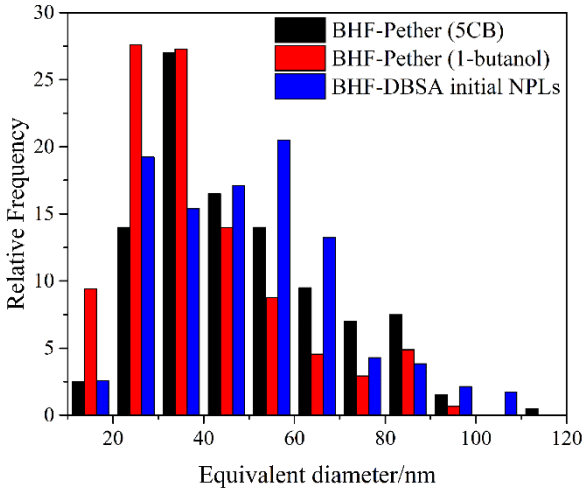

Figure 4.29: The equivalent diameter distribution of colloidally stable BHF-Pether NPLs in 1-butanol and nematic 5CB compared to the BHF-DBSA NPLs.

4.3.1.5 BHF-OA NPLs

OA has a long alkyl tail (18-C) with a cis-double bond in the middle and a carboxylic anchoring functional group (see structure in Figure 3.1). In the IR spectrum of the ligand OA, shown in Figure 4.30, the two sharp bands at 2923 cm^{-1} and 2852 cm^{-1} are assigned to the asymmetric and symmetric CH_2 stretching vibrations, respectively. At 1710 cm^{-1} there is a very strong band ascribed to the C=O stretching and at 1284 cm^{-1} to the C-O stretching vibrations. The bands at 1464 cm^{-1} and 935 cm^{-1} are attributed to the in-plane and out-of-plane O-H stretching vibration, respectively. In the IR spectrum of BHF-OA NPLs in Figure 4.30, the stretching vibrations for CH_2 are shifted from 2923 cm^{-1} and 2852 cm^{-1} to 2920 cm^{-1} and 2851 cm^{-1} [64], [152]. The shift is a consequence of closely packed OA hydrocarbon chains [156]. The strong band at 1710 cm^{-1} observed in the IR spectrum of OA almost disappears, and a broad band at 1535 cm^{-1} appears, which can be attributed to the COO^- stretching vibrations and, as previously suspected [64], [157], [158], is a consequence of carboxylate formation on the surface of the NPLs.

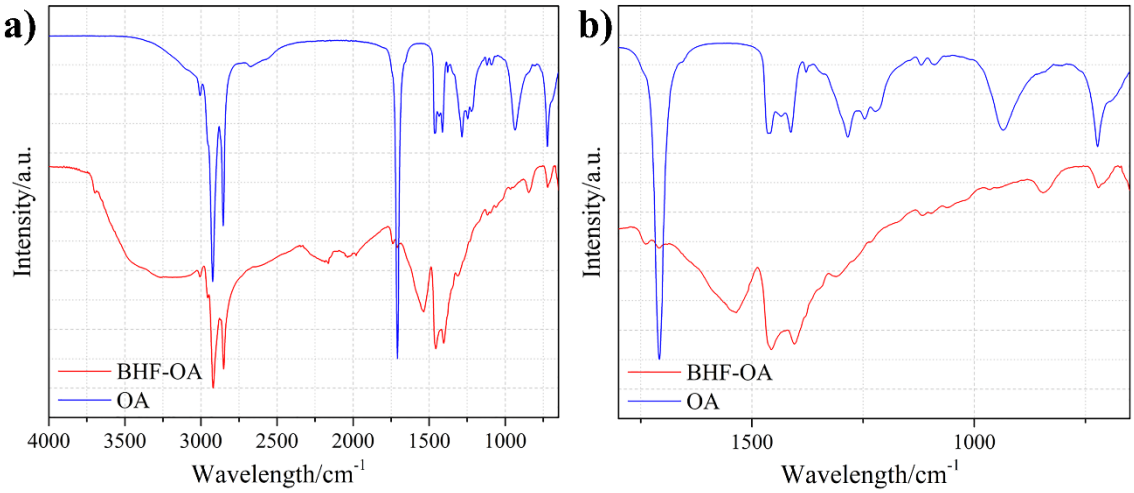

Figure 4.30: a) IR spectra of BHF-OA NPLs and ligand OA and b) zoomed IR spectra of a) to the 1800–650 cm^{-1} region.

OA is a common surfactant used for the preparation of ferrofluids, e.g. [65], [159]. The BHF-OA NPLs form a stable colloidal suspension in chloroform (~ 3 g/L) and 5CB. The colloidal suspension of BHF-OA in the isotropic 5CB shows a very strong MO response and is without visible aggregates, as shown in Figure 4.31a. To observe the behavior during a slow phase transition to the nematic phase, the suspension was cooled to the phase transition temperature, resulting in aggregation of the NPLs and disappearance of the MO response at 39 °C. A mesh-like structure, shown in Figure 4.31b, was observed. It was formed by the NPLs that irreversibly aggregated at the interface between the isotropic and nematic phases. On the other hand, quenching of the isotropic suspension resulted in a stable nematic suspension of the BHF-OA NPLs. The nematic suspension with an initial concentration of ~ 20 g/l was centrifuged at 10000 RCF for 5 min to remove possible aggregates. The centrifuged nematic suspension remained dark brown, so the concentration did not change significantly. The stable nematic suspension was then observed in a 20-µm LC cell. Initially, the sample is polydomain, and ~ 20 mT is needed for the formation of larger domains and π-domain-walls depicted in Figure 4.32. The MO response in the two types of domains reverses when the magnetic field is applied in the opposite direction, as expected in such a system (see Chapter 3.4.5.2) [1].

The colloidally stable BHF-OA in chloroform and nematic 5CB were on average smaller (having an average diameter of 29 nm with a standard deviation of 16 nm and 38 nm with a standard deviation of 15 nm, respectively) than the original bare BHF NPLs (with an average diameter of 47 nm and standard deviation of 21 nm) used for their preparation. The equivalent diameter distributions are shown in Figure 4.33. Also in this case, similar to BHF-Pether, the smallest NPLs (< 20 nm) were not observed in 5CB. The BHF-OA NPLs that formed the stable colloidal suspension in chloroform had a M_s of 30 A m^2/kg (including the ligand OA).

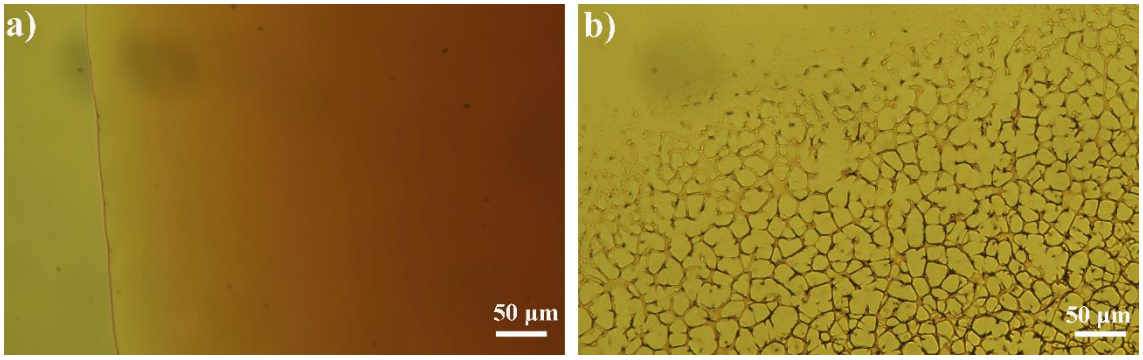

Figure 4.31: a) Isotropic suspension of BHF-OA in 5CB, b) the mesh-like structure formed during the slow phase transition.

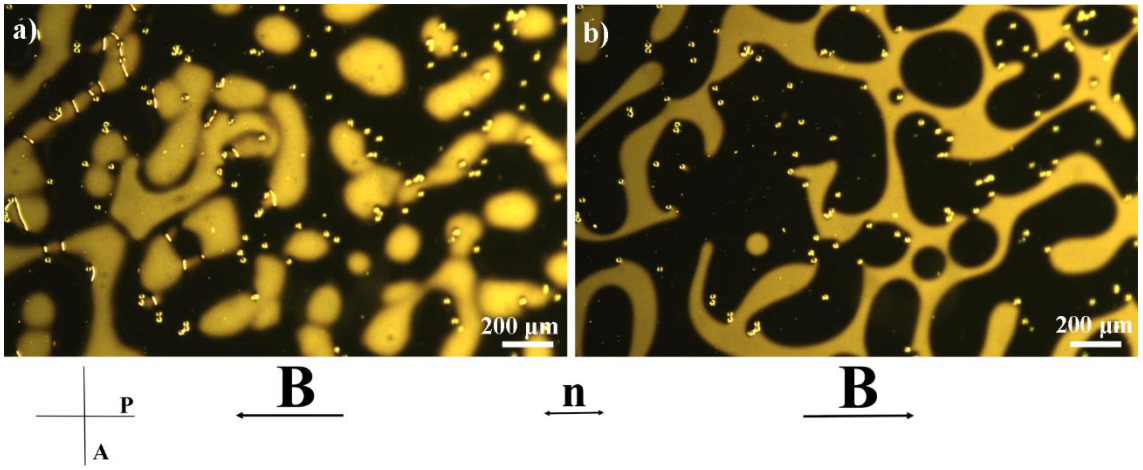

Figure 4.32: POM images of the BHF-OA NPLs in nematic 5CB in an external magnetic field.

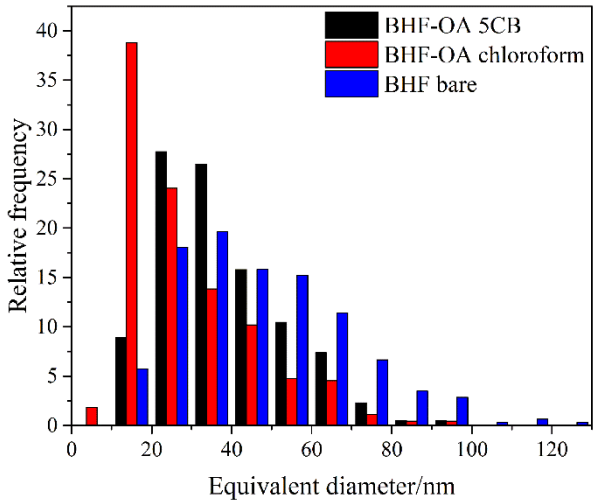

Figure 4.33: The equivalent diameter distribution of the colloidally stable BHP-OA NPLs in chloroform and nematic 5CB compared to the original bare BHF NPLs.

OA is a surfactant with a long alkyl chain that makes the surface of NPLs hydrophobic and is mainly used to stabilize iron oxide nanoparticles in nonpolar solvents. The colloidal stability is attributed to the cis double bond forming a kink in the middle of the molecule, as shown in Figure 4.34a. It has been shown that the kink is essential for the steric colloidal stabilization of iron oxide nanoparticles in nonpolar solvents since the fully saturated stearic acid (18-C alkyl chain) without the kink (see Figure 4.34b) does not provide colloidal stabilization [24]. Tadmor et al. performed a study on the wettability of oleic and stearic acid surfactant layers on mica surfaces in hexadecane [160]. They showed that the OA layer is solvated by hexadecane, most likely due to the kink that hinders the dense assembly of the OA chains. In contrast, the stearic acid layer was only partially wetted (partially solvated), probably due to the closely packed alkyl tails [160]. The stearic acid surfactant layers in contact with hexadecane collapse/coil and the short-ranged adhesive interactions lead to aggregation [160].

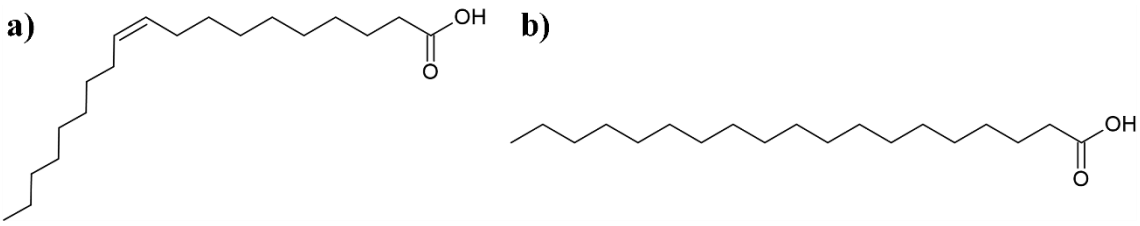

Figure 4.34: Molecular structure of a) oleic acid and b) stearic acid.

A study performed by Gyergyek et al. [65] on OA and RA-modified iron oxide nanoparticles showed a correlation between colloidal stability and solvent dielectric constant. OA-modified nanoparticles remained colloidally stable in solvents with a dielectric constant below 5 (with the exception of THF). In such nonpolar solvents, there is a weak lyophobic attractive interaction between the nanoparticles [161]. In our case, the colloidal stabilization of BHF-OA in chloroform with a dielectric constant of 4.9 [162] is consistent with these results. On the other hand, the colloidal stabilization of BHF-OA in isotropic and nematic 5CB is not, because the dielectric constant of isotropic and nematic 5CB is 10, which is much higher than the dielectric constant of chloroform or even THF (7.4) [163], [164]. The colloidal stability of BHF-OA was better in the isotropic phase than in the nematic phase of 5CB, although the dielectric constant of 5CB is similar in both phases. This difference is probably a consequence of the nematic ordering of the LC molecules and nematic-mediated elastic forces that partially destabilize the suspension of the BHF-OA NPLs (see Chapter 1.4.1.6). The BHF-OA NPLs have a monolayer of OA on the surface when dispersed in nonpolar chloroform, and the colloidal stability of the NPLs is steric. Electrophoretic mobility measurements of the BHF-OA NPLs in isotropic 5CB give a phase-plot diagram close to zero, indicating that the BHF-OA NPLs in 5CB have no charge. The interaction between the isotropic solvent (chloroform) and 5CB and the solvation of the OA surface layer must be of great importance for the colloidal stabilization of the BHF-OA NPLs. The offered explanation for the colloidal stability in 5CB is that the nonpolar alkyl chains of 5CB (see the structure in Figure 1.20) interact with the OA on the surface of the NPLs. As a result, a double layer forms around the NPLs, which helps to sterically stabilize the BHF-OA NPLs despite the higher dielectric constant of 5CB (compared to chloroform). As explained (see Chapters 1.4.1.4–1.4.1.6), to stabilize the NPLs in a nematic medium, we need quadrupole defects (see Figure 1.19 and Figure 1.23) around each NPL to prevent aggregation. In this case, the strong elastic forces during the

slow phase transition cause irreversible aggregation of the NPLs and a defect forms only around an aggregate preventing its dissolution.

4.3.1.6 BHF-RA NPLs

In the IR spectrum of the RA ligand (see structure in Figure 3.1), shown in Figure 4.35a, the bands at 3009 cm^{-1}, 2925 cm^{-1}, and 2855 cm^{-1} are attributed to the asymmetric and symmetric CH_2 stretching [152]. The band at 1708 cm^{-1} is the characteristic stretching vibration for C=O [152] and the band at 1211 cm^{-1} for C-O stretching. The band at 1462 cm^{-1} can be attributed to the O-H vibration [157], [158]. In the IR spectrum of the modified BHF-RA NPLs, there is a broad band at 3200 cm^{-1} attributed to the O-H vibrations. The bands attributed to asymmetric and symmetric CH_2 stretching are shifted to lower frequencies than in RA, i.e., from 2925 cm^{-1} and 2855 cm^{-1} to 2920 cm^{-1} and 2952 cm^{-1}, respectively. The shift is due to the fact that RA hydrocarbon chains are in a closely packed state [156]. The C=O band at 1708 cm^{-1} (RA) was much weaker for the BHF-RA NPLs and shifted to 1736 cm^{-1} (see Figure 4.35b). The shift to a higher frequency could be due to the hydrogen bonding present in the pure RA, which changes the electronegativity of a neighboring atom and the bond length. The new band at 1586 cm^{-1} can be assigned to the asymmetric COO^- and may be a consequence of a carboxylate formation on the NPLs' surface, as previously suggested [64], [157], [158].

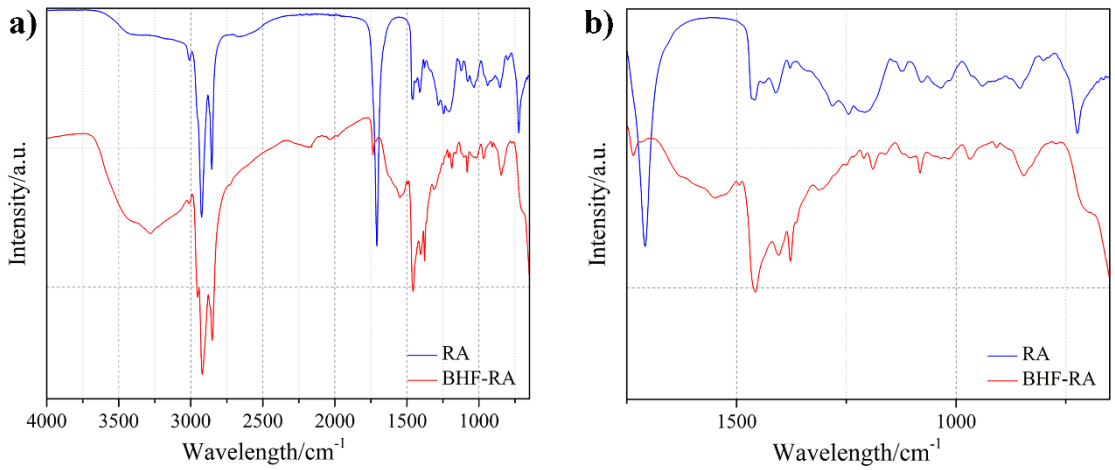

Figure 4.35: a) IR spectra of BHF-RA NPLs and the ligand RA, b) selected bands from the IR spectra between 1750 cm^{-1} and 650 cm^{-1}.

The BHF-RA NPLs were prepared by two different procedures and dispersed in two different solvents as described in Chapter 3.2.3 and shown in the schematic diagram in Figure 4.36. BHF-RA forms stable colloidal suspensions at low concentrations (1–3 g/l) in solvents such as toluene and chloroform (see the synthesis procedures in Chapter 3.2.3). In the isotropic phase of 5CB (see Figure 4.36), the maximum concentration was higher, i.e., ~ 20 g/l and the suspension showed a strong MO response.

We observed a different behavior of the differently prepared BHF-RA NPLs in 5CB, which is shown in the scheme in Figure 4.36. The BHF-RA NPLs (1) (see Figure 4.36) transferred from toluene into 5CB aggregated after a slow phase transition and also after quenching the suspension to the nematic phase. Although the suspension (1) did not remain colloidally stable in the nematic 5CB, the aggregates formed during the phase transition dissolved almost immediately after heating the suspension back to the isotropic phase. The BHF-RA NPLs (2) transferred from chloroform to 5CB remained stable in the nematic

phase after quenching the isotropic 5CB suspension. The initial concentration of the BHF-RA (2) nematic suspension was ~ 20 g/l but decreased slightly after centrifugation and elimination of aggregates. The suspension remained dark brown, indicating that the concentration did not decrease significantly. The nematic sample BHF-RA (2) was transferred to a 20-µm LC cell to observe its behavior under an applied magnetic field. The sample brightened homogeneously when the magnetic field was applied and formed magnetic domains at ~ 12 mT, reversing in the opposite direction of the applied magnetic field, as shown in Figure 4.37a and Figure 4.37b. At ~ 16 mT, the nematic suspension becomes a monodomain. BHF-RA (2) 5CB suspension did not retain colloidal stability after a slow transition to the nematic phase. This was observed upon slow cooling of the isotropic 5CB suspension from the initial ~ 60 °C. Aggregates began to form at 35.7 °C and did not dissolve even after heating the suspension back to the isotropic phase. The equivalent diameter distributions of BHF-RA (2) with an average equivalent diameter 34 nm and a standard deviation of 11 nm and BHF-RA NPLs in nematic 5CB with an average equivalent diameter 33 nm and a standard deviation of 10 nm are comparable, as represented in Figure 4.38, while the average diameter decreases compared to the original bare BHF NPLs with an average diameter 47 nm and a standard deviation of 21 nm. Therefore, only smaller NPLs were stabilized in chloroform and consequently in 5CB. The BHF-RA (2) NPLs that formed the stable colloidal suspension had a M_s of 31 A m^2/kg (including the ligand RA).

The BHF-RA NPLs prepared by both procedures have identical IR spectra and the different behavior in 5CB must be a consequence of the choice of solvent. Similar to BHF-RA, RA-modified iron-oxide nanoparticles have been shown to form stable colloidal suspensions in solvents with dielectric constants up to 9.8 [65], which is close to the dielectric constant of 5CB [163]. The RA forms a monolayer around the NPLs, which enables colloidal stability in nonpolar solvents. The structure of RA is similar to that of OA, and the explanation for the colloidal stability of the NPLs in 5CB can be taken from there. The nonpolar alkyl tails of 5CB order around BHF-RA and form a layer that enables colloidal stabilization in 5CB. Electrophoretic mobility measurements of the BHF-RA NPLs in isotropic 5CB give a phase plot close to zero, indicating that the BHF-RA NPLs in 5CB have no surface charge. This result is expected because the carboxyl groups bind to the surface of the NPLs and the hydrophobic tail is in contact with the solvent enabling colloidal stability. As discussed in Chapters 1.4.1.4–1.4.1.6, quadrupole (nematic-mediated) defects around each NPL are required to stabilize the NPLs in a nematic medium (see Figure 1.19 and Figure 1.23). In the case of BHF-RA (1) NPLs in 5CB, there is a weak anchoring strength and weak elastic forces bring the NPLs together in the nematic phase. Since the elastic forces are weaker than in the case of BHF-RA (2) in chloroform, the aggregates dissolve when the temperature is increased to the isotropic phase. In contrast, in the case of BHF-RA (2) NPLs, the aggregation in 5CB is irreversible due to the stronger elastic forces. Nevertheless, the BHF-RA (2) NPLs were stable in the nematic phase, showing that the stabilization of the NPLs with quadrupolar defects was successful, similar to the case of BHF-OA (see 4.3.1.5).

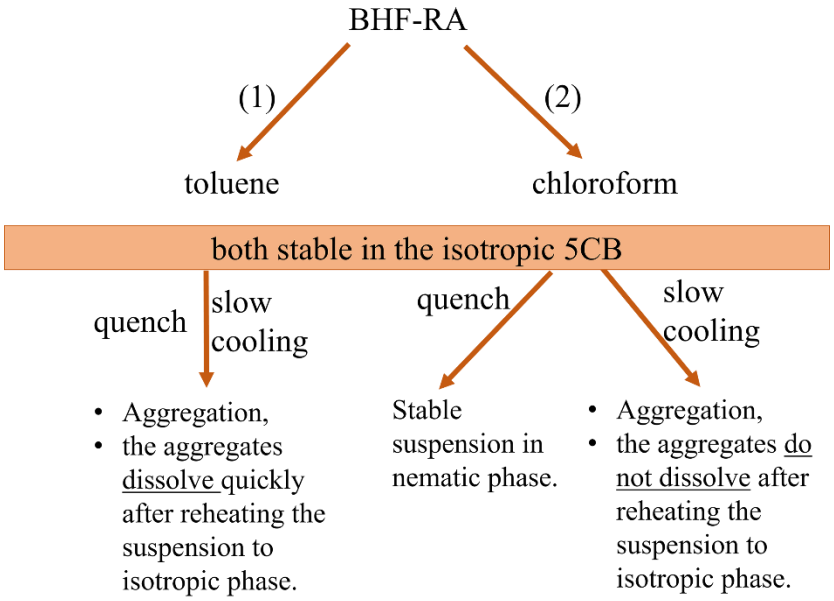

Figure 4.36: Schematic of BHF-RA NPLs behavior in 5CB.

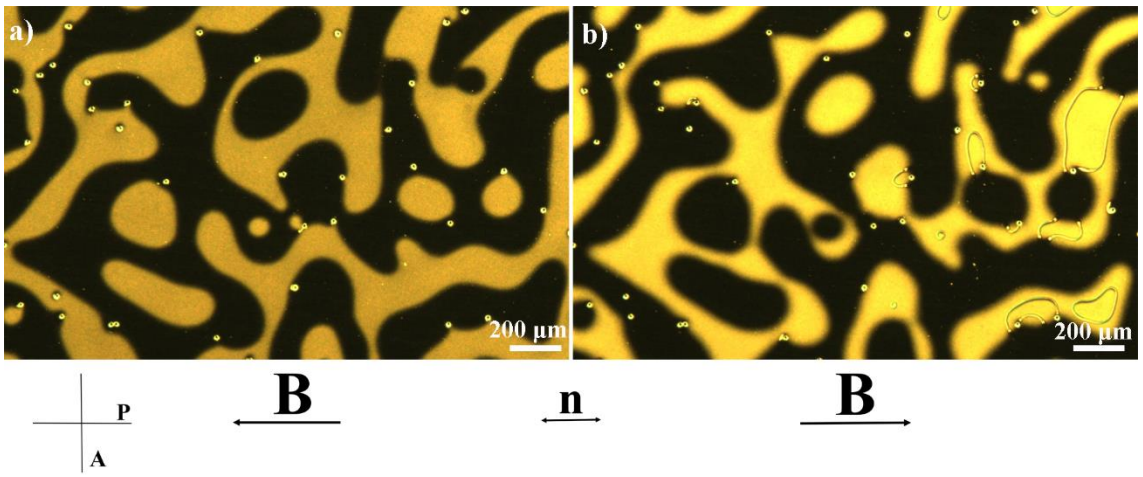

Figure 4.37: POM images of the polydomain nematic BHF-RA (2) sample in 5CB in an external magnetic field.

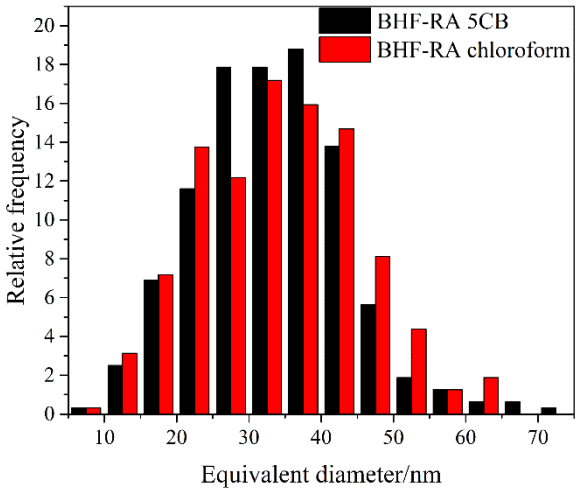

Figure 4.38: The equivalent diameter distribution of colloidally stable BHF-RA NPLs in chloroform and in nematic 5CB.

4.3.2 Combinations of promesogenic and other surface ligands

Surface modification with only one promesogenic ligand (dendrimer or 10POCB) was not a successful approach to stabilize the NPLs in 5CB. The BHF-dendrimer NPLs were stable in toluene at a very low concentration (< 1 g/l), whereas the BHF-10POCB were stable in ethanol. However, the transfer of the NPLs to the isotropic 5CB resulted in aggregation. The negative results prompted us to change the direction. Therefore, we investigated surface modification with different combinations of promesogenic and other surface ligands.

4.3.2.1 BHF-RA-dendrimer NPLs

In the IR spectra of RA and dendrimer, shown in Figure 4.39, we find that the typical C=O band for the carboxyl group in RA at 1708 cm^{-1} is very close to the C=O band for vibrations of several ester groups in the dendrimer (1718 cm^{-1}). The C=O band is present in the case of BHF-RA-dendrimer NPLs at 1709 cm^{-1}. There is also a difference in the region between 1600 cm^{-1} and 1400 cm^{-1}, where a broad absorption band is present that is specific for the carboxyl group. An indication that the dendrimer is bound to the surface is the changes in the 1100–1000 cm^{-1} region, which correspond to the free and binding forms of phosphonic acids. Between 1200 cm^{-1} and 900 cm^{-1} there is a broad band, typical of the P-O vibrations. Some IR spectral bands of the BHF-RA-dendrimer NPLs overlap with the bands of BHF-RA NPLs, indicating that the ligand exchange may not be complete and a mixture of two ligands is present at the surface of the NPLs. Only partial ligand exchange is evidenced by observing the behavior of the 5CB suspension, where there is a clear difference in the behavior of the BHF-dendrimer, BHF-RA and BHF-RA-dendrimer samples.

The BHF-RA-dendrimer NPLs formed a stable colloidal suspension in toluene (~ 1 g/l) and isotropic 5CB with a strong MO response. However, the 5CB suspension destabilized after the transition to the nematic phase (slow and quenching). Aggregates formed during the phase transition dissolved after reheating the suspension back to the isotropic phase. The zeta potential of the BHF-RA-dendrimer NPLs in the isotropic 5CB is close to zero. The stability of the BHF-RA-dendrimer 5CB suspension is improved compared to BHF-dendrimer suspension. The latter is unstable in the isotropic and in the nematic phases of

5CB. This suggests that the combination of the dendrimer with linear molecules on the NPLs surface (in this case RA) provides sufficient space between the tails of the dendrimer for the 5CB molecules to intercalate and enable colloidal stability, similar to what has been shown for spherical magnetic particles [71]. Moreover, the favorable interactions between the RA and 5CB molecules that enable colloidal stability of BHF-RA NPLs in nematic 5CB (see Chapter 4.3.1.6) improve the colloidal stability of the BHF-RA-dendrimer 5CB suspension in comparison to the BHF-dendrimer 5CB suspension.

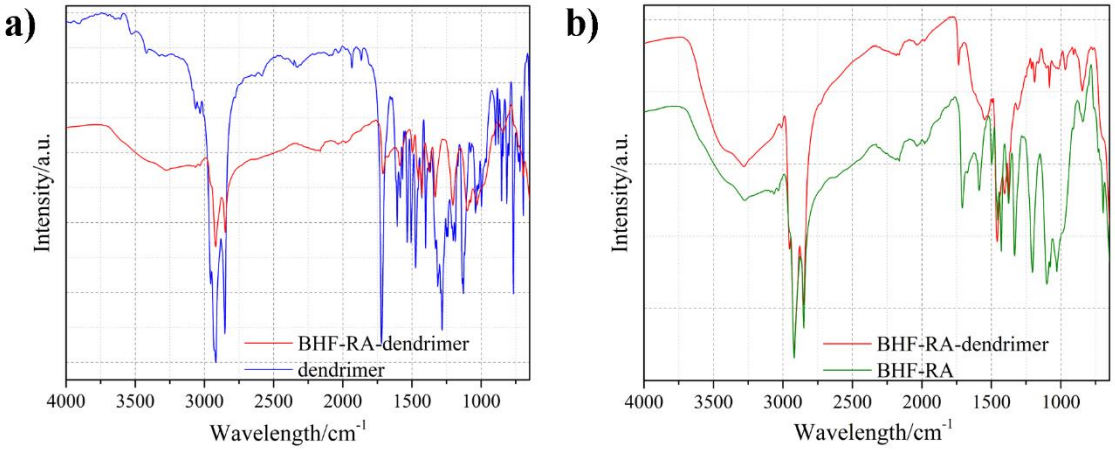

Figure 4.39: a) IR spectra of the ligand dendrimer and BHF-RA-dendrimer, b) IR spectra of the BHF-RA-dendrimer and BHF-RA NPLs.

4.3.2.2 BHF-HPA-dendrimer NPLs

In the IR spectrum of HPA, shown in Figure 4.40, bands at 2930 cm^{-1}, 2857 cm^{-1}, and 1462 cm^{-1} are assigned to asymmetric and symmetric C-H stretching and bending vibrations, respectively. The bands for the phosphonic group are at 1235 cm^{-1} (P-O stretch), 1104 cm^{-1} and 1071 cm^{-1} (PO_3 stretch). Very strong bands between 998–929 cm^{-1} and 770 cm^{-1} are assigned to P-O-H and P-C. In the IR-spectrum of the BHF-HPA-dendrimer NPLs, the HPA bands at 1235 cm^{-1} and 1104 cm^{-1} and the dendrimer band at 1282 cm^{-1} disappear. The bands combine to form a broad band at 1030 cm^{-1}, which extends approximately between 1030 cm^{-1} and 907 cm^{-1}. The differences in the spectra of the pure ligands and the modified BHF-HPA-dendrimer NPLs indicate that phosphonic groups are bound to the surface of the NPLs. Since HPA contains similar stretching vibrations (for the alkyl chain and the phosphonic group) as the dendrimer, it is difficult to distinguish between the two ligands in the spectrum of the BHF-HPA-dendrimer NPLs. The actual molar ratio between the HPA and the dendrimer on the NPLs may differ from the initial ratio (1:5) used in the surface modification procedure (see Chapter 3.2.3) due to the significant size differences and with this related mobility of the molecules [71]. Prodanov et al. [71] showed that the actual molar ratio between HPA and dendrimer for surface modification of very small (< 10 nm) spherical $CoFe_2O_4$ nanoparticles was close to the ratio used, i.e., instead of 1:4 it was 1:2.8. Nevertheless, they obtained colloidally stable NLC suspensions with a dendrimer-HPA surface modification.

In our case, the as-modified NPLs formed a stable suspension only in the isotropic phase of 5CB with a strong MO response and no visible aggregates. Cooling of the BHF-HPA-dendrimer 5CB isotropic suspension to the nematic phase resulted in aggregation. The aggregates formed during the phase transition dissolved after reheating the suspension back to the isotropic phase.

The zeta potential of the BHF-HPA-dendrimer NPLs in isotropic 5CB is close to zero, and the modified NPLs have no surface charge. This was expected since HPA and dendrimer do not possess any sources of charge other than the anchoring phosphonic functional groups. Thus, we can also exclude the possibility of the formation of a double layer.

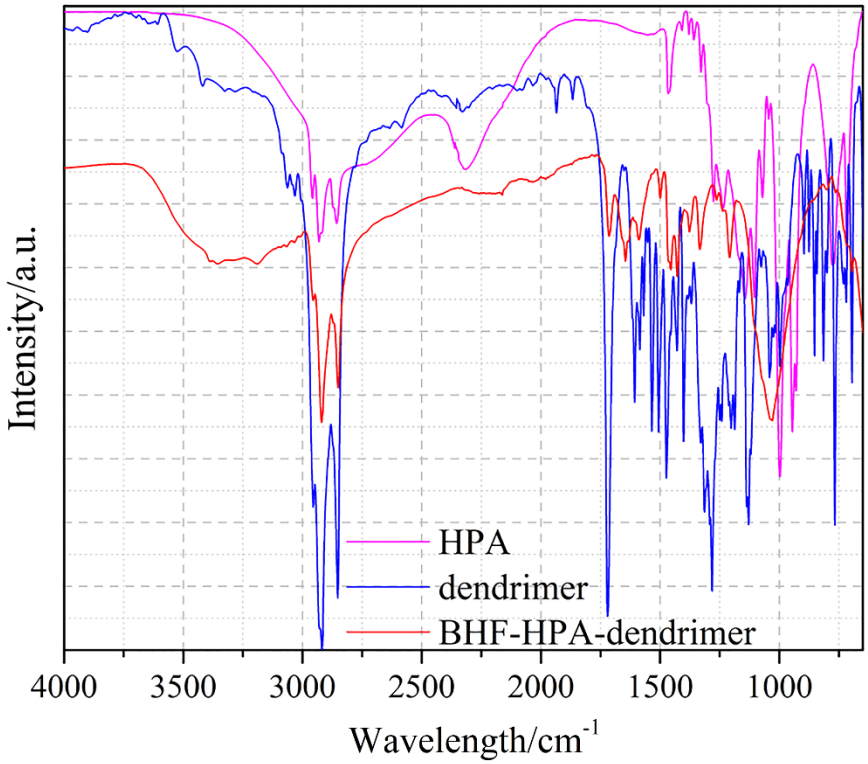

Figure 4.40: IR spectra of ligands HPA, dendrimer and BHF-HPA-dendrimer NPLs.

4.3.2.3 BHF-ODPA-dendrimer NPLs

ODPA is a molecule with a phosphonic group and a long alkyl chain (see structure in Figure 3.1). The IR spectrum of ODPA, shown in Figure 4.41, has CH_3 and CH_2 vibrations at 2957 cm^{-1}, 2916 cm^{-1}, and 2850 cm^{-1}. The band at 1472 cm^{-1} can be assigned to CH, 1213 cm^{-1} P=O, 1075 cm^{-1} and 930 cm^{-1} to P-O, 947 cm^{-1} to P-O-H and 782 cm^{-1} and 715 cm^{-1} to P-C and C-H vibrations [73], [76]. In the IR spectrum of the BHF-ODPA-dendrimer NPLs, there are bands between 1713 cm^{-1} and 1333 cm^{-1} that can be attributed to the dendrimer. At the same time, the band at 1213 cm^{-1} remains at the same wavelength as in ODPA, but could also be a result of shifted bands of the dendrimer. Since both the dendrimer and ODPA contain P=O bonds, the band cannot be assigned to either ligand. The very broad band at 1039 cm^{-1} is a consequence of the bound phosphonic group to the BHF surface [151], [152], [165].

Similar to BHF-RA-dendrimer NPLs and BHF-HPA-dendrimer NPLs, the difference in surface modification affected the NPLs behavior in 5CB compared to the NPLs modified with only one of these ligands. BHF-ODPA-dendrimer NPLs in isotropic 5CB form a stable suspension that aggregates upon phase transition to the nematic phase. The measured zeta potential of the modified NPLs is close to zero. As in the previous two cases (BHF-RA-dendrimer and BHF-HPA-dendrimer), the dilution of the dendrimer layer on the surface

of the NPLs contributes to the colloidal stabilization of the NPLs in toluene (~ 1 g/l) and in isotropic 5CB.

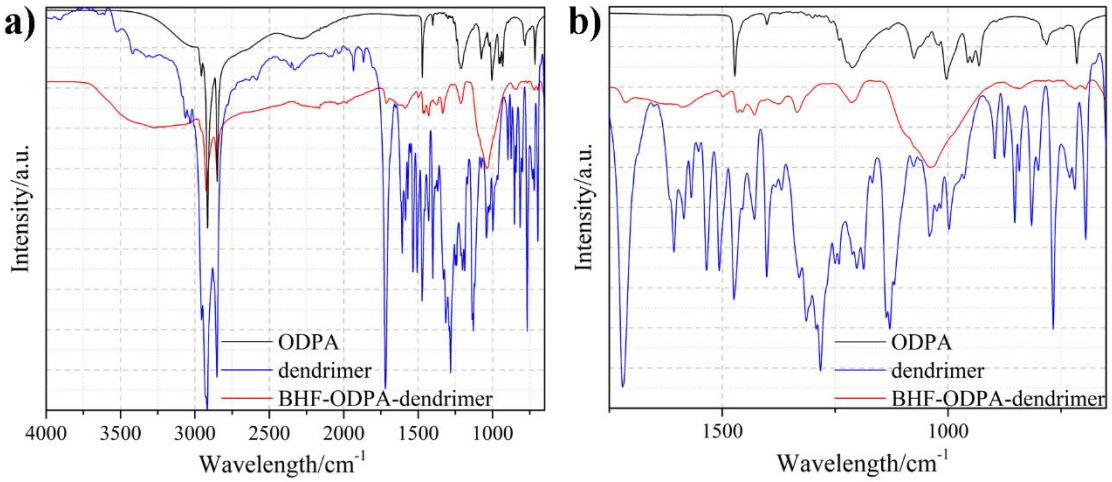

Figure 4.41: a) IR spectra of pure ligands and BHF-ODPA-dendrimer NPLs, b) zoomed IR spectra to 1750–650 cm^{-1}.

4.3.2.4 BHF-10POCB-AL NPLs

The surface modification of BHF-10POCB-AL NPLs can be demonstrated by comparing the IR spectra of both ligands, namely 10POCB and AL to the surface-modified NPLs. The IR spectra are shown in Figure 4.42. The IR spectrum of 10POCB shows bands for aromatic and aliphatic CH_3 and CH_2 stretching vibrations at 2936 cm^{-1}, 2920 cm^{-1} (aromatic) and 2851 cm^{-1} as well as a band for CN at 2236 cm^{-1}, which is located in the mesogenic part of the ligand (see Figure 4.42) [73], [166]. The band at 1521 cm^{-1} is attributed to the C-C stretching vibrations in the aromatic ring and the bands between 835 cm^{-1} and 734 cm^{-1} are assigned to the out-of-plane C-H bending vibrations in the aromatic rings [152].

AL contains three different functional groups, namely two phosphonic groups, one hydroxyl group, and one amino group (see the AL structure in Figure 3.1). The N-H stretching vibrations result in a band at 3477 cm^{-1} and N-H bending vibrations at 1643 cm^{-1} [167]. The bands between 1250 cm^{-1} and 750 cm^{-1} can be assigned to vibrations in the two phosphonic groups (see previous explanations of IR-spectra) [152].

The phosphonic anchoring groups of both ligands bind to the surface of the NPLs. The result is a broadened band between 1195 cm^{-1} and 880 cm^{-1} [152]. The binding ratio between 10POCB and AL is not necessarily the same as used in the modification procedure (see Chapter 3.2.3). The bands such as 1521 cm^{-1} (aromatic ring) in 10POCB and 1643 cm^{-1} (N-H) in AL are also present in the IR spectrum of the modified NPLs. The presence of the bands attributable to both ligands indicates that the surface modification was successfully performed with a combination of both ligands.

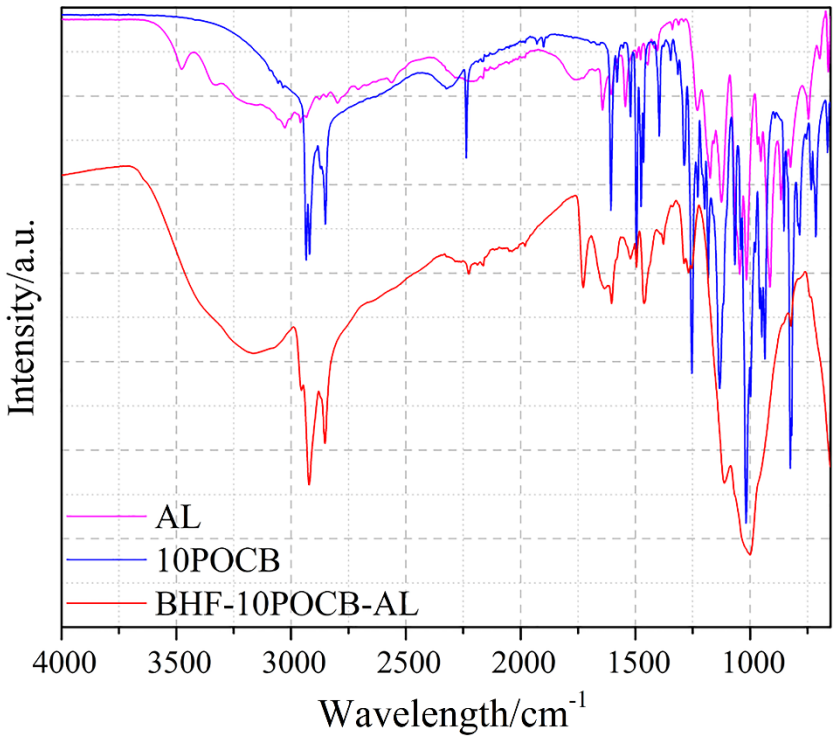

Figure 4.42: IR spectra of the pure ligands and BHF-10POCB-AL NPLs.

The zeta potential of the BHF-10POCB-AL 1:1 NPLs in ethanol was (22.5 ± 1.0) mV and in THF (–22.1 ± 0.4) mV, while for the BHF-10POCB-AL 3:1 NPLs, it was (–23.0 ± 0.5) mV in ethanol and (37.6 ± 0.8) mV in THF. The large excess of 10POCB used in the surface modification (3:1) may lead to partial double-layer formation caused by the π-π stacking aromatic interactions (weakly electrostatic) of the biphenyls in the mesogenic part of the 10POCB molecules. On one side of the 10POCB molecule, there is a nitrile group as an electron acceptor, and on the other side, an oxygen directly bound to the ring is an electron donor group. The attractive interactions between the mesogenic moieties can lead to a realignment of the free 10POCB molecules, with the phosphonic group facing outward and inducing a negative surface charge on the NPLs. Since the zeta potential is relatively low for a functional group such as the phosphonic group, we assume that the second layer is very dilute. The positive zeta potential of the BHF-10POCB-AL 1:1 NPLs in ethanol can be attributed to the amino group of the AL ligand.

The most obvious evidence that the system is different from that with pure 10POCB is the behavior of the NPLs in the 5CB, because the NPLs modified with only 10POCB were not colloidally stable in the isotropic 5CB. The schematic in Figure 4.43 shows the behavior of the BHF-10POCB-AL NPLs in 5CB. BHF-10POCB-AL 3:1 NPLs (THF) were colloidally stable in the isotropic 5CB and showed a strong MO response. Cooling of the LC suspension to the phase transition resulted in aggregation of the NPLs into layered structures that did not dissolve after the nematic-isotropic phase transition. In contrast, in the case of BHF-10POCB-AL 3:1 NPLs (ethanol), a different behavior was observed despite the same functionalization procedure. These NPLs already formed aggregates in the isotropic 5CB (see Figure 4.43).

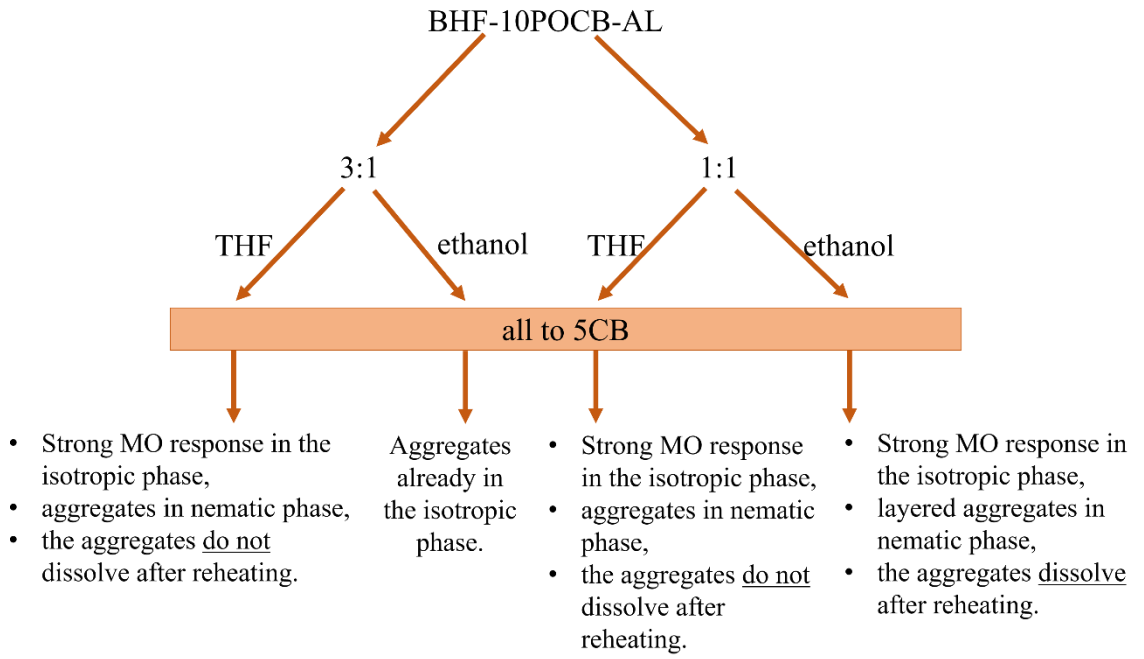

Figure 4.43: Schematic of the different versions of BHF-10POCB-AL NPLs suspensions and the results on their colloidal stability in 5CB.

The BHF-10POCB-AL 1:1 (THF) and the BHF-10POCB-AL 1:1 (ethanol) 5CB suspensions were colloidally stable in the isotropic phase and showed a strong MO response. Quenching and slow transition into the nematic phase caused aggregation. In the case of BHF-10POCB-AL 1:1 (ethanol), the aggregation is reversible and the MO response is regained. In contrast, the aggregates of BHF-10POCB-AL 1:1 (THF) do not dissolve (see Figure 4.43). In the case of BHF-10POCB-AL 1:1 (ethanol), a very slow decrease in temperature to 42 °C leads to the formation of droplets in the observed sample, similar as shown in Figure 4.44, which exhibit MO response. In the range of 40–42 °C we observe a very strong MO response, typical of a ferromagnetic phase. At 31 °C, the MO response is still present for a few minutes, then aggregates begin to form. The aggregates dissolve with increasing temperature and can be separated with an external magnetic field. Similar behavior during slow cooling through the phase transition was observed for BHF-10POCB-AL 1:1 (THF). At ~ 50 °C, we observed a phase resembling a ferromagnetic nematic phase with MO response (see Figure 4.44). The BHF-10POCB-AL 1:1 (THF) NPLs aggregate during the phase transition, and the aggregates do not dissolve after reheating the suspension (see Figure 4.43). The intermediate phase occurs in the temperature range above the phase transition where the elastic forces are not strong enough to cause aggregation.

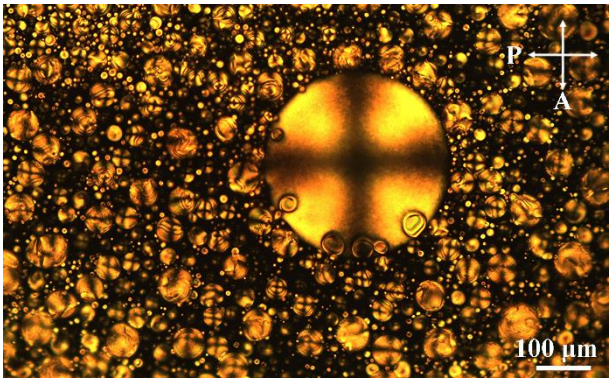

Figure 4.44: Droplets of the ferromagnetic phase in the sample BHF-10POCB-AL 1:1 NPLs (THF) in 5CB.

4.3.2.5 BHF-PSA-10POCB NPLs

BHF-PSA-10POCB NPLs were prepared with a combination of both ligands, i.e., PSA and 10POCB, on the surface of the NPLs. The IR spectrum of BHF-PSA-10POCB NPLs, shown in Figure 4.45, has very weak bands that cannot be assigned to only one of the ligands used. Therefore, we cannot conclude from the IR spectrum whether both ligands have bound to the surface.

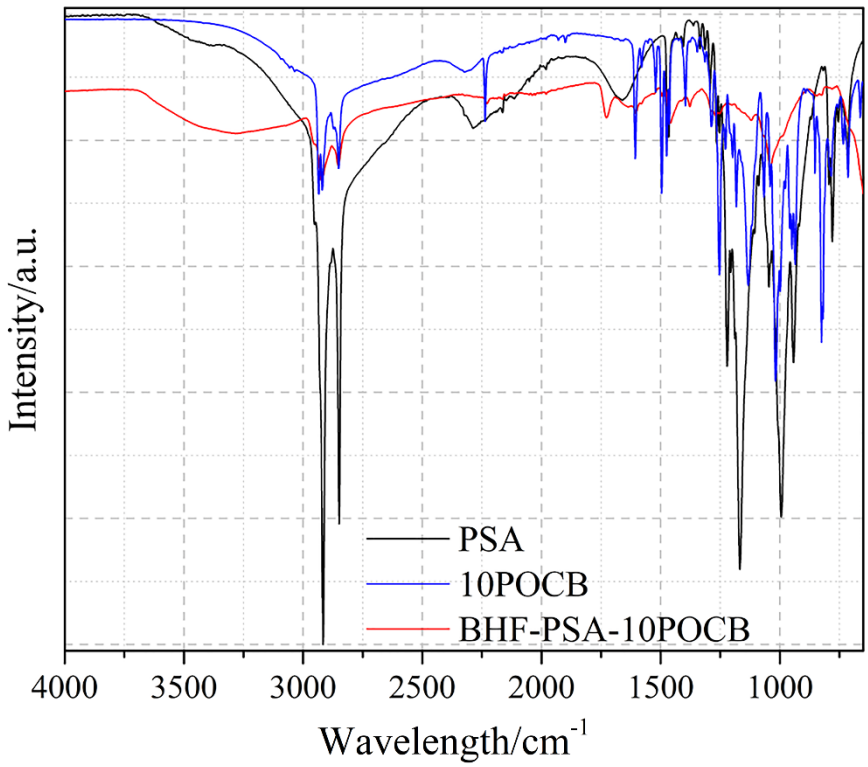

Figure 4.45: IR spectra of pure ligands and BHF-PSA-10POCB NPLs.

However, the behavior in 5CB showed that the surface of the NPLs was modified with a combination of PSA and 10POCB. The NPLs modified with only one of the surfactants, namely BHF-PSA and BHF-10POCB NPLs, did not form a colloidally stable suspension

in 5CB. However, the BHF-PSA-10POCB NPLs form a stable colloidal suspension in isotropic 5CB. At 60 °C, the suspension shows a strong MO response. When we slowly lower the temperature to 40 °C, we observe droplets of a ferromagnetic liquid between crossed polarizers, as shown in Figure 4.46. The liquid had a very strong MO response. Approaching the isotropic-nematic transition (i.e., > 35 °C), the LC near the surface of the glass, which cools first, appeared to be already in the nematic phase and formed some gellish aggregates. The phase transition could be slowed down with a strong external magnetic field. The aggregates formed during the transition dissolved after the suspension was reheated, and the suspension resumed its original MO response. The longer we stayed in the nematic phase before reheating, the larger the aggregates were and the slower they dissolved.

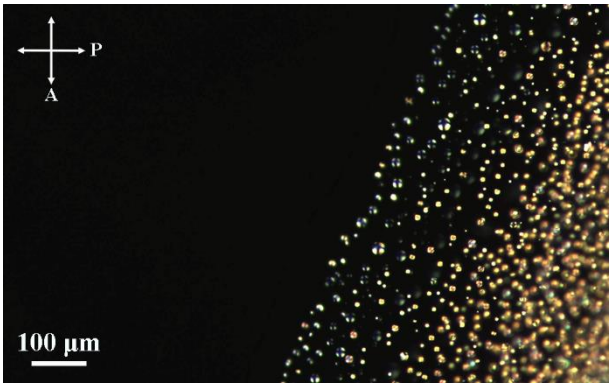

Figure 4.46: The ferromagnetic MO-responsive droplets of BHF-PSA-10POCB 5CB suspension near the phase transition (at 40 °C).

4.3.2.6 Discussion

Despite a promising study [79] on the stabilization of NLC suspensions made of spherical nanoparticles modified with dendrimer and HPA, this system is not suitable colloidal stabilization of plate-shaped ferrimagnetic NPLs. The basal surfaces of the NPLs are flat, which leads to close packing of the mesogenic parts of the dendrimer and consequently suppresses the flexibility of the molecule, although the dendrimer layer is diluted with shorter HPA molecules, as shown in Figure 4.47. The same result was observed in all cases where one of the promesogenic ligands (dendrimer or 10POCB) was used in combination with other ligands added to dilute the surface layer of the promesogenic ligand and/or provide a surface charge (BHF-RA-dendrimer, BHF-HPA-dendrimer, BHF-ODPA-dendrimer, BHF-10POCB-AL, and BHF-PSA-10POCB NPLs, see Table 4.8). Our explanation is partially confirmed by the observation that neither BHF-dendrimer NPLs nor BHF-10POCB NPLs were colloidally stable in isotropic 5CB, but the combinations of dendrimer or 10POCB with other ligands stabilized the isotropic 5CB suspensions. For the colloidal stability of smaller nanoparticles in an NLC, it is important that the surface coverage and the arrangement of the surface ligands allow the penetration of the LC molecules into the interstices of the bound ligand layer [71], [72], [79], which reduces the deformation of **n** around the NPLs in the nematic phase and consequently enables colloidal stability. This has been demonstrated for spherical and needle-shaped particles [71], [72], [79]. Both types of particles have a curved surface that allows the bound surface ligands to stretch in the surrounding space and allow the penetration of the LC molecules. However, Qi et al. [168] observed that spherical Au nanoparticles with diameters less than 2 nm covered with promesogenic ligands tend to aggregate in an LC host, in contrast to Au

nanoparticles covered with alkyl ligands of different lengths. Surface modification with promesogenic ligands may promote self-attraction due to π-π stacking or dipole-dipole interactions leading to aggregation [168]. On the other hand, Appel et al. [169] functionalized $CoFe_2O_4$ and γ-Fe_2O_3 nanoparticles (with an average diameter of less than 3 nm) with ligands similar to 10POCB. The difference in the structure of the ligand used compared to 10POCB is only in the length of the alkyl chain (alkyl chain C_6, C_7, C_{15}) and the anchoring group (carboxyl). The nanoparticles formed stable suspensions in the isotropic and nematic phases of 5CB. They observed that longer spacers in the promesogenic ligand provided flexibility and favorable arrangement with respect to the NLC, leading to colloidal stability [169]. Buluy et al. reported results on the surface modification of needle-shaped nanoparticles (with an average diameter of 25 nm and length of 175 nm). Functionalization with a 10POCB-like promesogenic linear ligand showed slightly better stability in an NLC than functionalization with dendrimer [72]. Spherical nanoparticles and needle-shaped nanoparticles have a round surface that enables flexibility of the ligand chain (especially the dendrimer) resulting in colloidal stability, while the flat surface of the NPLs with densely packed 10POCB (see Figure 4.47c) does not allow sufficient flexibility of the 10POCB molecules and also promotes the attractive π-π stacking interactions between the biphenyls in PMUs. The π-π stacking interactions may cause the ligand chains to collapse and not allow favorable arrangement of the LC molecules and consequently colloidal stability. A combination of 10POCB with shorter, linear ligands provides stability of the NPLs in the isotropic 5CB, but this type of coverage does not provide stability in the NLC, suggesting that nematic-mediated elastic forces are the reason for aggregation.

Another reason for the observed aggregation of BHF NPLs in nematic 5CB is the shape and size of the NPLs and also nematic elastic forces. After evaluating our results and comparing them with other studies on colloidal stabilization of nanoparticles in LCs [79], [101], [169], [170], it is clear that larger particles (> 10 nm) are more challenging to stabilize in the nematic hosts. Smaller nanoparticles can be stabilized in an NLC if we have small distortions of **n** and the nematic-mediated elastic forces do not cause aggregation (see Chapter 1.4.1.6). However, to stabilize larger nanoparticles, quadrupole defects are needed because the field around a quadrupole decreases rapidly with distance and two nanoparticles that are not in close mutual vicinity do not interact. The quadrupolar nematic-mediated interaction is preferable to counteract the attractive dipole-dipole interactions along the direction of the magnetic moments of the NPLs [3]. Strong anchoring and strong elastic forces in the case of larger NPLs (> 10 nm) (see Chapter 1.4.1), which are required for stability in NLC, also lead to the observed irreversible aggregation (in the case of BHF-OA and BHF-RA, see Table 4.8). In our case, the elastic forces between the NPLs modified with promesogenic ligands are too weak to stabilize the NPLs in the nematic 5CB, and at the same time sufficiently weak for the aggregates formed during the phase transition to dissolve (see Chapter 4.3.2).

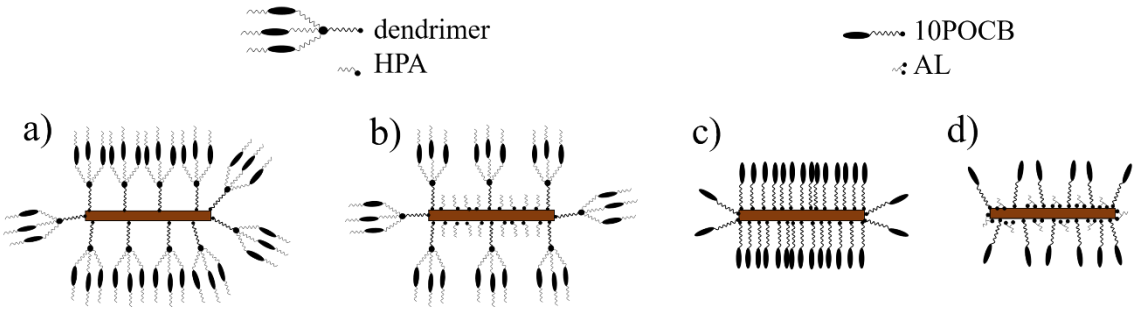

Figure 4.47: Schematic representation of ligand alignment on the NPLs: a) dendrimer, b) HPA and dendrimer, c) 10POCB, and d) 10POCB and AL.

Our results show the importance of the ratio between promesogenic 10POCB and AL, but also the importance of the isotropic solvent from which the NPLs were transferred to 5CB. Different solvents solvate the surface of the modified NPLs differently. An unsuitable solvent that does not ensure good solvation of the NPLs may destabilize the NPLs already in the isotropic solvent from which the NPLs are transferred to an LC. Consequently, stability cannot be restored in the nematic LC. Better results are obtained for BHF-10POCB-AL 1:1 NPLs (as well as for BHF-PSA-10POCB NPLs) than for BHF-10POCB-AL 3:1 NPLs 5CB suspensions, since in the first case we observe a ferromagnetic nematic intermediate phase. In the case of BHF-10POCB-AL NPLs (ethanol) with positive surface charge, the aggregation was reversible. The observed intermediate phases (see Chapters 4.3.2.4 and 4.3.2.5) in the 5CB suspensions need subsequent investigation and are of interest for further research to stabilize BHF-promesogenic-ligand NPLs in an NLC.

Based on our results, the formation of a stable suspension of BHF NPLs in the nematic phase of an LC host is still a major challenge due to the combination of attractive dipole-dipole magnetic interactions and the elastic forces between the NPLs in the NLC. The ligands must be long enough to be flexible and to sterically stabilize the suspensions of the magnetic NPLs. On the other hand, if the ligands are too long, they will resemble less the structure of an LC, which prevents stabilization due to the larger exclusion volume [72], [101]. In the case of ferrimagnetic BHF NPLs, steric repulsion is sufficient for sufficiently small NPLs (< 35 nm), as shown in the case of BHF-OA and BHF-RA NPLs (see Chapters 4.3.1.5, 4.3.1.6 and Table 4.8). Additional electrostatic interactions caused by some ligands such as DBSA provide repulsion at shorter distances between NPLs and ensure colloidal stability of suspensions prepared from larger NPLs [3], [55].

4.3.3 Summary

Table 4.8: A summary of the results presented in Chapters 4.3.1 and 4.3.2.

Sample	Solvent	Stability in isotropic 5CB	Stability in nematic 5CB	Reversibility of aggregation
BHF-DBSA	water	/	/	/
BHF-PHDA	water	/	/	/
BHF-PSA	water	/	/	/
	1-butanol	no	no	/
BHF-Pether	water	/	/	/
	1-butanol	yes	yes	yes
BHF-OA	chloroform	yes	yes	no
BHF-RA	toluene (1)	yes	no	yes
	chloroform (2)	yes	yes	no
BHF-RA-dendrimer	toluene	yes	no	yes
BHF-HPA-dendrimer	toluene	yes	no	yes
BHF-ODPA-dendrimer	toluene	yes	no	yes
BHF-10POCB-AL 1:1	THF	yes	no	no
	ethanol	yes	no	yes
BHF-10POCB-AL 3:1	THF	yes	no	no
	ethanol	no	no	/

Chapter 5

Conclusions

The dissertation reveals the mechanisms for colloidal stabilization of BHF NPLs in various solvents. An example of colloidal systems with stability at very high concentrations are alcohol suspensions of the NPLs modified with DBSA. Such alcohol suspensions allow the preparation of a ferromagnetic nematic ferrofluid – a liquid magnet. We have shown that electrostatic interactions are crucial for the stability of alcohol suspensions. The electrostatic interactions are affected by the concentration of DBSA in the suspension. The dissolved and adsorbed DBSA are in equilibrium. The concentration of adsorbed DBSA determines the surface charge and the concentration of dissolved DBSA determines the ionic strength of the suspension. The dielectric constant affects the dissolution and dissociation degree of DBSA, as well as the zeta potential and Debye screening length. By evaluating the parameters affecting the total interaction energy in alcohol suspensions of DBSA-modified NPLs (surface charge, ionic strength, Debye screening length), we concluded that 1-butanol is the best among the studied alcohols for preparing a ferromagnetic nematic ferrofluid. Although 1-butanol suspensions have a slightly lower Debye length (compared to other alcohols), the highest colloidal stability can be attributed to an optimal combination of the relatively high surface charge of the NPLs and low dielectric constant of the alcohol. The calculated total interaction energy in the system revealed a shallow secondary minimum at a few tens of nm. The minimum is responsible for the nematic ordering of the NPLs. However, when it is too deep, it can lead to reversible aggregation or, in the case of dense suspensions, gelation.

The study of the effects of various parameters (equivalent diameter distribution of NPLs, strength of magnetic and electrostatic interaction) on the phase behavior of the 1-butanol suspensions of BHF NPLs revealed that:

1. The NPLs with on-average larger average equivalent diameter order to ferromagnetic nematic phase at a lower volume fraction than the NPLs with a smaller equivalent diameter.
2. In-substituted NPLs with lower saturation magnetization than Sc-substituted NPLs with comparable equivalent diameter distribution order to ferromagnetic nematic phase at higher concentrations. Stronger magnetic interaction lowers the threshold volume fraction for the isotropic-nematic phase transition.
3. The threshold volume fraction of Sc-substituted suspensions decreases with increasing concentration of dissolved DBSA. The increased concentration of dissociated DBSA decreases the Debye screening length in the suspensions and reduces the electrostatic repulsion. Moreover, the increased concentration of dissociated DBSA affects the effective shape anisotropy of the NPLs. Consequently, the NPLs move closer together and experience stronger magnetic attraction.

We have shown that by using the optimized preparation of nematic suspensions, the threshold volume fraction of the isotropic-nematic phase transition can occur at volume fractions about five times lower than those determined for some systems with nonmagnetic platelets [145], [146], and as first observed for BHF NPLs ($\phi > 28$ %) [123].

In the last part of the dissertation, we implemented the knowledge gained in the first two parts with the aim of preparing stable colloidal suspensions in aqueous, nonpolar solvents and LC 5CB. Different surface modifications using ligands with one or more functional groups, promesogenic ligands and several combinations of different ligands led to the following results:

1. Colloidal stabilization in water is enabled if the ligand has a functional group that gives a sufficiently high surface charge in water. Such groups have been shown to be carboxylic acids, phosphonic acids, and sulfonic acids.
2. Among the other ligands, colloidal stabilization in water was enabled with the ligand Pether, which does not possess a functional group that would provide a surface charge for the NPLs. Moreover, highly concentrated aqueous suspensions of BHF-Pether NPLs showed ferromagnetic ordering. This is the second example of a ferromagnetic nematic suspension in an isotropic solvent after the DBSA-modified NPLs in 1-butanol [123]. Moreover, the Pether-modified NPLs first dispersed in 1-butanol and subsequently transferred to 5CB were colloidally stable in the isotropic and nematic phases.
3. Colloidal stabilization of nanoplatelets smaller than 35 nm in nonpolar solvents, such as chloroform and toluene, was achieved by OA and RA surface modification. Both modifications enabled colloidal stability even in isotropic and nematic 5CB. Together with the BHF-Pether NPLs, these are the only ferromagnetic nematic LC suspensions reported after the discovery of the first suspension [3].
4. Various combinations of promesogenic and linear ligands have efficiently colloidally stabilized the NPLs in ethanol, toluene, and isotropic 5CB. In the latter case, the surface layer of the promesogenic ligands on the NPLs must be diluted with nonpromesogenic and sterically simple ligands to allow the 5CB molecules to penetrate between the surface ligands. The BHF-10POCB-AL and BHF-PSA-10POCB NPLs, which reversibly aggregate and show an intermediate phase between isotropic and nematic phases in 5CB, are interesting for further research to stabilize BHF-promesogenic-ligand NPLs in an NLC.

In this work, we have shown that colloidal stability of BHF NPLs can be ensured by sufficient electrostatic or electrosteric repulsion in aqueous and alcoholic solvents. Steric repulsion and surface wettability are important for colloidal stabilization in nonpolar solvents and 5CB, as previously shown for spherical particles [65], [71], [79]. However, the approaches for colloidal stabilization of spherical nanoparticles with promesogenic ligands [71], [79], [101], [169] were not suitable for BHF NPLs. Finally, highly colloidally stable suspensions with ferromagnetic nematic order in an isotropic solvent and nematic 5CB were obtained using a suitable combination of surface-modifying ligand and solvent.

References

[1] D. Lisjak and A. Mertelj, "Anisotropic magnetic nanoparticles : A review of their properties, syntheses and potential applications," *Prog. Mater. Sci.*, vol. 95, pp. 286–328, 2018, doi: 10.1016/j.pmatsci.2018.03.003.

[2] T. Goršak *et al.*, "Magneto-mechanical actuation of barium-hexaferrite nanoplatelets for the disruption of phospholipid membranes," *J. Colloid Interface Sci.*, vol. 579, pp. 508–519, 2020, doi: 10.1016/j.jcis.2020.06.079.

[3] A. Mertelj, D. Lisjak, M. Drofenik, and M. Čopič, "Ferromagnetism in suspensions of magnetic platelets in liquid crystal," *Nature*, vol. 504, no. 7479, pp. 237–241, 2013, doi: 10.1038/nature12863.

[4] G. Ferk *et al.*, "Monolithic magneto-optical nanocomposites of barium hexaferrite platelets in PMMA," *Sci. Rep.*, vol. 5, pp. 1–8, 2015, doi: 10.1038/srep11395.

[5] M. Wang and Y. Yin, "Magnetically responsive nanostructures with tunable optical properties," *J. Am. Chem. Soc.*, vol. 138, pp. 6315–6323, 2016, doi: 10.1021/jacs.6b02346.

[6] K. G. Kornev, D. Halverson, G. Korneva, Y. Gogotsi, and G. Friedman, "Magnetostatic interactions between carbon nanotubes filled with magnetic nanoparticles," *Appl. Phys. Lett.*, vol. 92, p. 233117, 2008, doi: 10.1063/1.2940303.

[7] A. Tokarev, I. Luzinov, J. R. Owens, and K. G. Kornev, "Magnetic rotational spectroscopy with nanorods to probe time-dependent rheology of microdroplets," *Langmuir*, vol. 28, pp. 10064–71, 2012.

[8] L. Chevry, N. K. Sampathkumar, A. Cebers, and J.-F. Berret, "Magnetic wire-based sensors for the microrheology of complex fluids," *Phys. Rev. B*, vol. 88, p. 062306, 2013, doi: 10.1103/PhysRevE.88.062306.

[9] J. Hu *et al.*, "Magnetic nanoplatelets for high contrast cardiovascular imaging by magnetically modulated optical coherence tomography," *ChemPhotoChem*, vol. 3, no. 7, pp. 529–539, 2019, doi: 10.1002/cptc.201900178.

[10] P. B. Braun, "The crystal structures of a new group of ferromagnetic compound," *Philips Res. Rep.*, vol. 12, no. December 1957, pp. 491–548, 1957.

[11] R. C. Pullar, "Hexagonal ferrites: A review of the synthesis, properties and applications of hexaferrite ceramics," *Prog. Mater. Sci.*, vol. 57, no. 7, pp. 1191–1334, 2012, doi: 10.1016/j.pmatsci.2012.04.001.

[12] E. Pollert, "Crystal chemistry of magnetic oxides part 2: hexagonal ferrites," *Prog. Cryst. Growth Charact.*, vol. 11, pp. 155–205, 1986.

[13] R. B. Jotania and H. S. Virk, "Y-type hexaferrites: structural, dielectric and magnetic properties," in *Solid State Phenomena*, vol. 189, 2012, pp. 209–232.

[14] J. Smit and H. P. J. Wijn, *Ferrites : physical properties of ferrimagnetic oxides in relation to their technical applications*. Eindhoven: Philips Technical Library, 1959.

[15] J. M. D. Coey, *Magnetism and magnetic materials*. New York: Cambridge University Press, 2009.

[16] R. M. Cornell and U. Schwertmann, *The iron oxides: structure, properties, reactions, occurences and uses*, 2nd ed. Weinheim: WILEY-VCH, 2003.

[17] B. D. Cullity and C. D. Graham, *Introduction to magnetic materials*, Second. New Jersey: John Wiley & Sons, 2009.

[18] A. Hubert and R. Schäfer, *Magnetic domains: the analysis of magnetic microstructures. Corrected edition.* Berlin: Springer, 2008.

[19] Ž. Gregorin, P. Hribar Boštjančič, N. Sebastián, D. Lisjak, N. Osterman, and A. Mertelj, "Dynamics of domain formation in a ferromagnetic liquid," in *Polarity and chirality in soft matter: book of abstracts*, 2021, p. 22.

[20] K. D. Sattler, *Handbook of nanophysics: Nanoparticles and quantum dots*. Boca Raton: CRC Press, 2011.

[21] D. Jiles, *Introduction to magnetism and magnetic materials*, 1st ed. Chapman and Hall, 1991.

[22] D. Primc, D. Makovec, D. Lisjak, and M. Drofenik, "Hydrothermal synthesis of ultrafine barium hexaferrite nanoparticles and the preparation of their stable suspensions," *Nanotechnology*, vol. 20, no. 31, 2009, doi: 10.1088/0957-4484/20/31/315605.

[23] V. Marghussian, "Magnetic properties of nano-glass ceramics," in *Nano-Glass Ceramics*, 2015, pp. 181–223.

[24] R. E. Rosensweig, *Ferrohydrodynamics*. Cambridge University Press, 1985.

[25] M. Drofenik, M. Kristl, A. Žnidaršič, D. Hanžel, and D. Lisjak, "Hydrothermal synthesis of Ba-hexaferrite nanoparticles," *J. Am. Ceram. Soc.*, vol. 90, no. 7, pp. 2057–2061, 2007, doi: 10.1111/j.1551-2916.2007.01740.x.

[26] G. Dhanaraj, K. Byrappa, V. Prasad, and M. Dudley, *Handbook of crystal growth*. Springer, 2010.

[27] M. Yoshimura and K. Byrappa, "Hydrothermal processing of materials: Past, present and future," *J. Mater. Sci.*, vol. 43, no. 7, pp. 2085–2103, 2008, doi: 10.1007/s10853-007-1853-x.

[28] K. Byrappa and M. Yoshimura, *Handbook of hydrothermal technology: A technology for crystal growth and materials processing*. Park Ridge: N.J.: Noyes Publications, 2001.

[29] J. Jolivet, M. Henry, J. Livage, and E. Bescher, *Metal oxide chemistry and synthesis*. Chichester: John Wiley & Sons, Ltd., 2000.

[30] S. Campelj, D. Makovec, and M. Drofenik, "Preparation and properties of water-based magnetic fluids," *J. Phys. Condens. Matter*, vol. 20, p. 204101 (5pp), 2008, doi: 10.1088/0953-8984/20/20/204101.

[31] J. Polte, "Fundamental growth principles of colloidal metal nanoparticles – a new perspective," *CrystEngComm*, vol. 17, no. 36, pp. 6809–6830, 2015, doi: 10.1039/C5CE01014D.

[32] R. F. Strickland-Constable, *Kinetics and mechanism of crystallization*. Academic

Press inc., 1968.

[33] V. K. LaMer and R. H. Dinegar, "Theory, production and mechanisms of formation of monodispersed hydrosols," *J. od Am. Chem. Soc.*, vol. 72, no. 11, pp. 4847–4854, 1950.

[34] A. Mali and A. Ataie, "Structural characterization of nano-crystalline BaFe12O19 powders synthesized by sol–gel combustion route," *Scr. Mater.*, vol. 53, pp. 1065–1070, 2005, doi: 10.1016/j.scriptamat.2005.06.037.

[35] J. Huang, H. Zhuang, and W. Li, "Optimization of the microstructure of low-temperature combustion-synthesized barium ferrite powder," *J. Magn. Magn. Mater.*, vol. 256, pp. 390–395, 2003.

[36] W. Zhong, W. Ding, N. Zhang, J. Hong, Q. Yan, and Y. Du, "Key step in synthesis of ultrafine BaFe12O19 by sol-gel technique," *J. Magn. Magn. Mater.*, vol. 168, pp. 196–202, 1997.

[37] B. T. Shirk and W. R. Buessem, "Magnetic properties of barium ferrite formed by crystallization of a glass," *J. Am. Ceram. Soc.*, vol. 53, pp. 192–196, 1970.

[38] L. Rezlescu, E. Rezlescu, P. D. Popa, and N. Rezlescu, "Fine barium hexaferrite powder prepared by the crystallisation of glass," *J. Magn. Magn. Mater.*, vol. 193, pp. 288–290, 1999, doi: 10.1016/S0304-8853(98)00442-9.

[39] D. Borin, R. Müller, and S. Odenbach, "Magnetoviscosity of a magnetic fluid based on barium hexaferrite nanoplates," *Materials (Basel).*, vol. 14, p. 1870, 2021, doi: 10.3390/ma14081870.

[40] M. Drofenik *et al.*, "The concept of a low-temperature synthesis for superparamagnetic BaFe12O19 particles," *J. Am. Ceram. Soc.*, vol. 93, no. 6, pp. 1602–1607, 2010, doi: 10.1111/j.1551-2916.2010.03620.x.

[41] M. Drofenik *et al.*, "The hydrothermal synthesis of super-paramagnetic barium hexaferrite particles," *Mater. Chem. Phys.*, vol. 127, no. 3, pp. 415–419, 2011, doi: 10.1016/j.matchemphys.2011.02.037.

[42] D. Makovec *et al.*, "Discrete evolution of the crystal structure during the growth of Ba-hexaferrite nanoplatelets," *Nanoscale*, vol. 10, no. 30, pp. 14480–14491, 2018, doi: 10.1039/c8nr03815e.

[43] D. Lisjak and M. Drofenik, "Chemical substitution-an alternative strategy for controlling the particle size of barium ferrite," *Cryst. Growth Des.*, vol. 12, no. 11, pp. 5174–5179, 2012, doi: 10.1021/cg301227r.

[44] D. Makovec *et al.*, "Incorporation of Sc into the structure of barium-hexaferrite nanoplatelets and its extraordinary finite-size effect on the magnetic properties," *Acta Mater.*, vol. 172, pp. 84–91, 2019, doi: 10.1016/j.actamat.2019.04.050.

[45] R. Díaz-Pardo, S. Bierlich, J. Töpfer, and R. V. Monjaras, "Electron spin resonance (ESR) of magnetic sublattices in Sc-substituted barium hexaferrite," *AIP Adv.*, vol. 6, no. 5, pp. 1–6, 2016, doi: 10.1063/1.4948796.

[46] J. N. Israelachvili, *Intermolecular and surface forces*, 3rd ed. Academic Press, 2011.

[47] G. V Lowry *et al.*, "Guidance to improve the scientific value of zeta-potential measurements in nanoEHS," *Environ. Sci. Nano*, vol. 3, pp. 953–965, 2016, doi: 10.1039/C6EN00136J.

[48] P. C. Hiemenz and R. Rajagopalan, *Principles of colloid and surface chemistry*, 3rd

ed. New York: Marcel Dekker, 1997.

[49] I. D. Morrison, "Electrical charges in nonaqueous media," *Colloids Surf., A*, vol. 71, pp. 1–37, 1993.

[50] F. M. Fowkes and R. J. Pugh, "Steric and electrostatic contributions to the colloidal properties of nonaqueous dispersions," in *Polymer Adsorption and Dispersion Stability*, vol. 240, Washington DC: American Chemical Society, 1984, pp. 331–354.

[51] R. J. Pugh, T. Matsunaga, and F. M. Fowkes, "The dispersibility and stability of carbon black in media of low dielectric constant. 1. Electrostatic and steric contributions to colloidal stability," *Colloids Surf.*, vol. 7, pp. 183–207, 1983.

[52] K. Kandori, K. Kon-no, and A. Kitahara, "The dispersion stability of colloidal particles in dioxane-water mixtures," *Bull. Chem. Soc. Jpn.*, vol. 57, pp. 3419–3425, 1984.

[53] K. Tamaribuchi and L. M. Smith, "Charge-determining species in a non-aqueous solvent," *J. Colloid Interface Sci.*, vol. 22, pp. 404–407, 1966.

[54] D. J. Shaw, *Introduction to colloid and surface chemistry*, 4th ed. Burlington, MA, USA: Butterworth-Heinemann Publications, 2000.

[55] P. Hribar Boštjančič, M. Tomšič, A. Jamnik, D. Lisjak, and A. Mertelj, "Electrostatic interactions between barium hexaferrite nanoplatelets in alcohol suspensions," *J. Phys. Chem. C*, vol. 123, no. 37, pp. 23272–23279, 2019, doi: 10.1021/acs.jpcc.9b07455.

[56] S. Odenbach, *Colloidal magnetic fluids: basics, development and application of ferrofluids*. Berlin Heidelberg: Springer, 2009.

[57] S. Odenbach, *Ferrofluids: magnetically controllable fluids and their applications*. Berlin Heidelberg: Springer, 2002.

[58] N. T. K. Thanh, *Magnetic nanoparticles from fabrication to clinical applications*. CRC Press, 2012.

[59] G. M. Whitesides and B. Grzybowski, "Self-assembly at all scales," *Science*, vol. 295, pp. 2418–2421, 2002.

[60] L. E. Depero and L. M. Curri, "Inorganic self-assembly," *Curr. Opin. Solid State Mater. Sci.*, vol. 8, no. 2, pp. 103–109, 2004.

[61] C. Yee *et al.*, "Self-assembled monolayers of alkanesulfonic and -phosphonic acids on amorphous iron oxide nanoparticles," *Langmuir*, vol. 15, pp. 7111–7115, 1999, doi: 10.1021/la990663y.

[62] S. Ovtar, D. Lisjak, and M. Drofenik, "Barium hexaferrite suspensions for electrophoretic deposition," *J. Colloid Interface Sci.*, vol. 337, no. 2, pp. 456–463, 2009, doi: 10.1016/j.jcis.2009.05.041.

[63] X. Gao and J. Chorover, "Adsorption of perfluorooctanoic acid and perfluorooctanesulfonic acid to iron oxide surfaces as studied by flow-through ATR-FTIR spectroscopy," *Environ. Chem.*, vol. 9, no. January, pp. 148–157, 2012, doi: 10.1071/EN11119.

[64] L. Zhang, R. He, and H. C. Gu, "Oleic acid coating on the monodisperse magnetite nanoparticles," *Appl. Surf. Sci.*, vol. 253, pp. 2611–2617, 2006, doi: 10.1016/j.apsusc.2006.05.023.

[65] S. Gyergyek, D. Makovec, and M. Drofenik, "Colloidal stability of oleic- and

ricinoleic-acid-coated magnetic nanoparticles in organic solvents," *J. Colloid Interface Sci.*, vol. 354, no. 2, pp. 498–505, 2011, doi: 10.1016/j.jcis.2010.11.043.

[66] Y. Sahoo *et al.*, "Aqueous ferrofluid of magnetite nanoparticles: fluorescence labeling and magnetophoretic control," *J. Phys. Chem. B*, vol. 109, pp. 3879–3885, 2005.

[67] S. Gyergyek, D. Makovec, A. Mertelj, M. Huskić, and M. Drofenik, "Superparamagnetic nanocomposite particles synthesized using the mini-emulsion technique," *Colloids Surf., A*, vol. 366, no. 1–3, pp. 113–119, 2010, doi: 10.1016/j.colsurfa.2010.05.035.

[68] B. Kim *et al.*, "Rapid dye adsorption via surface modification of TiO2 photoanodes for dye-sensitized solar cells," *Appl. Mater. Interfaces*, vol. 5, no. 11, pp. 5201–5207, 2013.

[69] D. Lisjak *et al.*, "Formation of Fe(III)-phosphonate coatings on barium hexaferrite nanoplatelets for porous nanomagnets," *ACS Omega*, vol. 5, no. 23, pp. 14086–14095, 2020, doi: 10.1021/acsomega.0c01597.

[70] M. F. Prodanov, M. Y. Diakov, G. S. Vlasenko, and V. V. Vashchenko, "Towards new oligomesogenic phosphonic acids as stabilizers of nanoparticles colloids in nematic liquid crystals," *Synlett*, vol. 26, no. 13, pp. 1905–1910, 2015, doi: 10.1055/s-0034-1379930.

[71] M. F. Prodanov, O. G. Buluy, E. V. Popova, S. A. Gamzaeva, Y. O. Reznikov, and V. V. Vashchenko, "Magnetic actuation of a thermodynamically stable colloid of ferromagnetic nanoparticles in a liquid crystal," *Soft Matter*, vol. 12, no. 31, pp. 6601–6609, 2016, doi: 10.1039/C6SM00906A.

[72] O. Buluy *et al.*, "Influence of surface treatment of ferromagnetic nanoparticles on properties of thermotropic nematic liquid crystals," *Mol. Cryst. Liq. Cryst.*, vol. 560, pp. 149–158, 2012, doi: 10.1080/15421406.2012.663195.

[73] P. J. Hotchkiss *et al.*, "The modification of indium tin oxide with tuning of surface properties, and potential for use in organic electronic applications," *Acc. Chem. Res.*, vol. 45, no. 3, pp. 337–346, 2012.

[74] C. Queffélec, M. Petit, P. Janvier, D. A. Knight, and B. Bujoli, "Surface modification using phosphonic acids and esters," *Chem. Rev.*, vol. 112, no. 7, pp. 3777–3807, 2012, doi: 10.1021/cr2004212.

[75] P. H. Mutin, G. Guerrero, and A. Vioux, "Hybrid materials from organophosphorus coupling molecules," *J. Mater. Chem.*, vol. 15, pp. 3761–3768, 2005, doi: 10.1039/b505422b.

[76] W. Gao, L. Dickinson, C. Grozinger, F. G. Morin, and L. Reven, "Self-assembled monolayers of alkylphosphonic acids on metal oxides," *Langmuir*, vol. 12, no. 26, pp. 6429–6435, 1996, doi: 10.1021/la9607621.

[77] M. Zwahlen, S. Tosatti, M. Textor, and G. Hähner, "Orientation in methyl- and hydroxyl-terminated self-assembled alkanephosphate monolayers on titanium oxide surfaces investigated with soft X-ray absorption," *Langmuir*, no. 18, pp. 3957–3962, 2002.

[78] H. Ma, O. Acton, D. O. Hutchins, N. Cernetic, and A. K.-Y. Jen, "Multifunctional phosphonic acid self-assembled monolayers on metal oxides as dielectrics, interface modification layers and semiconductors for low-voltage high-performance organic

field-effect transistors," *Phys. Chem. Chem. Phys.*, vol. 14, pp. 14110–14126, 2012, doi: 10.1039/c2cp41557g.

[79] M. F. Prodanov *et al.*, "Thermodynamically stable dispersions of quantum dots in a nematic liquid crystal," *Langmuir*, vol. 29, no. 30, pp. 9301–9309, 2013, doi: 10.1021/la401475b.

[80] D. Andrienko, "Introduction to liquid crystals," *J. Mol. Liq.*, vol. 267, pp. 520–541, 2018, doi: 10.1016/j.molliq.2018.01.175.

[81] J. P. F. Lagerwall and G. Scalia, *Liquid crystals with nano and microparticles*. Singapore: World Scientific Publishing Co. Pte., 2017.

[82] X. Qiao, X. Zhang, Y. Guo, S. Yang, Y. Tian, and Y. Meng, "Boundary layer viscosity of CNT-doped liquid crystals: Effects of phase behavior," *Rheol. Acta*, vol. 52, no. 10–12, pp. 939–947, 2013, doi: 10.1007/s00397-013-0732-4.

[83] P. G. de Gennes and J. Prost, *The physics of liquid crystals*, 2nd ed. New York: Clarendon Press, 1993.

[84] M. Kléman and C. Williams, "Anchoring energies and the nucleation of surface disclination lines in nematics," *Philos. Mag.*, vol. 28, no. 3, pp. 725–732, 1973, doi: 10.1080/14786437308221014.

[85] J. A. Castellano, "Surface anchoring of liquid crystal molecules on various substrates," *Mol. Cryst. Liq. Cryst.*, vol. 94, no. 1–2, pp. 33–41, 1983, doi: 10.1080/00268948308084245.

[86] H. Stark, "Physics of colloidal dispersions in nematic liquid crystals," *Phys. Rep.*, vol. 351, no. 6, pp. 387–474, 2001, doi: 10.1016/S0370-1573(00)00144-7.

[87] I. Smalyukh, "Liquid crystal colloids," *Annu. Rev. Condens. Matter Phys.*, vol. 9, 2018, doi: 10.1146/annurev-conmatphys-033117-054102.

[88] J. D. Jackson, *Classical electrodynamics*. New York: John Wiley & Sons, 1962.

[89] P. Poulin, H. Stark, T. C. Lubensky, and D. A. Weitz, "Novel Colloidal Interactions in Anisotropic Fluids," *Science*, vol. 275, no. 5307, pp. 1770–1773, 1997.

[90] T. C. Lubensky, D. Pettey, and N. Currier, "Topological defects and interactions in nematic emulsions," *Phys. Rev. E*, vol. 57, no. 1, pp. 610–625, 1998.

[91] B. Senyuk, D. Glugla, and I. I. Smalyukh, "Rotational and translational diffusion of anisotropic gold nanoparticles in liquid crystals controlled by varying surface anchoring," *Phys. Rev. E*, vol. 88, no. 6, pp. 1–11, 2013, doi: 10.1103/PhysRevE.88.062507.

[92] U. Tkalec and I. Muševič, "Topology of nematic liquid crystal colloids confined to two dimensions," *Soft Matter*, vol. 9, no. 34, p. 8140, 2013, doi: 10.1039/c3sm50713k.

[93] C. P. Lapointe, T. G. Mason, and I. I. Smalyukh, "Shape-controlled colloidal interactions in nematic liquid crystals," *Science*, vol. 326, no. 5956, pp. 1083–1086, 2009, doi: 10.1126/science.1176587.

[94] A. Mertelj and D. Lisjak, "Ferromagnetic nematic liquid crystals," *Liq. Cryst. Rev.*, vol. 5, no. 1, pp. 1–33, 2017, doi: 10.1080/21680396.2017.1304835.

[95] O. Stamatoiu, J. Mirzaei, X. Feng, and T. Hegmann, "Nanoparticles in liquid crystals and liquid crystalline nanoparticles," *Top. Curr. Chem.*, vol. 318, pp. 331–394, 2012, doi: 10.1007/128.

[96] A. V. Ryzhkova and I. Muševič, "Particle size effects on nanocolloidal interactions

in nematic liquid crystals," *Phys. Rev. E*, vol. 87, no. 3, p. 032501, 2013, doi: 10.1103/PhysRevE.87.032501.

[97] Q. Liu, Y. Yuan, and I. I. Smalyukh, "Electrically and optically tunable plasmonic guest-host liquid crystals with long-range ordered nanoparticles," *Nano Lett.*, vol. 14, no. 7, pp. 4071–4077, 2014, doi: 10.1021/nl501581y.

[98] M. Bagiński, A. Szmurło, A. Andruszkiewicz, M. Wójcik, and W. Lewandowski, "Dynamic self-assembly of nanoparticles using thermotropic liquid crystals," *Liq. Cryst.*, vol. 43, no. 13–15, pp. 2391–2409, 2016, doi: 10.1080/02678292.2016.1225834.

[99] G. L. Nealon *et al.*, "Liquid-crystalline nanoparticles: Hybrid design and mesophase structures," *Beilstein J. Org. Chem.*, vol. 8, pp. 349–370, 2012, doi: 10.3762/bjoc.8.39.

[100] M. Draper *et al.*, "Self-assembly and shape morphology of liquid-crystalline gold metamaterials," *Adv. Funct. Mater.*, vol. 21, no. 7, pp. 1260–1278, 2011, doi: 10.1002/adfm.201001606.

[101] M. Hähsler, I. Appel, and S. Behrens, "Magnetic hybrid materials in liquid crystals," *Phys. Sci. Rev.*, pp. 1–24, 2020.

[102] S. H. Chen and N. M. Amer, "Observation of macroscopic collective behavior and new texture in magnetically doped liquid crystals," *Phys. Rev. Lett.*, vol. 51, no. 25, pp. 2298–2301, 1983, doi: 10.1103/PhysRevLett.51.2298.

[103] N. Podoliak *et al.*, "Macroscopic optical effects in low concentration ferronematics," *Soft Matter*, vol. 7, no. 10, p. 4742, 2011, doi: 10.1039/c1sm05051f.

[104] P. Kopčanský *et al.*, "Structural changes in the 6CHBT liquid crystal doped with spherical, rodlike, and chainlike magnetic particles," *Phys. Rev. E*, vol. 78, no. 1, pp. 4–8, 2008, doi: 10.1103/PhysRevE.78.011702.

[105] I. Langmuir, "The role of attractive and repulsive forces in the formation of tactoids, thixotropic gels, protein crystals and coacervates," *J. Chem. Phys.*, vol. 6, pp. 873–896, 1938.

[106] H. Z. Zocher, "Über freiwillige Strukturbildung in Solen. (Eine neue Art anisotrop flüssiger Medien.)," *Z. Anorg. Allg. Chem.*, vol. 147, pp. 91–110, 1925.

[107] F. C. Bawden, N. W. Pirie, J. D. Bernal, and I. Fankuchen, "Liquid crystalline substances from virus-infected plants," *Nature*, vol. 138, pp. 1051–1052, 1936.

[108] F. M. Van Der Kooij and H. N. W. Lekkerkerker, "Liquid-crystalline phase behavior of a colloidal rod-plate mixture," *Phys. Rev. Lett.*, vol. 84, no. 4, pp. 781–784, 2000.

[109] D. van der Beek *et al.*, "Magnetic-field-induced orientational order in the isotropic phase of hard colloidal platelets," *Phys. Rev. E*, vol. 73, p. 041402, 2006, doi: 10.1103/PhysRevE.73.041402.

[110] D. van Der Beek and H. N. W. Lekkerkerker, "Liquid crystal phases of charged colloidal platelets," *Langmuir*, vol. 20, pp. 8582–8586, 2004, doi: 10.1021/la049455i.

[111] J. P. Gabriel, C. Sanchez, and P. Davidson, "Observation of nematic liquid-crystal textures in aqueous gels of smectite clays," *J. Phys. Chem.*, vol. 100, pp. 11139–11143, 1996.

[112] P. Woolston and J. S. van Duijneveldt, "Isotropic - nematic phase transition in aqueous sepiolite suspensions," *J. Colloid Interface Sci.*, vol. 437, pp. 65–70, 2015, doi: 10.1016/j.jcis.2014.09.014.

[113] L. J. Michot *et al.*, "Liquid-crystalline aqueous clay suspensions," *Proc. Natl. Acad. Sci.*, vol. 103, no. 44, pp. 16101–16104, 2006, doi: 10.1073/pnas.0605201103.

[114] E. Paineau *et al.*, "Liquid-crystalline nematic phase in aqueous suspensions of a disk-shaped natural beidellite clay," *J. Phys. Chem. B*, vol. 113, pp. 15858–15869, 2009.

[115] L. Onsager, "The effects of shape on the interaction of colloidal particles," *Ann. New York Acad. Sci.*, vol. 51, pp. 627–659, 1949.

[116] J. A. C. Veerman and D. Frenkel, "Phase behavior of disklike hard-core mesogens," *Phys. Rev. A*, vol. 45, no. 8, pp. 5632–5648, 1992, doi: 10.1103/PhysRevA.45.5632.

[117] D. Frenkel and R. Eppenga, "Monte Carlo study of the isotropic-nematic transition in a fluid of thin hard disks," *Am. Phys. Soc.*, vol. 49, no. 15, pp. 1089–1092, 1982.

[118] M. Vis, H. H. Wensink, H. N. W. Lekkerkerker, and D. Kleshchanok, "Nematic and lamellar liquid-crystalline phases in suspensions of charged silica-coated gibbsite platelets," *Mol. Phys.*, vol. 113, pp. 1053–1060, 2014, doi: 10.1080/00268976.2014.985276.

[119] P. A. Forsyth, S. Marčelja, D. J. Mitchell, and B. W. Ninham, "Onsager Transition in Hard Plate Fluid," *J. Chem. Soc., Faraday Trans. 2*, vol. 73, pp. 84–88, 1977.

[120] D. Sun, H. Sue, Z. Cheng, Y. Martínez-Ratón, and E. Velasco, "Stable smectic phase in suspensions of polydisperse colloidal platelets with identical thickness," *Phys. Rev. E*, vol. 80, p. 041704, 2009, doi: 10.1103/PhysRevE.80.041704.

[121] M. A. Bates, "Influence of particle shape on the nematic — isotropic transition of colloidal platelet systems," *J. Chem. Phys.*, vol. 111, pp. 1732–1736, 1999, doi: 10.1063/1.479433.

[122] M. A. Bates and D. Frenkel, "Nematic – isotropic transition in polydisperse systems of infinitely thin hard platelets," *J. Chem. Phys.*, vol. 110, pp. 6553–6559, 1999, doi: 10.1063/1.478558.

[123] M. Shuai *et al.*, "Spontaneous liquid crystal and ferromagnetic ordering of colloidal magnetic nanoplates," *Nat. Commun.*, vol. 7, p. 10394, 2016, doi: 10.1038/ncomms10394.

[124] A. Mertelj, B. Lampret, D. Lisjak, J. Klepp, J. Kohlbrecher, and čop, "Evolution of nematic and ferromagnetic ordering in suspensions of magnetic nanoplatelets," *Soft Matter*, vol. 15, pp. 5412–5420, 2019, doi: 10.1039/c9sm00949c.

[125] P. Hribar Boštjančič, Ž. Gregorin, N. Sebastián, N. Osterman, D. Lisjak, and A. Mertelj, "Isotropic to nematic transition in alcohol ferrofluids of barium hexaferrite nanoplatelets," *J. Mol. Liq.*, vol. 348, 2022, doi: 10.1016/j.molliq.2021.118038.

[126] J. F. Miller, K. Schätzel, and B. Vincent, "The determination of very small electrophoretic mobilities in polar and nonpolar colloidal dispersions using phase analysis light scattering," *J. Colloid Interface Sci.*, vol. 143, no. 2, pp. 532–554, 1991, doi: 10.1016/0021-9797(91)90286-H.

[127] B. J. Berne and R. Pecora, "Dynamic light scattering with applications to chemistry, biology, and physics." Dover Pulbications, Inc., Mineola, N.Y., 2000.

[128] P. S. Singh, "Chapter 6 - Small-angle scattering techniques (SAXS/SANS)," in *Membrane Characterization*, N. Hilal, A. F. Ismail, T. Matsuura, and D. Oatley-Radcliffe, Eds. Elsevier B.V., 2017, pp. 95–111.

[129] D. Orthaber, A. Bergmann, and O. Glatter, "SAXS experiments on absolute scale with Kratky systems using water as a secondary standard," *J. Appl. Crystallogr.*, vol. 33, no. 2, pp. 218–225, 2000, doi: 10.1107/s0021889899015216.

[130] O. Glatter, "Instrumentation for SAXS and SANS," in *Scattering methods and their Application in Colloid and Interface science*, Elsevier, 2018, pp. 123–136.

[131] J. A. Lake, "An iterative method of slit-correcting small angle X-ray data," *Acta Cryst.*, vol. 23, no. 2, pp. 191–194, 1967, doi: 10.1107/s0365110x67002440.

[132] J. W. Robinson, E. M. Skelly Frame, and G. M. Frame II, *Undergraduate Instrumental Analysis*, Seventh ed. Boca Raton: CRC Press Taylor & Francis Group, 2014.

[133] P. Atkins and J. de Paula, *Physical Chemistry*, 8th ed., vol. 272, no. 4. New York: Oxford University Press, 2006.

[134] A. Ortega and J. Garcia De La Torre, "Hydrodynamic properties of rodlike and dislike particles in dilute solution," *J. Chem. Phys.*, vol. 119, no. 18, pp. 9914–9919, 2003, doi: 10.1063/1.1615967.

[135] R. Agra, E. Trizac, and L. Bocquet, "The interplay between screening properties and colloid anisotropy : Towards a reliable pair potential for disc-like charged particles," *Eur. Phys. J. E*, vol. 15, pp. 345–357, 2004, doi: 10.1140/epje/i2004-10052-x.

[136] B. Russel, D. A. Saville, and W. R. Schowalter, *Colloidal dispersions*. Cambridge: Cambridge University Press, 1992.

[137] P. Sarkar and P. S. Nicholson, "Electrophoretic deposition (EPD): mechanisms, kinetics, and applications to ceramics," *J. Am. Ceram. Soc.*, vol. 79, pp. 1987–2002, 1996.

[138] A. J. Hess, Q. Liu, and I. I. Smalyukh, "Optical patterning of magnetic domains and defects in ferromagnetic liquid crystal colloids," *Appl. Phys. Lett.*, vol. 107, p. 071906, 2015, doi: 10.1063/1.4928552.

[139] K. Klimaszewski, A. Boruń, A. Bald, and R. J. Sengwa, "Static permittivities of isomeric butanol mixtures at temperatures from (288.15 to 308.15) K," *J. Chem. Eng. Data*, vol. 57, no. 11, pp. 3164–3170, 2012, doi: 10.1021/je3007666.

[140] N. V. Sastry and M. K. Valand, "Dielectric constants, refractive indexes and polarizations for 1-alcohol+heptane mixtures at 298.15 and 308.15 K," *Ber. Bunsenges. Phys. Chem.*, vol. 101, pp. 243–250, 1997.

[141] N. V. Sastry and S. R. Patel, "Excess volumes and dielectric properties for (methyl methacrylate + a branched alcohol) at T = 298.15 K and T = 308.15 K," *J. Chem. Thermodyn.*, vol. 32, no. 12, pp. 1669–1682, 2000, doi: 10.1006/jcht.2000.0707.

[142] N. V Sastry and M. K. Valand, "Viscosities and densities for heptane +1-pentanol, +1-hexanol, +1-heptanol, +1-octanol, +1-decanol, and +1-dodecanol at 298.15 K and 308.15 K," *J. Chem. Eng. Data*, vol. 41, pp. 1426–1428, 1996, doi: 10.1021/je9601725.

[143] S. Chen, Q. Lei, and W. Fang, "Viscosities and densities for binary mixtures of N-methylpiperazine with methanol, ethanol, n-propanol, iso-propanol, n-butanol and iso-butanol at 293.15, 298.15 and 303.15 K," *Fluid Phase Equilib.*, vol. 234, no. 1–2, pp. 22–33, 2005, doi: 10.1016/j.fluid.2005.05.012.

[144] T. M. Aminabhavi, M. I. Aralaguppi, S. B. Harogoppad, and R. H. Balundgi, "Densities, viscosities, refractive indices, and speeds of sound for methyl acetoacetate + aliphatic alcohols (C1–C8)," *J. Chem. Eng. Data*, vol. 38, no. 1, pp. 31–39, 1993, doi: 10.1021/je00009a008.

[145] F. M. van der Kooij, D. van der Beek, and H. N. W. Lekkerkerker, "Isotropic - nematic phase separation in suspensions of polydisperse colloidal platelets," *J. Phys. Chem. B*, vol. 105, pp. 1696–1700, 2001.

[146] F. M. van der Kooij, K. Kassapidou, and H. N. W. Lekkerkerker, "Liquid crystal phase transitions in suspensions of polydisperse plate-like particles," *Nature*, vol. 406, pp. 868–871, 2000.

[147] D. van der Beek and H. N. W. Lekkerkerker, "Nematic ordering vs. gelation in suspensions of charged platelets," *Europhys. Lett.*, vol. 61, no. 5, pp. 702–707, 2003.

[148] A. A. Eliseev *et al.*, "Tunable order in colloids of hard magnetic hexaferrite nanoplatelets," *Nano Res.*, vol. 15, pp. 898–906, 2022, doi: 10.1007/s12274-021-3572-z.

[149] M. Rosenberg *et al.*, "The influence of polydispersity on the structural properties of the isotropic phase of magnetic nanoplatelets," *J. Mol. Liq.*, vol. 312, p. 113293, 2020, doi: 10.1016/j.molliq.2020.113293.

[150] T. Goršak, D. Makovec, U. Javornik, B. Belec, S. Kralj, and D. Lisjak, "A functionalization strategy for the dispersion of permanently magnetic barium-hexaferrite nanoplatelets in complex biological media," *Colloids Surf., A*, vol. 573, no. April, pp. 119–127, 2019, doi: 10.1016/j.colsurfa.2019.04.051.

[151] Y. Lalatonne, C. Paris, J. M. Serfaty, P. Weinmann, M. Lecouvey, and L. Motte, "Bis-phosphonates-ultra small superparamagnetic iron oxide nanoparticles: A platform towards diagnosis and therapy," *Chem. Commun.*, no. 22, pp. 2553–2555, 2008, doi: 10.1039/b801911h.

[152] G. Socrates, *Infrared and Raman characteristic group frequencies: Tables and charts*. Chichester, 2001.

[153] A. Nersasian and P. R. Johnson, "Infrared spectra of alkanesulfonic acids, chlorosulfonated polyethylene, and their derivatives," *J. Appl. Polym. Sci.*, vol. 9, pp. 1653–1668, 1965.

[154] H. Zhang, X. Wen, and Y. Wang, "Synthesis and characterization of sulfate and dodecylbenzenesulfonate intercalated zinc – iron layered double hydroxides by one-step coprecipitation route," *J. od Solid State Chem.*, vol. 180, pp. 1636–1647, 2007, doi: 10.1016/j.jssc.2007.03.016.

[155] S. Fornarini, "Mass spectrometry of sulfonic acids and their derivatives," in *The chemistry of sulphonic acids, esters and their derivatives*, S. Patai and Z. Rappoport, Eds. John Wiley & Sons, 1991, pp. 73–133.

[156] K. Nakamoto, *Infrared and Raman spectra of inorganic and coordination compounds*. New York: John Wiley & Sons, 1997.

[157] J. Ibarra *et al.*, "Synthesis and characterization of magnetite/PLGA/chitosan nanoparticles," *Mater. Res. Express*, vol. 2, no. 9, p. 095010, 2015, doi: 10.1088/2053-1591/2/9/095010.

[158] K. Bootdee, M. Nithitanakul, and B. P. Grady, "Synthesis and encapsulation of

magnetite nanoparticles in PLGA : effect of amount of PLGA on characteristics of encapsulated nanoparticles," *Polym. Bull.*, vol. 69, pp. 795–806, 2012, doi: 10.1007/s00289-012-0773-3.

[159] C. W. Lai, F. W. Low, M. F. Tai, and S. B. Abdul Hamid, "Iron oxide nanoparticles decorated oleic acid for high colloidal stability," *Adv. Polym. Technol.*, vol. 37, no. 6, pp. 1712–1721, 2018, doi: 10.1002/adv.21829.

[160] R. Tadmor, R. E. Rosensweig, J. Frey, and J. Klein, "Resolving the puzzle of ferrofluid dispersants," *Langmuir*, vol. 16, pp. 9117–9120, 2000.

[161] M. T. López-López, J. D. G. Durán, A. V Delgado, and F. González-Caballero, "Stability and magnetic characterization of oleate-covered magnetite ferrofluids in different nonpolar carriers," *J. Colloid Interface Sci.*, vol. 291, pp. 144–151, 2005, doi: 10.1016/j.jcis.2005.04.099.

[162] J. D. Douglas, W. Ernest, and S. Turner, "XXXI.-The dielectric constants of some organic solvents at their melting or boiling points," *J. Chem. Soc. Trans.*, vol. 107, no. 276, pp. 276–282, 1894.

[163] K. Abe, A. Usami, K. Ishida, Y. Fukushima, and T. Shigenari, "Dielectric and fluorescence study on phase transitions in liquid crystal 5CB and 8CB," *J. Korean Phys. Soc.*, vol. 46, pp. 220–223, 2005.

[164] F. E. Critchfield, J. A. Gibson, and J. L. Hall, "Dielectric constant and refractive index from 20 to 35° and density at 25° for the system tetrahydrofuran—water," *J. Am. Chem. Soc.*, vol. 75, no. 23, pp. 6044–6045, 1953.

[165] P. J. Hotchkiss, M. Malicki, A. J. Giordano, N. R. Armstrong, and S. R. Marder, "Characterization of phosphonic acid binding to zinc oxide," *J. Mater. Chem.*, vol. 21, no. 9, pp. 3107–3112, 2011, doi: 10.1039/c0jm02829k.

[166] Y. P. Piryatinski, L. A. Dolgov, O. V. Yaroshchuk, T. A. Gavrilko, and S. K. Lazarouk, "Enhancement of fluorescence of porous silicon upon saturation by liquid crystal," *Opt. Spectrosc.*, vol. 108, no. 1, pp. 70–79, 2010, doi: 10.1134/S0030400X1001011X.

[167] J. Coates, "Interpretation of infrared spectra, a practical approach," *Encyclopedia of Analytical Chemistry*. John Wiley & Sons, Ltd., pp. 1–23, 2006, doi: 10.1002/9780470027318.a5606.

[168] H. Qi, B. Kinkead, V. M. Marx, H. R. Zhang, and T. Hegmann, "Miscibility and alignment effects of mixed monolayer cyanobiphenyl liquid-crystal-capped gold nanoparticles in nematic cyanobiphenyl liquid crystal hosts," *ChemPhysChem*, vol. 10, no. 8, pp. 1211–1218, 2009, doi: 10.1002/cphc.200800765.

[169] I. Appel *et al.*, "Doping of nematic cyanobiphenyl liquid crystals with mesogen-hybridized magnetic nanoparticles," *Phys. Chem. Chem. Phys.*, vol. 19, no. 19, pp. 12127–12135, 2017, doi: 10.1039/C7CP01438D.

[170] M. F. Prodanov *et al.*, "Dispersion of magnetic nanoparticles in a polymorphic liquid crystal," *Liq. Cryst.*, vol. 39, no. 12, pp. 1512–1526, 2012, doi: 10.1080/02678292.2012.725867.

Bibliography

Publications related to the doctoral dissertation

Original scientific article

[1] P. Hribar Boštjančič, Ž. Gregorin, N. Sebastián, N. Osterman, D. Lisjak, and A. Mertelj, "Isotropic to nematic transition in alcohol ferrofluids of barium hexaferrite nanoplatelets," *J. Mol. Liq.*, vol. 348, 2022, doi: 10.1016/j.molliq.2021.118038.

[2] D. Zabek, A. Grzebielec, L. Cmok, P. Hribar, and A. Mertelj, "Experimental analysis of the stability of ferrofluids based on iron oxide powder," *Inżynieria Bezpieczeństwa Obiektów Antropog.*, vol. 2, pp. 1–6, 2021, doi: 10.37105/iboa.108.

[3] J. Papan, P. Hribar Boštjančič, A. Mertelj, and D. Lisjak, "Preparation of Barium-Hexaferrite/Gold Janus Nanoplatelets Using the Pickering Emulsion Method," *Nanomaterials*, vol. 11, no. 11, p. 2797, 2021, doi: 10.3390/nano11112797.

[4] D. Lisjak *et al.*, "Formation of Fe(III)-phosphonate coatings on barium hexaferrite nanoplatelets for porous nanomagnets," *ACS Omega*, vol. 5, no. 23, pp. 14086–14095, 2020, doi: 10.1021/acsomega.0c01597.

[5] M. Rosenberg *et al.*, "The influence of polydispersity on the structural properties of the isotropic phase of magnetic nanoplatelets," *J. Mol. Liq.*, vol. 312, p. 113293, 2020, doi: 10.1016/j.molliq.2020.113293.

[6] P. Hribar Boštjančič, M. Tomšič, A. Jamnik, D. Lisjak, and A. Mertelj, "Electrostatic interactions between barium hexaferrite nanoplatelets in alcohol suspensions," *J. Phys. Chem. C*, vol. 123, no. 37, pp. 23272–23279, 2019, doi: 10.1021/acs.jpcc.9b07455.

Published scientific conference contribution

[7] D. Zabek, A. Grzebielec, L. Cmok, P. Hribar Boštjančič, A. Mertelj, "Two-phase ferrofluid systems: surfactants and thermal properties of iron oxide Nanofluids for Condensation," in *XIV Research & Development in Power Engineering (RDPE 2019)*, 2019, pp. 01015-1-01015–4.

Published scientific conference contribution (invited lecture)

[8] A. Mertelj *et al.*, "Polar nematic phases," in *Advances in Soft Matter Physics : 47th German Liquid Crystal Conference, GLCC 2021 : Magdeburg*, 2021, p. 20, [Online]. Available: http://www.liquidcr.ovgu.de/resources/GLCC2021/AbstractBook_GLCC_2021.p

df. .

[9] A. Grzebielec, D. Zabek, L. Cmok, P. Hribar Boštjančič, and A. Mertelj, "Two-phase ferrofluid systems: surfactants and thermal properties of iron oxide nanofluids for condensation," in *XIV Research & Development in Power Engineering (RDPE 2019)*, 2019, p. 30.

Published scientific conference contribution abstract

[10] Ž. Gregorin, P. Hribar Boštjančič, N. Sebastián, D. Lisjak, N. Osterman, and A. Mertelj, "Liquid magnets," in *11th Liquid Matter Conference 2020/2021*, 2021, [Online]. Available: https://secure.confis.cz/lmc2020/cd/Files/0101.pdf.

[11] P. Hribar Boštjančič, D. Lisjak, Ž. Gregorin, N. Sebastián, N. Osterman, and A. Mertelj, "Phase diagram of colloidal suspensions of magnetic nanoplatelets," in *11th Liquid Matter Conference 2020/2021*, 2021, [Online]. Available: https://secure.confis.cz/lmc2020/cd/Files/0129.pdf.

[12] P. Hribar Boštjančič, D. Lisjak, Ž. Gregorin, N. Sebastián, N. Osterman, and A. Mertelj, "Phase behaviour of alcohol suspensions of magnetic barium hexaferrite nanoplatelets," in *[1st] Crossnano Crossborder Workshop in Nanoscience and Nanotechnology*, 2021, p. 11, [Online]. Available: http://web.units.it/dottorato/nanotecnologie/sites/nanotecnologie/files/CrossNano Workshop 2021 Abstract Book.pdf. .

[13] Ž. Gregorin, P. Hribar Boštjančič, N. Sebastián, D. Lisjak, N. Osterman, and A. Mertelj, "Dynamics of domain formation in a ferromagnetic liquid," in *Polarity and chirality in soft matter: book of abstracts*, 2021, p. 22, [Online]. Available: http://flc2021.ijs.si/BookOfAbstracts.pdf.

[14] M. Vilfan *et al.*, "Observations of bidirectional flow in ferromagnetic ferrofluids generated by uniaxial magnetic field," in *Polarity and chirality in soft matter: book of abstracts*, 2021, p. 24, [Online]. Available: http://flc2021.ijs.si/BookOfAbstracts.pdf.

[15] M. Küster *et al.*, "Ferromagnetic nematics in rotating and oscillating magnetic fields," in *Polarity and chirality in soft matter: book of abstracts*, 2021, p. 46, [Online]. Available: http://flc2021.ijs.si/BookOfAbstracts.pdf.

[16] P. Medle Rupnik, T. Potisk, P. Hribar Boštjančič, D. Lisjak, and A. Mertelj, "Hydrodynamic coupling in ferromagnetic cholesteric liquid crystals," in *Polarity and chirality in soft matter: book of abstracts*, 2021, p. 92, [Online]. Available: http://flc2021.ijs.si/BookOfAbstracts.pdf.

[17] P. Hribar Boštjančič, Ž. Gregorin, N. Sebastián, N. Osterman, D. Lisjak, and A. Mertelj, "Tuning nematic ordering of barium-hexaferrite nanoplatelets in 1-butanol," in *Polarity and chirality in soft matter: book of abstracts*, 2021, p. 95, [Online]. Available: http://flc2021.ijs.si/BookOfAbstracts.pdf.

[18] J. Papan, P. Hribar Boštjančič, A. Mertelj, and D. Lisjak, "Barium-hexaferrite/gold Janus nanoplatelets," in *Book of abstracts: 27th Annual Meeting of the Slovenian Chemical Society*, 2021, p. 64.

[19] P. Hribar Boštjančič *et al.*, "Colloidal stabilization of magnetic nanoplatelets," in

Book of abstracts: 27th Annual Meeting of the Slovenian Chemical Society, 2021, p. 105.

[20] D. Lisjak *et al.*, "Interaction of the barium hexaferrite nanoplatelets with phosphonic acids," in *Book of abstracts: 27th Annual Meeting of the Slovenian Chemical Society*, 2021, p. 38.

[21] P. Hribar Boštjančič, D. Lisjak, Ž. Gregorin, N. Sebastián, N. Osterman, and A. Mertelj, "Phase behaviour of the suspensions of magnetic nanoplatelets," in *12th Jožef Stefan International Postgraduate School Students' Conference and 14th Young Researchers' Day*, 2020, p. 47, [Online]. Available: http://ipssc.mps.si/BookOfAbstracts.pdf.

[22] P. Hribar Boštjančič *et al.*, "Phase behaviour of the suspensions based on magnetic nanoplatelets," in *Book of abstracts: 26th Annual Meeting of the Slovenian Chemical Society*, 2020, p. 80.

[23] D. Lisjak *et al.*, "Porous nanomagnets made by coating barium hexaferrite nanoplatelets with phosphonic acids," in *Book of abstracts: 26th Annual Meeting of the Slovenian Chemical Society*, 2020, p. 49.

[24] J. Papan, P. Hribar Boštjančič, A. Mertelj, and D. Lisjak, "Preparation of Janus nanoparticles based on bariumhexaferrite nanoparticles," in *Book of abstracts: 26th Annual Meeting of the Slovenian Chemical Society*, 2020, p. 140.

[25] Ž. Gregorin, N. Sebastián, P. Hribar Boštjančič, D. Lisjak, N. Osterman, and A. Mertelj, "Magneto optical properties of nanoplatelet based ferrofluid, ICMF 2019," in *Book of abstracts. 15th International Conference on Magnetic Fluids, ICMF 2019*, 2019, p. 62, [Online]. Available: https://premc.org/doc/ICMF2019/ICMF2019_Book_Of_Abstracts.pdf.

[26] N. Sebastián, P. Hribar Boštjančič, Ž. Gregorin, N. Osterman, D. Lisjak, and A. Mertelj, "Properties and domain formation in ferromagnetic fluids," in *Book of abstracts. 15th International Conference on Magnetic Fluids, ICMF 2019*, 2019, p. 83, [Online]. Available: https://premc.org/doc/ICMF2019/ICMF2019_Book_Of_Abstracts.pdf.

[27] P. Hribar Boštjančič, M. Tomšič, A. Jamnik, D. Lisjak, and A. Mertelj, "Electrostatic interaction between magnetic nanoplatelets in alcohols," in *11th Jožef Stefan International Postgraduate School Students' Conference and 13th Young Researchers' Day*, 2019, p. 63, [Online]. Available: http://ipssc.mps.si/Proceedings/Proceedings2019.pdf.

[28] P. Hribar Boštjančič, M. Tomšič, A. Jamnik, D. Lisjak, and A. Mertelj, "Electrostatic interaction between barium hexaferrite nanoplatelets in alcohol suspensions," in *9th International Colloids Conference*, 2019, p. 71.

[29] P. Hribar Boštjančič, M. Tomšič, A. Jamnik, D. Lisjak, and A. Mertelj, "Electrostatic interactions in alcohol suspensions of barium hexaferrite nanoplatelets," in *Book of abstracts: 25th Annual Meeting of the Slovenian Chemical Society*, 2019, p. 89.

[30] P. Hribar, S. Gyergyek, Z. Syrgiannis, D. Lisjak, and A. Mertelj, "Promesogenic ligands for surface functionalization of barium hexaferrite nanoplatelets," in *Book of abstracts: plenary lectures, keynote lectures, section lectures, poster session. 24th*

Annual Meeting of the Slovenian Chemical Society, 2018.

[31] P. Hribar, S. Gyergyek, Z. Syrgiannis, D. Lisjak, and A. Mertelj, "Use of promesogenic ligands for preparation of liquid crystal colloid with barium hexaferrite nanoplatelets," in *Book of abstracts. 32nd Conference of The European Colloid and Interface Society*, 2018, p. 236, [Online]. Available: http://ecis2018.fkkt.uni-lj.si/dist/img/ECIS2018_BA.pdf.

[32] Ž. Gregorin, P. Hribar, D. Lisjak, A. Mertelj, and N. Osterman, "Tekoči magneti: feromagnetne nanoploščice v mikrofluidičnem vezju," in *Zbornik povzetkov. 11. konferenca fizikov v osnovnih raziskavah*, 2018, p. 38.

[33] P. Hribar, S. Gyergyek, Z. Syrgiannis, D. Lisjak, and A. Mertelj, "Surface functionalization of barium hexaferrite nanoplates with promesogenic molecules," in *10th Jožef Stefan International Postgraduate School Students' Conference and 12th Young Researchers' Day*, 2018, p. 45, [Online]. Available: http://ipssc.mps.si/Proceedings/Proceedings_2018.pdf.

Biography

Patricija Hribar Boštjančič was born on November 15, 1991, in Postojna, Slovenia. She attended elementary school in Podgrad, Slovenia, and graduated secondary school at Gimnazija Koper. In 2010, she enrolled in the first academic bachelor's degree program in chemistry at the Faculty of Chemistry and Chemical Technology at the University of Ljubljana. She received her bachelor's degree in chemistry with the defense of the work entitled "Reakcije tiosemikarbazidov z nekaterimi kovinskimi ioni" in 2014. In the same year, she enrolled in the second cycle master's program in chemistry at the same faculty. She received her master's degree in 2017 with the work "Koordinacijske spojine nekaterih kovinskih ionov z N-etoksikarbonilmetil-N'-(2-piridil)tiosečnino". In 2017, Patricija started her doctoral study at the Jožef Stefan International Postgraduate School, Ljubljana, Slovenia, under the supervision of Asst. Prof. Alenka Mertelj. The experimental work was carried out at the Jožef Stefan Institute, Department of Complex Matter. The focus of her doctoral research was to study the mechanisms for the colloidal stabilization of barium hexaferrite nanoplatelets. The understanding of the mechanisms for the colloidal stabilization of the dodecylbenzenesulfonic acid modified nanoplatelets and their phase behavior in 1-butanol was used for the colloidal stabilization of the barium hexaferrite nanoplatelets in other, non-alcoholic solvents for the preparation of ferromagnetic ferrofluids. During her doctoral study, Patricija participated in workshops and several national and international conferences, where she presented her work either orally or as a poster.